Downloaded from orbit.dtu.dk on: Dec 18, 2017

Technical University of Denmark

Low-dimensional modeling and dynamics of the flow in a lid driven cavity with a rotating rod

Jørgensen, Bo Hoffmann; Larsen, Rasmus; Sørensen, Jens Nørkær; Brøns, Morten

Publication date:
2000

Document Version
Publisher's PDF, also known as Version of record

Link back to DTU Orbit

Citation (APA):
Jørgensen, B. H., Larsen, R., Sørensen, J. N., & Brøns, M. (2000). Low-dimensional modeling and dynamics of the flow in a lid driven cavity with a rotating rod. Kgs. Lyngby, Denmark: Technical University of Denmark (DTU). (ET-PHD; No. 2000-02).

DTU Library
Technical Information Center of Denmark

General rights
Copyright and moral rights for the publications made accessible in the public portal are retained by the authors and/or other copyright owners and it is a condition of accessing publications that users recognise and abide by the legal requirements associated with these rights.

- Users may download and print one copy of any publication from the public portal for the purpose of private study or research.
- You may not further distribute the material or use it for any profit-making activity or commercial gain
- You may freely distribute the URL identifying the publication in the public portal

If you believe that this document breaches copyright please contact us providing details, and we will remove access to the work immediately and investigate your claim.

ET-PHD 2000-02

DTU

Low-dimensional modeling and dynamics of the flow in a lid driven cavity with a rotating rod

Bo Hoffmann Jørgensen

Fluid Mechanics
Department of Energy Engineering
Technical University of Denmark

Low-dimensional modeling and dynamics of the flow in a lid driven cavity with a rotating rod.

Bo Hoffmann Jørgensen

PhD Thesis

2000

Technical University of Denmark
Department of Energy Engineering
Fluid Mechanics Section, Building 403
DK-2800 Lyngby
Denmark

ET-PhD 2000-2
ISBN 87 7475 232 4

Preface

This thesis is submitted in partial fulfillment of the requirements for the PhD at the Technical University of Denmark (DTU). The work was carried out in the Fluid Mechanics section at the Department of Energy Engineering in collaboration with the Department of Mathematics. I would like to express my deepest thanks to my advisors, Jens Nørkær Sørensen and Morten Brøns for their constant support during the project. Also, I am grateful for recieving the scholarship from the Technical University of Denmark which made it possible for me to pursue the PhD in the period from 1996 to 2000.

This project has not been easy. However, I have enjoyed what I did. Therefore, I would like to thank all the people who have helped me during the PhD-project. In particular, my warmest thanks are truly deserved by my wife to be, Anita Hougaard Koch, mange tak skat! Thanks also to Nadine Aubry at the New Jersey Institute of Technology for two pleasant months of discussions, for providing computing facilities and for sharing even her home and family with me from time to time. One of the key persons in all of what has happened is Erik Adler Christensen, whom I first met at the IUTAM symposium at DTU in 1997 and later visited in New York. Erik developed a low-dimensional model of the closed cavity with a rotating lid, and he has performed a massive amount of numerical simulations - Erik, whereever you are in the world, I extend my gratitude to you for all our conversations and for urging me to participate in exciting events.

The period of my PhD is rich of memories and I realize it is difficult for me to include all the people who have helped me. I thank everybody for their help and their part in all the little events of the past that I may recall in the future. Thanks also to my colleagues at the department and many members of the staff at DTU for providing a pleasant atmosphere of everyday life.

The low-dimensional models constructed during the present study have been interesting to investigate and certainly have contributed to a better understanding of the flow in the lid driven cavity with a rotating rod. And, after all, understanding is really what it is all about.

Summary

The flow in a lid driven cavity with a rotating rod has been studied by numerical simulations utilizing an axisymmetric Navier-Stokes solver. This type of flow is suitable for studying vortex breakdown because it is free of external, ambient disturbances and because the boundary conditions are well-defined. The results of the simulations show that the breakdown bubbles of the steady flow as well as the unsteady flow can be controlled by the rotation of the rod. Tools were developed to obtain a quantitative measure of the transient behavior of the flow field in the cavity. Transition of the flow was studied and the frequencies appearing in the time varying flow field were determined by applying a Fast Fourier Transform (FFT).

By applying Proper Orthogonal Decomposition (POD), one is able to extract a limited amount of data which characterizes a flow of interest. The modes resulting from the decomposition form a basis in the phase space on which a Galerkin projection of the equations of motion can be performed. By carrying out such a procedure one obtains a low-dimensional model consisting of a reduced set of Ordinary Differential Equations (ODE) which models the original equations. Such low-dimensional models have been constructed and used for analyzing bifurcations occurring in the flow in the lid driven cavity with a rotating rod.

A technique called the Sequential Proper Orthogonal Decomposition (SPOD) was developed to perform decompositions suitable for low-dimensional models. The SPOD is capable of transforming data organized in different sets separately while still producing orthogonal modes. Also, a method has been developed for constructing low-dimensional models with more than one free parameter. It was applied to the flow in the lid driven cavity with a rotating rod. The resulting model allows one of the free parameters to appear in the inhomogeneous boundary conditions without the addition of any constraints. This is necessary because both the driving lid and the rotating rod can be controlled simultaneously. Apparently, the results are among the first to be obtained for low-dimensional models based on projection on POD modes for more than one free parameter.

Dansk resumé

Strømningen i en lukket cylinder med roterende låg og roterende stang er blevet undersøgt ved hjælp af numeriske simuleringer med en akse-symmetrisk Navier-Stokes-løser. Denne type strømning er velegnet til studier af vortex breakdown (nedbrud af en hvirvel) på grund af fraværet af udefrakommende forstyrrelser, og fordi at randbetingelserne er veldefinerede. Resultaterne af simuleringerne viser, at recirkulationsboblerne i den stationære såvel som den instationære strømning kan styres ved hjælp af stangens rotation. Der er udviklet værktøjer til beregning af kvantitative egenskaber for transienterne i strømningsfeltet i den lukkede cylinder. Transition af strømningen er blevet undersøgt, og frekvenserne, der optræder i det tidsvarierende strømningsfelt er beregnet ved hjælp af Fast Fourier Transform (FFT).

Ved anvendelse af Proper Ortogonal Dekomposition (POD) kan man ekstrahere en begrænset mængde af data, som karakteriserer den pågældende strømning. Resultatet af dekompositionen udgør en basis i faserummet. På denne basis kan man foretage en Galerkin-projektion af bevægelsesligningerne. Herved opnås en lavdimensional model, som består af et reduceret sæt af ordinære differentialligninger, der kan fungere som en model af de oprindelige ligninger. Lavdimensionale modeller er blevet konstrueret og anvendt til at analysere bifurkationer, som optræder i strøningen i den lukkede cylinder med roterende låg og roterende stang.

En metode, som kaldes Sekventiel Proper Ortogonal Dekomposition (SPOD), er blevet udviklet med henblik på lavdimensional modellering. SPOD er i stand til separat at transformere data, som er organiseret i adskilte delmængder, på en sådan måde at de beregnede basisvektorer bliver ortogonale. Endvidere er der blevet udviklet en metode til at konstruere lavdimensionale modeller med mere end én fri parameter. Metoden er anvendt på strømningen i den lukkede cylinder med roterende låg og roterende stang. Den resulterende model tillader, at en af de frie parametre forekommer i de inhomogene randbetingelser, men uden at det er nødvendigt at tilføje yderligere betingelser. Dette er nødvendigt, fordi at både det roterende låg og den roterende stang kan styres samtidigt. De opnåede resultater er, så vidt det vides, blandt de første, der er opnået for lavdimensionale modeller baseret på projektion på en basis, som er beregnet via POD, for mere end én fri parameter.

Contents

List of Figures

List of Tables

Chapter 1

Introduction

The equations of motion are simple and well known. Yet they provide an unending source of complicated fluid motion. The researcher might try to identify structures appearing in a fluid flow and thereby attempt to understand its behavior. Perhaps the most striking development along this line of research is the recent ability to predict the motion of the fluid from structures appearing in the flow.

During the last few decades computers have become cheaper and increasingly more powerful. It has for some time been possible to sample large amounts of data from fluid flow experiments by using automated measuring equipment based on hot-wires, Laser Doppler Anemometry (LDA) and Particle Image Velocimetry (PIV). Also, today very large amounts of data are being computed by numerical solution of the Navier-Stokes equations.

By applying Proper Orthogonal Decomposition (POD), Wavelets and similar transformations, one is able to extract a limited amount of data which characterizes a flow of interest. The modes resulting from such transformations form a basis in the phase space on which a Galerkin projection of the equations of motion can be performed. By carrying out such a procedure one obtains a set of Ordinary Differential Equations (ODE) which models the original equations. The idea behind constructing a model of this type is that although the original equations have a very large number of degrees of freedom the actual solution may have only a moderate number of dimensions.

The approach of constructing low-dimensional models by applying Galerkin projection of the Navier-Stokes equations on POD modes has several shortcomings. This fact is emphasized when considering Low-dimensional models of more realistic flows. Discretization of the original partial differential equations yields a large number ODE's which are coupled through sparse coefficient matrices. Although a smaller number of ODE's can be obtained by Galerkin projection, the resulting equations are coupled in such a way that any solution variable depends on all the others. Thus, the necessary number of computations increases

quickly with the number of modes. A certain error is introduced when representing a solution by POD modes corresponding to data sampled for selected parameter values. The error tends to grow quickly for parameter which are not close to the values selected for the sampled data. Therefore, many modes are needed for a large parameter space.

The advantage of using POD modes for a low-dimensional model is that the modes are calculated in order to suit the specific problem in contrast to for instance the Fourier modes which are given a priori. Of course, this is also a disadvantage because the solution of the problem must be known before the POD modes can be found. However, the quest of data for the calculation of modes to be used in a low-dimensional model provides motivation for investigating the system which is modeled. The desire to enhance the performance and accuracy of the low-dimensional model leads to a need for more detailed and accurate data. The low-dimensional model can be viewed both as a model of a system and as a tool to present large amounts of data for a system on a concentrated form.

In present study, the goal is to carry out axisymmetric numerical simulations in order to control the steady and unsteady flow in a closed cylinder with a rotating lid and rod, construct low-dimensional models based on decomposition techniques and analyze bifurcations occurring in the flow. The study is presented in two parts. The numerical simulations are presented in the first part. The second part is concerned with the construction and analysis of the low-dimensional models.

The lid driven cavity is suitable for studying vortex breakdown because it is free of external, ambient disturbances that are often present in open flows and because the boundary conditions of the fluid mechanics problem are well-defined. Despite its wide range of technical applications, vortex breakdown is not fully understood and remains difficult to predict and control. Due to the simple geometry of the closed cavity and the existence of efficient axisymmetric Navier-Stokes solvers, this type of problem is highly suitable for numerical studies. In Chapter 2, the problem is introduced, various aspects of the steady flow are discussed and the results for the unsteady flow are presented. In order to characterize the flow for a given set of parameters, numerical simulations were carried out for a long time interval until a limiting state was obtained. The recorded data were analyzed and later utilized for both the construction and evaluation of low-dimensional models. Tools were developed to obtain a quantitative measure of the transient behavior of the flow field in the cavity. The frequencies appearing in the time varying flow field were determined by applying a Fast Fourier Transform (FFT) and the peaks were located in the calculated FFT amplitudes.

Constructing low-dimensional models of the flow in a lid driven cavity with a rotating rod has indicated several problems and served as a source of inspiration for enhancing the modeling procedure. The Sequential Proper Orthogonal Decomposition (SPOD), which will

be introduced in Chapter 3, is a technique which was developed to perform decompositions suitable for low-dimensional models. The SPOD is capable of transforming data organized in different sets separately while still producing orthogonal modes. This feature is desirable because the POD modes with the largest eigenvalues represent data corresponding to large energy better than data corresponding to small energy. Thus, dynamically important data might not be represented unless it is either transformed separately or weighted in some fashion. An interesting contribution to the construction of low-dimensional models is presented in Chapter 4. It is a method for satisfying inhomogeneous boundary conditions, in which one of the free parameters appears, without the addition of any constraints. This is necessary because the model has two free parameters in contrast to earlier models with only one free parameter. The problem arises because both the driving lid and the rotating rod can be controlled simultaneously.

In the beginning of Chapter 5, a validation is performed by comparing solutions of the current type of low-dimensional model to the results obtained in the earlier work of E. A. Christensen *et al.* [10]. In order to accomplish this, a special version of the low-dimensional model was implemented for the lid driven cavity without a rod. The performance of this version of the model compares favorably with the earlier model of Christensen *et al.* The low-dimensional models of the flow in the lid driven cavity with a rotating rod are presented. The transition occurring for varying parameter values is studied and the results are compared to the original results obtained for the full numerical simulations. The effect of different methods of data sampling and variations of the decomposition procedure is investigated. The eigenvalue spectra of the SPOD are used for estimating an upper limit for the number of modes which can be included in the models. A low-dimensional model, which is operational with two varying parameters, is utilized for Hopf continuation. The resulting critical curve is compared to the data obtained for the full model. For one constant parameter, the accuracy of the critical values obtained for the varying parameter are superior to the results obtained for simpler models. Within the literature, no results have previously been reported for low-dimensional models based on projection on POD modes for more than one free parameter.

Part I

The lid driven cavity with a rotating rod

Chapter 2

The closed cylinder with a rotating lid and rod

2.1 Background

The flow in a closed cylinder with a rotating lid was originally introduced experimentally by Vogel [31] and Ronnenberg [25], and was later studied intensively by experiment in the work of Escudier [15]. Although it has appeared much less frequently in the literature than the flow between rotating concentric cylinders it has gained increased popularity.

The flow in a closed cylinder with a rotating lid is suitable for studying vortex breakdown because it is free of external, ambient disturbances that are often present in open flows and because the boundary conditions of the fluid mechanics problem are well-defined. One has to keep in mind, however, that the flow is affected by the walls, and the lack of through-flow in the cavity makes it difficult to transfer results directly to realistic applications.

Due to the simple geometry of the closed cavity and the existence of efficient axisymmetric Navier-Stokes solvers, this type of problem is highly suitable for numerical studies. Recently, the transition scenario in the flow has been studied numerically by Sørensen and Christensen [28].

Despite its wide range of technical applications, vortex breakdown is not fully understood and remains difficult to predict and control. Vortex breakdown in the closed cavity flow was first controlled by means of a rotating axial rod by Hussain *et al.* [18] who reported flow visualization experiments and an presented an analytical model aimed at explaining the observed phenomena. Their analytical model is based on the velocities being independent on the axial coordinate, which prevents modeling of breakdown bubbles. In contrast, the present calculations show a change in the azimuthal velocity near the lid and near the bottom.

Mullin *et al.* [22] performed a numerical investigation of a slightly different configuration

in which both end-walls rotate. In particular, they considered the case of an inner cylinder rotating with the end-walls and the case of a stationary inner cylinder. A recent experimental and numerical study was performed by Mullin *et al.* [23] of a rotating cylinder of fluid where one end-wall is rotated. The results show that the addition of a sloping inner cylinder has a dramatic effect on the recirculation such that it can either be intensified or suppressed. One of their main conclusions is that the onset of the recirculation bubble is mainly unaffected by the presence of a small straight rotating inner cylinder (attached to the rotating bottom end-wall). In contrast, the current study shows that presence of a small straight inner cylinder, which is rotating independently of the end-walls, has an effect on the recirculation bubbles which is just as significant as the presence of the sloped inner cylinder investigated by Mullin *et al.*

The goal of the present study is to carry out axisymmetric numerical simulations in order to control the steady and the unsteady flow in a closed cylinder with a rotating lid and rod. The data resulting from the investigation will be used to construct low-dimensional models based on decomposition techniques with the purpose of analyzing bifurcations occurring in the flow.

2.2 Physics

The basic configuration consisting of a closed cylinder with a rotating lid (without any rod) is shown in Fig. 2.1. The rotating lid has the effect of setting the fluid into a rotating motion

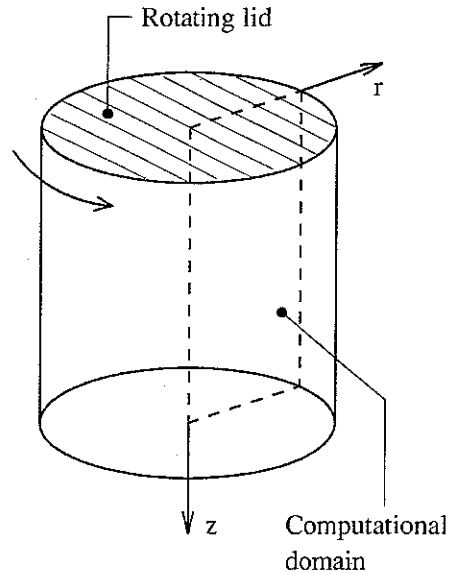

Figure 2.1: Cylindrical cavity with rotating lid. The considered domain is a plane in between the center axis and the wall.

around the center axis. In addition, it drives the fluid close to the lid away from the center thereby causing a meridional circulation. The fluid leaving the area near the lid then travels downwards along the outer wall, turns inwards near the fixed bottom, rises vertically close to the center axis and returns to the area near the rotating lid. Along this path, the azimuthal velocity component of the fluid undergoes changes and the fluid rising along the center axis forms a strong swirling vortex core. The vortex may experience a vortex breakdown which manifests itself by one or several bubble-like zones of recirculating fluid, called breakdown bubbles, that are located along the center axis.

The model parameters governing the flow are the aspect ratio

$$\lambda = H/R, \tag{2.1}$$

where H and R denote the height and radius of the cylinder, respectively, and the Reynolds number

$$\mathrm{Re}_{lid} = \frac{v_{lid} R}{\nu}, \tag{2.2}$$

where v_{lid} refers to the tip velocity of the lid and ν is the kinematic viscosity.

Escudier [15] identified boundaries within the $(\lambda, \mathrm{Re}_{lid})$-plane in which zero, one, two or three breakdown bubbles occur on the center axis. In addition, for any given aspect ratio, there is a critical Reynolds number, $\mathrm{Re}_c(\lambda)$, at which the flow becomes unsteady and starts to oscillate. Escudier found that for Reynolds numbers just above $\mathrm{Re}_c(\lambda)$ the oscillation is periodic and axial provided that $\lambda < 3.1$.

The present study is limited to treat only the case of a cylinder with an aspect ratio of 2.0. The transition to three-dimensional flow for this aspect ratio has been studied numerically by Sørensen *et al.* [29] They found that the flow remains axisymmetric in a substantial part of the unsteady domain.

For this particular aspect ratio value, the only possible configurations in the steady domain consist of zero, one or two breakdown bubbles. The streamlines of the flow obtained from a steady state numerical simulation are represented in Fig. 2.2b. In Fig. 2.2 this result is qualitatively compared to an experimental visualization (a) of Buchhave *et al.* [8]

As shown in Sørensen and Ta Phuoc [27] the axisymmetric flow is accurately described by transport equations for vorticity and azimuthal velocity, and a Poisson equation for the stream function. This has been exploited this to produce a numerical model for simulating the flow.

In order to control the vortex breakdown, that is either suppress or enhance the formation of breakdown bubbles, a thin rod with radius $\delta = 0.02R$ was implemented in the numerical model (see Fig. 2.3). As seen in 2.6.1, rotating the rod has a significant effect on the formation of breakdown bubbles. By rotating the rod in the same direction as the lid, the appearance

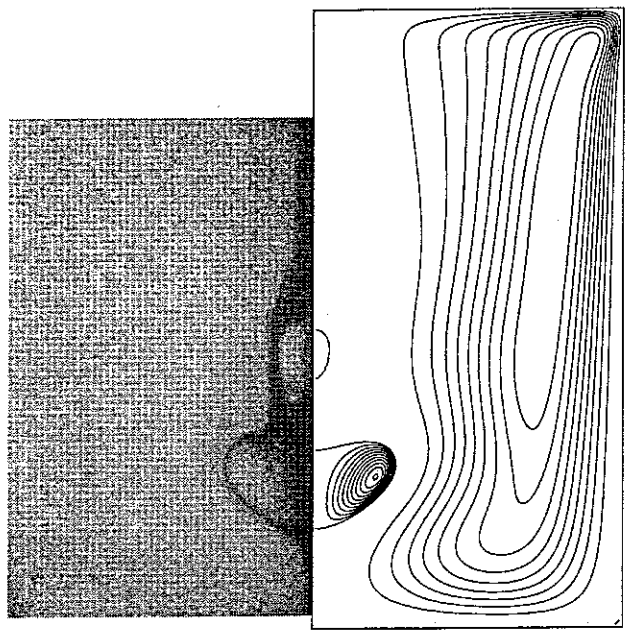

(a) (b)

Figure 2.2: Comparison between experiment and computed stream lines for $\mathrm{Re}_{lid} = 2200$. (a) Visualization, particles appear as white spots in a laser sheet. (b) Stream lines from simulation.

of vortex breakdown bubbles can be prevented, whereas counter-rotating the rod results in an amplification of the bubbles.

A simple dimensional analysis of this problem yields four model parameters. These are, besides the aspect ratio, λ, and the Reynolds number, Re_{lid}, the ratio between the radius of the rod and the cylinder,

$$\xi = \delta / R, \tag{2.3}$$

and the ratio between the Reynolds number of the rod and the cylinder,

$$\gamma = \frac{\mathrm{Re}_\delta}{\mathrm{Re}_{lid}} = \frac{v_\delta \delta}{v_{lid} R}, \tag{2.4}$$

where v_δ is the surface velocity of the rod. Re_δ is the Reynolds number based on the surface velocity of the rod. To limit the number of control parameters, set $\xi = 0.02$. Since $\lambda = 2.0$, the two remaining model parameters are therefore γ and Re_{lid}.

2.3 The governing equations

As shown in Appendix A, the Navier-Stokes equations and the continuity equation can be reformulated in terms of velocity, $\mathbf{v}$, vorticity,

$$\boldsymbol{\omega} = \nabla \times \mathbf{v}, \tag{2.5}$$

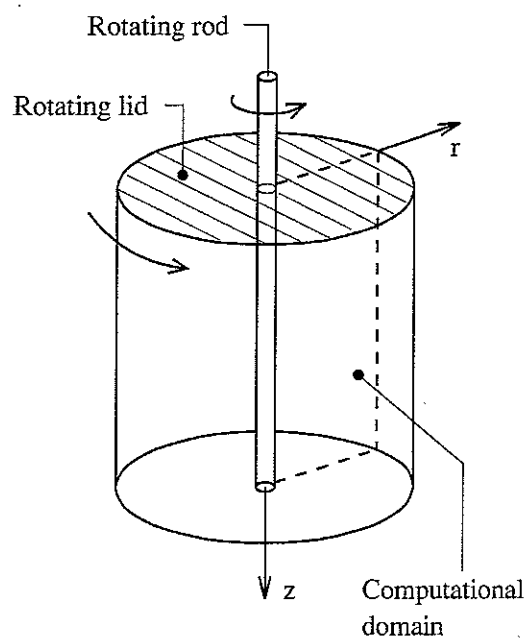

Figure 2.3: Cylindrical cavity with rotating lid and rotating rod. The considered domain is a plane in between the rod and the wall.

and a covariant vector stream function,

$$\mathbf{v} = -\nabla \times \boldsymbol{\psi}, \tag{2.6}$$

For rotational symmetry and utilizing cylindrical coordinates, it is only necessary to consider the azimuthal components, which are called v, ω and ψ respectively. The radial and axial components of the velocity are then given by

$$v_r = \frac{1}{r}\frac{\partial \psi}{\partial z}, \quad v_z = -\frac{1}{r}\frac{\partial \psi}{\partial r}. \tag{2.7}$$

This leads to a formulation of the governing equations consisting of the equations (A.47), (A.61) and (A.69). The equations are restated here as the Poisson equation,

$$r\omega = \frac{\partial^2 \psi}{\partial r^2} - \frac{1}{r}\frac{\partial \psi}{\partial r} + \frac{\partial^2 \psi}{\partial z^2}, \tag{2.8}$$

the vorticity transport equation,

$$\frac{\partial \omega}{\partial t} = -\frac{\partial}{\partial r}(v_r \omega) - \frac{\partial}{\partial z}(v_z \omega) + \frac{1}{r}\frac{\partial}{\partial z}(v_\theta^2) + \frac{1}{\mathrm{Re}}\left(-\frac{1}{r^2}\omega + \frac{1}{r}\frac{\partial}{\partial r}\left(r\frac{\partial \omega}{\partial r}\right) + \frac{\partial^2 \omega}{\partial z^2}\right), \tag{2.9}$$

and the azimuthal velocity transport equation,

$$\frac{\partial}{\partial t} v_\theta = -\frac{\partial}{\partial r}(v_r v_\theta) - \frac{\partial}{\partial z}(v_z v_\theta) - \frac{2}{r} v_r v_\theta + \frac{1}{\mathrm{Re}}\left(-\frac{1}{r^2} v_\theta + \frac{1}{r}\frac{\partial}{\partial r}\left(r\frac{\partial v_\theta}{\partial r}\right) + \frac{\partial^2 v_\theta}{\partial z^2}\right). \tag{2.10}$$

In addition, according to the work of Daube *et al.* [12], there is a constraint (A.13), which, for the lid driven cavity with a rod, has the form

$$\int_\Gamma \left(\frac{\partial}{\partial t}\mathbf{v} - \mathbf{v} \times (\nabla \times \mathbf{v}) + \frac{1}{\mathrm{Re}} \nabla \times (\nabla \times \mathbf{v})\right) \cdot d\mathbf{l} = 0, \tag{2.11}$$

where Γ is a loop around the rod. The constraint is introduced because the pressure is eliminated by differentiation when deriving the vorticity transport equation. However, as shown in Appendix A, the constraint is automatically satisfied because the azimuthal velocity equation is solved directly. This ensures the existence of a pressure function.

2.4 Boundary conditions

For the closed cylinder with a rotating lid the following boundary conditions apply according to Sørensen and Ta Phuoc [27]:

Symmetry axis

$$\psi = v_r = \omega = \frac{\partial \psi}{\partial r} = 0, \; v_\theta = 0, \; \frac{\partial^2 \psi}{\partial r^2} = -v_z. \tag{2.12}$$

Cylinder wall

$$\psi = v_r = v_z = \frac{\partial \psi}{\partial r} = 0, \; v_\theta = 0, \; \frac{\partial^2 \psi}{\partial r^2} = r\omega. \tag{2.13}$$

Rotating lid

$$\psi = v_r = v_z = \frac{\partial \psi}{\partial z} = 0, \; v_\theta = r, \; \frac{\partial^2 \psi}{\partial z^2} = r\omega. \tag{2.14}$$

Fixed bottom

$$\psi = v_r = v_z = \frac{\partial \psi}{\partial z} = 0, \; v_\theta = 0, \; \frac{\partial^2 \psi}{\partial z^2} = r\omega. \tag{2.15}$$

The rotating rod with radius δ is implemented by replacing the boundary conditions for the symmetry axis by appropriate no-slip conditions

$$\psi = v_r = v_z = \frac{\partial \psi}{\partial r} = 0, \; v_\theta = v_\delta, \; \frac{\partial^2 \psi}{\partial r^2} = r\omega, \; \text{for } r = \frac{\delta}{R}. \tag{2.16}$$

2.5 Numerical implementation of the Navier-Stokes solver

The transport equations are discretized by a second order central difference scheme. The Poisson equation is discretized to fourth order accuracy using three-point Hermitian expressions for the derivatives of the stream function. The boundary conditions were implemented by using Taylor series expansions into the flow domain. The transport equations were solved alternately with the Poisson equation. For each equation, every time step was split into two steps, one time step for the z-direction and one time step for the r-direction, employing the ADI technique. Further details about the numerical implementation, including references, can be found in Sørensen and Ta Phuoc [27].

The ability of the applied numerical procedure to correctly reproduce the flow structures is shown in Fig. 2.2 which displays a comparison between PIV photo (a) from Buchhave *et al.* [8] and computed stream lines (b). A detailed comparison between numerical results

and measurements, showing excellent agreement, is reported in Sørensen and Ta Phuoc [27]. They validated the basic numerical code (without the rod) against visualizations and velocity profiles obtained by using LDA. We thus assume that the numerical method is thoroughly validated, and we use it to gain insight into the physical problem. When the symmetry condition with respect to the center axis is replaced by a no-slip boundary condition, it seems reasonable to assume that the no-slip boundary condition performs equally well for the rod and the outer wall.

By investigating different grid sizes, a grid resolution of $\Delta r = \Delta z = 0.01$ was found to be sufficient within the parameter range of interest in this study. An example for the rod is given in Fig. 2.4.

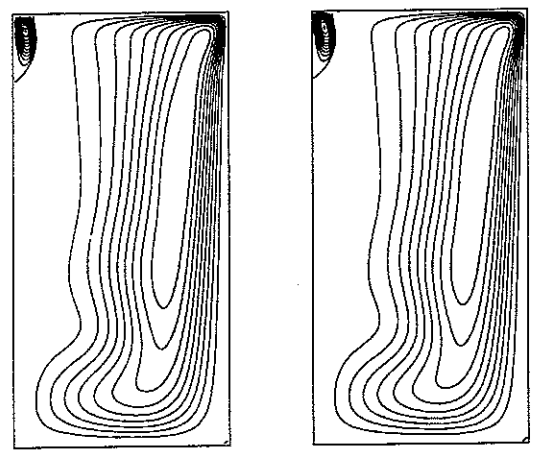

(a) (b)

Figure 2.4: A study of the grid size effects for the rod with $\gamma = 0.010$ at $\mathrm{Re}_{lid} = 2200$. (a) Grid with 201x101 points, (b) grid with 281x141 points.

2.6 Steady flow

2.6.1 The effect of the rotating rod

The effect of co-rotation ($\gamma > 0$) and counter-rotation ($\gamma < 0$) of the rod relative to the direction of the rotation of the lid for $\mathrm{Re}_{lid} = 2200$ is shown in Fig. 2.5. Co-rotation causes the smaller breakdown bubble to disappear at a γ-value within the interval $0.001 < \gamma < 0.002$ and the larger breakdown bubble to disappear at a γ-value within $0.004 < \gamma < 0.005$. Note the appearance of a small vortex in the upper left hand corner of the computational domain close to the intersection between the rod and the lid. In contrast, counter-rotation causes the size of both breakdown bubbles to increase and the flow becomes unsteady at a γ-value in the range of $-0.007 < \gamma < -0.006$. But, also counter-rotation creates a vortex in the upper left hand

corner of the computational domain. Thus, both co-rotation and counter-rotation are seen to have a dramatic effect on the flow structure near the rod. This behavior is similar to the qualitative experimental observations of Hussain *et al.* [18]. They performed visualizations for $\mathrm{Re}_{lid} = 2720, H/R = 3.25$ and $\xi = 0.0416$ in which they observed three breakdown bubbles for a fixed rod. As co-rotation of the rod was increased, the bubbles became progressively smaller in size and finally disappeared. For slow counter-rotation of the rod, the bubbles became more prominent and wider than those for the fixed rod. Furthermore, the observed effect of the rotating rod on the bubbles is similar to the effect which was obtained numerically and experimentally by Mullin *et al.* for an inner cylinder with a sloped wall.

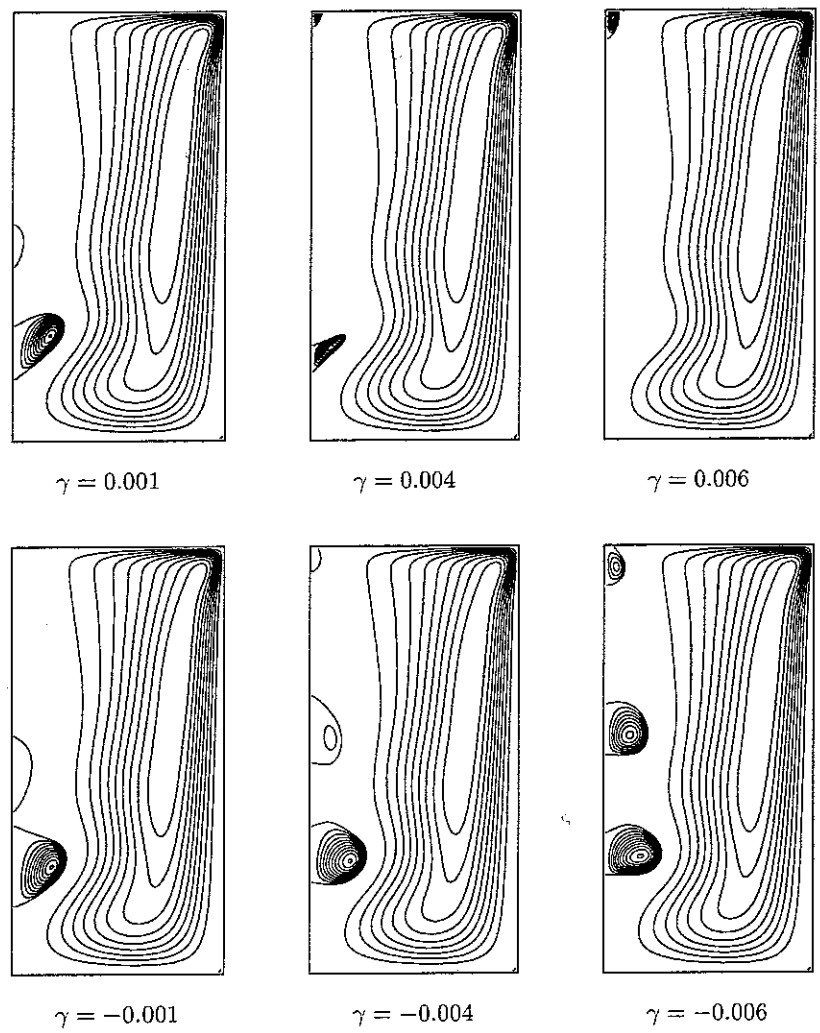

Figure 2.5: The effect of co-rotation (above) and counter-rotation (below) of the rod for $\mathrm{Re}_{lid} = 2200$.

2.6.2 Parametric study for the cavity with a rod

Numerical simulations of the flow in the cavity with a rod have been carried out for varying parameters, $(\mathrm{Re}_{lid}, \gamma)$. Within the steady domain the breakdown bubbles were counted via the stream function for each investigated parameter combination. The recorded number of breakdown bubbles did not include any vortex appearing in the upper left corner of the computational domain near the intersection between the rod and the lid. The results are shown in the diagram in Fig. 2.6.

The horizontal axis corresponds to Re_{lid} and the vertical axis corresponds to γ. Each investigated parameter combination is equivalent to a point in the diagram. Within the steady domain each point is marked to show the occurrence of zero, one, or two breakdown bubbles in the flow. Any points within the unsteady domain are shown as crosses.

The boundaries among the domains and the transition between steady and unsteady flow are indicated by lines. In order to limit the number of computations most of the points were located in areas where topological changes or transition to unsteady flow were expected.

Independently of whether the rod is rotating or not, the flow is unsteady for Reynolds numbers above 2700. For Reynolds numbers above 1500 the flow is unsteady for values of γ above 0.031 and below -0.016. No simulations were carried out for Reynolds numbers less than 1500. The flow becomes unsteady at a critical line, shown in the figure as a dashed line, which extends in a curve from a point near the upper left corner of the diagram to a point near the lower left corner. Within the steady domain, six distinct domains corresponding to different numbers of bubbles can be identified. The uppermost domain corresponds to zero bubbles. Below this domain, a domain of one bubble is located. Below this domain, the domain of two bubbles is located. Inside this domain, a small domain of one bubble can be found. It represents the phenomenon of two breakdown bubbles having merged to form one large bubble. Below the domain of two bubbles, the flow becomes unsteady for Reynolds numbers greater than a value in between 1800 and 1900. For Reynolds numbers less than this value, a domain of one bubble can be found. Below this domain an L-shaped domain of zero bubbles is found. Below and on the right hand side of this domain, the flow is unsteady. From the diagram we learn that the topology of the stream lines can be controlled by changing γ and Re_{lid}. In particular, it is possible to remove the breakdown bubbles by co-rotation of the rod for all investigated Reynolds numbers up to a value above 2400. But it is also possible to remove the breakdown bubbles by counter-rotation provided that Re_{lid} is small enough. In Fig. 2.6 this is shown for $\mathrm{Re}_{lid} = 1500$.

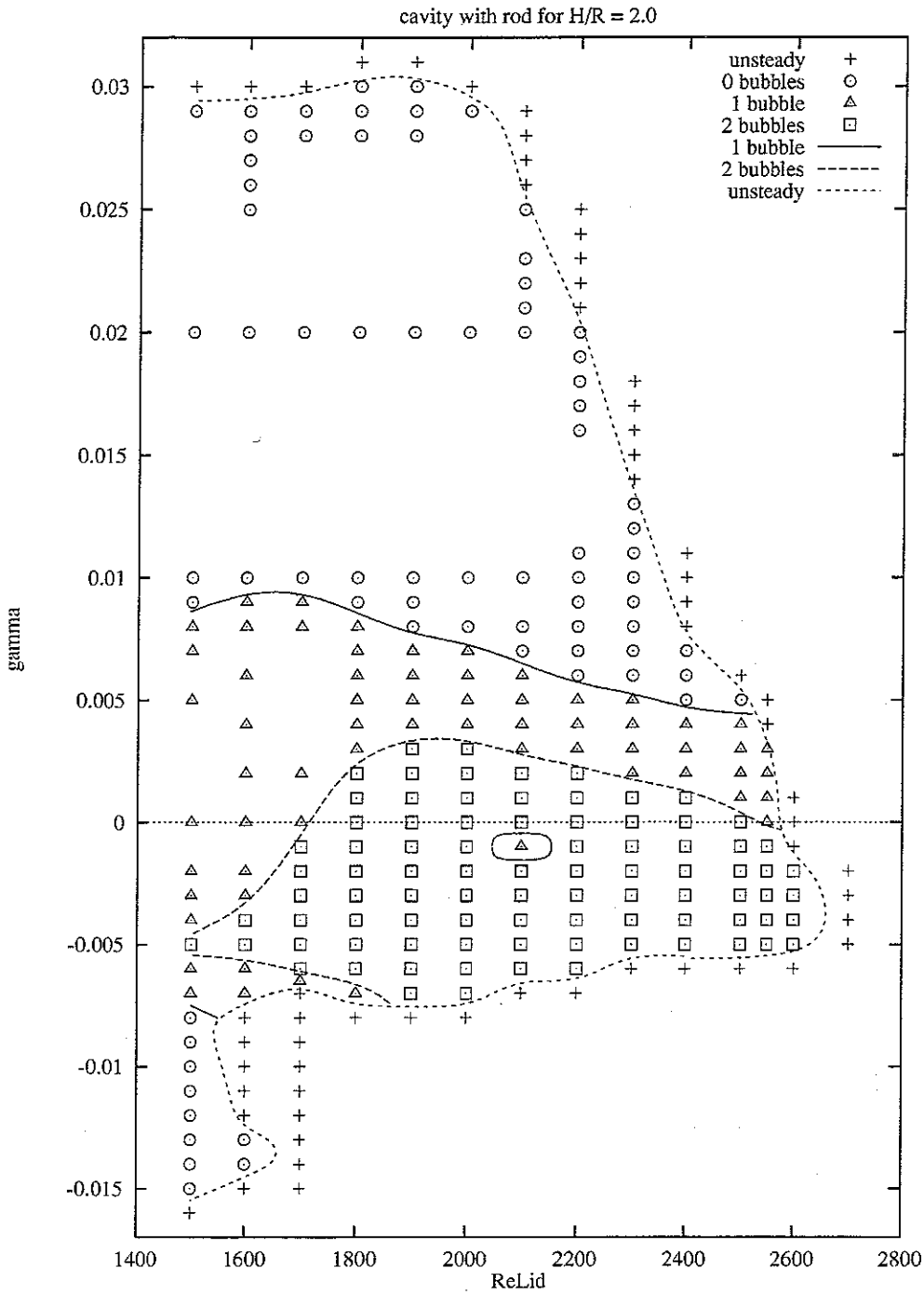

Figure 2.6: Parametric study for the cavity with rod. For a series of values of Re_{lid} and γ the number of breakdown bubbles were counted by using the stream function. The lines are meant to aid in distinguishing among the domains of different behavior and do not represent computed data.

For $\mathrm{Re}_{lid} = 1600$ the diagram displays a rather complicated behavior. Increasing the rotational speed of a counter-rotating rod ($\gamma < 0$), the flow becomes unsteady at $\gamma = -0.008$, re-stabilizes with no breakdown bubbles at $\gamma = -0.013$, and becomes steady once again at $\gamma = -0.015$. Thus, the mechanism behind the observed behavior does not lend itself to an easy explanation.

Escudier [15] reports the range of two breakdown bubbles at $\lambda = 2$ to be $1850 < \mathrm{Re}_{lid} < 2240$ for the cylinder without a rod. We find that by introducing a fixed rod with $\xi = 0.02$ the range of two breakdown bubbles is expanded to become about $1800 < \mathrm{Re}_{lid} < 2555$.

The stream line topology for the closed cavity with a rotating lid can be viewed within a mathematical framework that describes all kinds of behavior which are possible. This work has been carried out by Brøns [5], Hartnack [17], Brøns and Hartnack [6] and Brøns *et al.* [7]. Indeed, the method used by Brøns [5] and Hartnack [17] can also be utilized for the cavity with a rod as it fully describes the allowed kinds of behavior near a boundary with a no-slip condition. Furthermore, the method for the interior of the flow can be applied. For instance, the merging of two breakdown bubbles shown by Brøns and Hartnack [6] can be observed for the parameters $(\mathrm{Re}_{lid}, \gamma) = (2100, -0.001)$ in Fig. 2.6. According to their predictions, the merged breakdown bubble should contain two recirculating areas. This is exactly what is observed.

2.7 Unsteady flow

2.7.1 Overview of investigation

The purpose of this study is to investigate the transition from steady to unsteady flow and the transition taking place within the unsteady region close to the steady region. In order to characterize the flow for a given set of parameters, numerical simulations were carried out for a long time interval until a limiting state was obtained.

As it is the nature of the flow to yield very long transients for parameter values close to a critical point of the limiting flow, it was necessary to limit the investigated parameter space in order to obtain data near critical points. The parameters of main interest are Re_{lid} and γ. Thus, the thickness of the rod was fixed by letting $\xi = 0.02$ and an aspect ratio of 2.0 was chosen for the cylinder. Escudier [15] reported the flow in the cavity without the rod to become unsteady at the critical Reynolds number via a precession of the vortex core for aspect ratios above 3.1. Hence, the aspect ratio for the present study was chosen well below this value to keep the flow axisymmetric.

The region shown in Fig. 2.7 was chosen in the parameter space near the transition from steady to unsteady flow for a fixed rod.

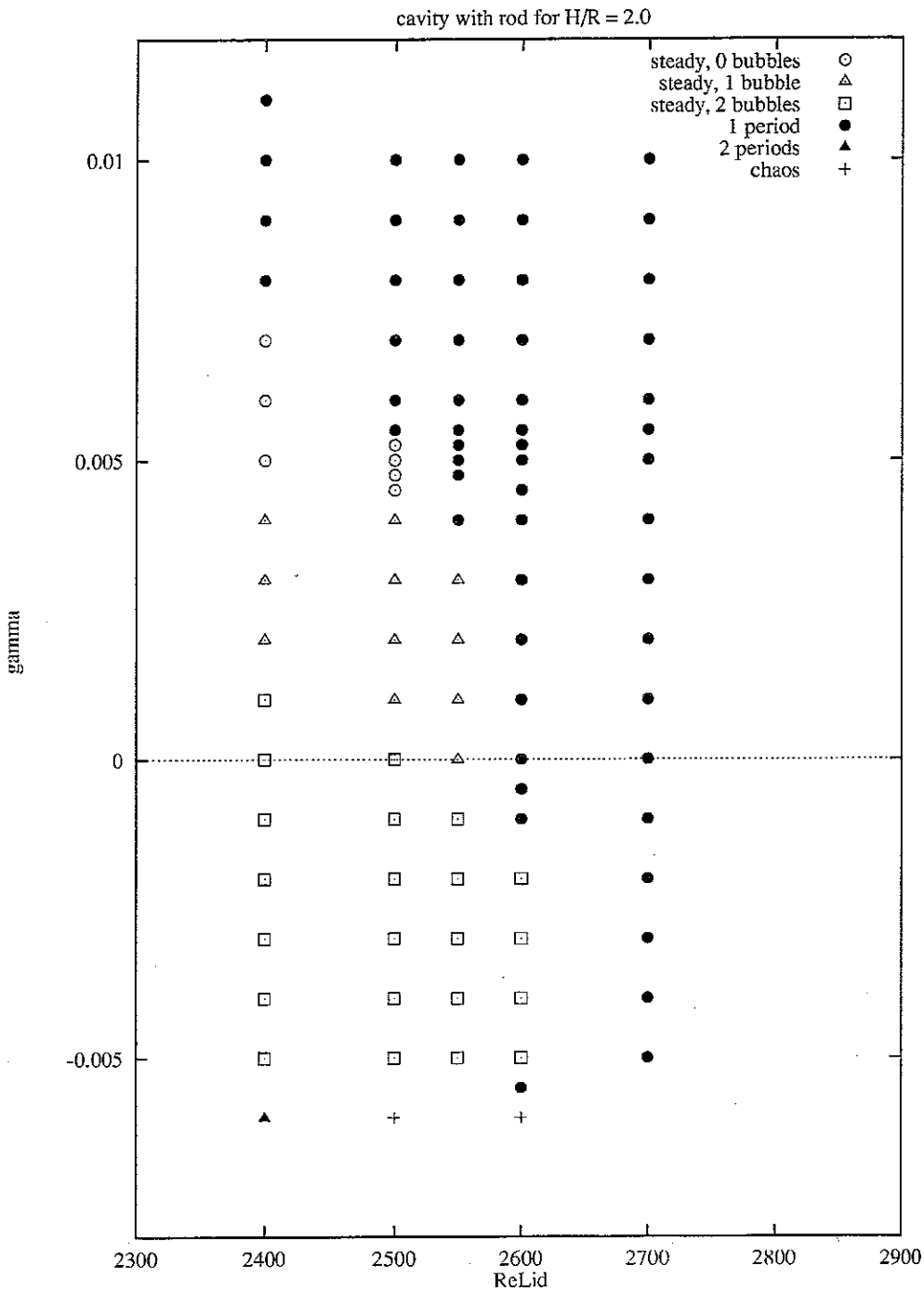

Figure 2.7: Characterization of the unsteady flow in the cavity with a rod near the steady region. For a series of values of Re_{lid} and γ the number of periods of the time varying flow field was determined.

The horizontal axis represents the Reynolds number, Re_{lid}, and the vertical represents γ. Data is shown for Reynolds numbers between 2400 and 2700 and for γ between -0.006 and 0.011. At $\mathrm{Re}_{lid} = 2700$ the flow is unsteady. For $2400 \leq \mathrm{Re}_{lid} \leq 2600$ the flow is steady between an upper and a lower critical γ and otherwise unsteady. The method of determining whether the flow is steady or unsteady is discussed further in 2.7.4.

For most of the parameter values in the shown unsteady region the time variation of the flow field has one period corresponding to a basic frequency. Some parameter values yield higher harmonics that co-exist with the basic frequency. In the next subsection it is explained how the Fast Fourier Transform was applied to enable detection of the frequencies in the unsteady flow field. In 2.7.3 the method of determining the peaks is accounted for.

The higher harmonics have frequencies that are multiples of the basic frequency. Where a single basic frequency exists the legend in the figure indicates one period.

2.7.2 Application of FFT

The frequencies appearing in the time varying flow field were determined by applying a Fast Fourier Transform (FFT) with a Hamming window to data ensembles consisting of 2^{15} or 2^{16} samples of the axial velocity at the monitor point $(0.67, 0.11)$. The number of sampled points covered several periods corresponding to the lowest occurring frequency. The samples were equidistant in time and separated by time intervals of $\Delta t = 0.04$. The sampling frequency was sufficiently high so that aliasing was not encountered.

The Hamming Window is defined by

$$H(j) = (1 - a) - a \cos \frac{2\pi j}{N - 1}, \; j = 0, \; \ldots, \; N - 1 \tag{2.17}$$

where $a = 0.46$. Before applying the Hamming window, the mean value of the ensemble data was subtracted from each data point.

A portable scientific Cray library, sciport, was used to perform the FFT. The amplitude (i.e. the square root of the energy) as a function of frequency was stored as the result.

An example of a time history of the axial velocity in the monitoring point for the parameters $(\mathrm{Re}_{lid}, \gamma) = (2650, 0.0)$ is shown in 2.8. Only the first 100000 time steps corresponding to a dimensionless time interval of $\Delta t = 4000$ are shown. After 133000 iterations the unsteady flow was considered to have reached a limiting state and a data ensemble consisting of 2^{16} time steps was sampled. The output of the described FFT procedure is shown in Fig. 2.9. The main frequency is determined by the largest peak at $f_1 = 0.0379$. The first harmonic is given by the peak at the frequency $f_2 = 0.0759$.

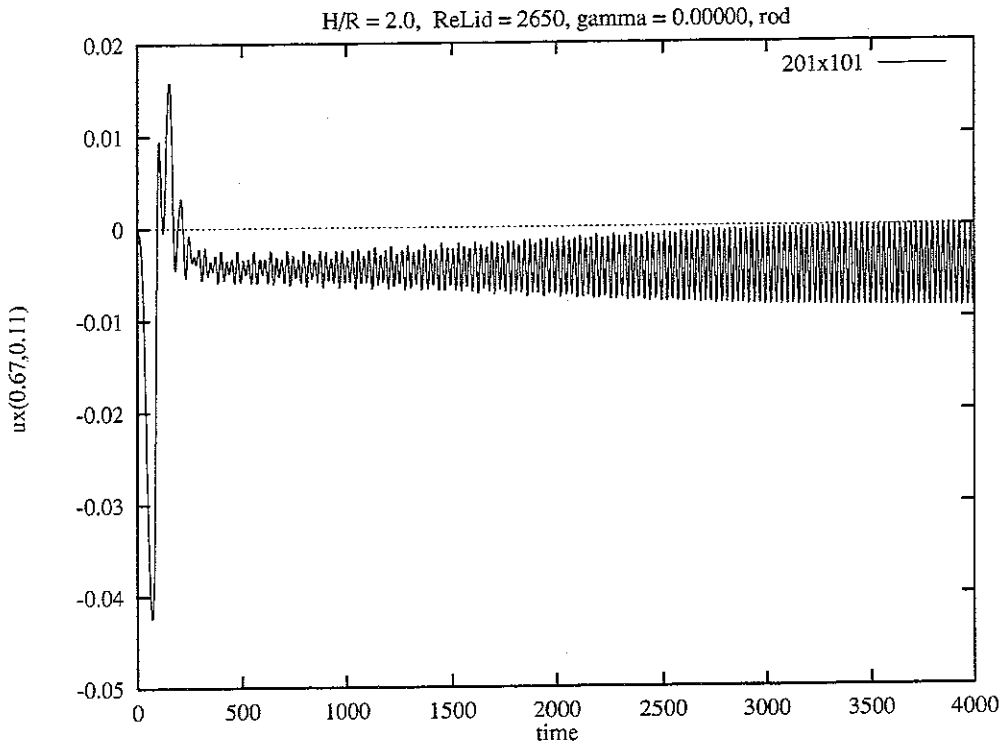

Figure 2.8: A time history of the axial velocity for the parameters $\mathrm{Re}_{lid} = 2650,\ \gamma = 0.000$.

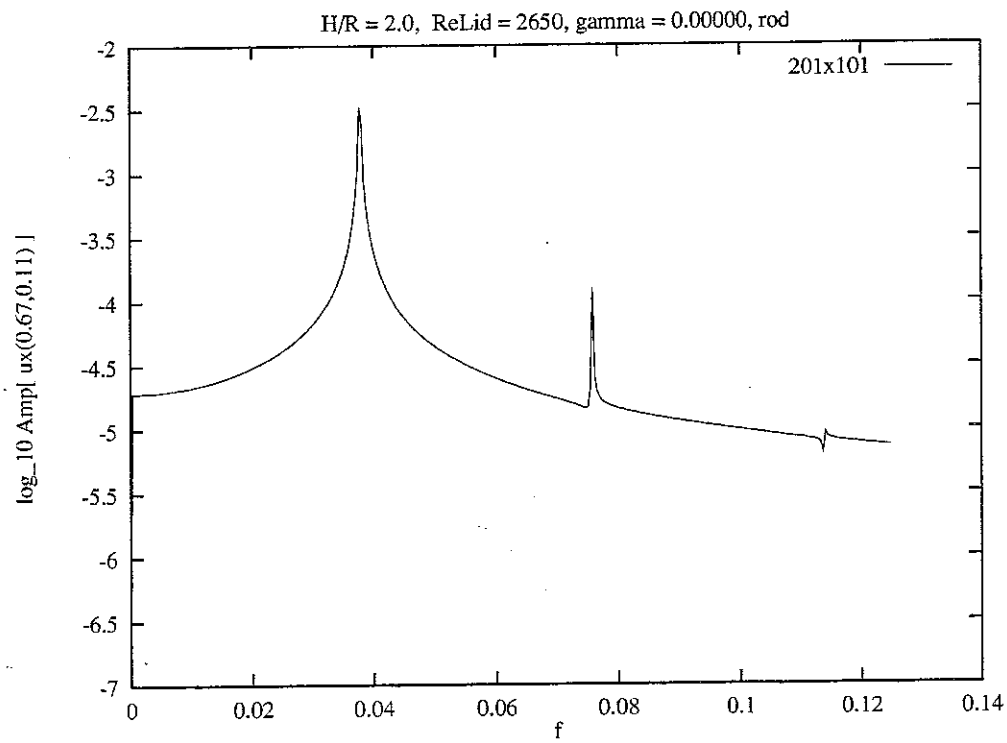

Figure 2.9: FFT amplitude of the axial velocity as a function of frequency for the parameters $\mathrm{Re}_{lid} = 2650,\ \gamma = 0.000$.

2.7.3 Determining peaks in the FFT amplitudes

A computer program, peakf, was written with the purpose of locating the peaks in the calculated FFT amplitudes. In this way the frequencies appearing in the time varying flow were found at the frequencies of the peaks. The principle used was to compare the levels of the logarithm of the amplitude for increased values of the frequency. Whenever a local maximum was encountered it had to satisfy two criteria in order to be recognized as a peak:

1. In order to avoid spurious peaks resulting from noise the local maximum was required to be greater than the mean level defined as

$$\langle \log_{10} A(f) \rangle_f = \frac{1}{N} \sum_{i=1}^{N} \log_{10} A(f_i) \tag{2.18}$$

2. For some parameter values $(\mathrm{Re}_{lid}, \gamma)$ the cost of reaching a limiting state of the time varying flow was prohibitively high. Hence, small peaks of diminishing transient signals were ignored by requiring both of the differences between the local maximum and the nearest local minimums to be greater than a predefined threshold value, i.e.

$$\log_{10} A(f_{peak}) - \log_{10} A(f_{min1}) > T \tag{2.19}$$

$$\log_{10} A(f_{peak}) - \log_{10} A(f_{min2}) > T. \tag{2.20}$$

A value of $T = 0.6$ was used.

Because of the discrete nature of the frequencies output by the FFT algorithm, the local maximum and the two neighboring points of each peak were fitted to a parabola via

$$f = f_j + (f_{j-1} - f_{j+1}) \frac{\ln A_{j-1} - \ln A_{j+1}}{2(ln A_{j-1} + \ln A_{j+1} - \ln A_j)} \tag{2.21}$$

This expression can be considered as a Gaussian interpolation formula based on the amplitude A.

2.7.4 Determining transient behavior

In order to obtain a quantitative measure of the transient behavior of the flow field in the cavity, a computer program, rmsham, was utilized. The idea was to calculate the square root of a filtered variance of the time history of interest within a Hamming window of a fixed size. Thus, a Root Mean Square (RMS) value was obtained for each time value at which the window was positioned.

Defining

$$p = \sum_{i=0}^{n-1} h_i, \tag{2.22}$$

where $h_i = H(i)$ is the Hamming window given by Eq. 2.17, and defining

$$\mu_j = \frac{1}{p}\sum_{i=0}^{n-1} h_i x_{i+j}, \tag{2.23}$$

the filtered variance is given by

$$v_j = \frac{1}{p}\sum_{i=0}^{n-1} h_i(x_{i+j} - \mu_j) = \frac{1}{p}\sum_{i=0}^{n-1} h_i x_{i+j}^2 - \left[\frac{1}{p}\sum_{i=0}^{n-1} h_i x_{i+j}\right]^2. \tag{2.24}$$

As the RMS value as a function of time determined by this method was found to be oscillating, depending on the size of the window, a post filtering procedure was applied via the expression

$$\eta_k = \frac{1}{q}\sum_{j=0}^{m-1} h_j\sqrt{v_{j+k}} \tag{2.25}$$

where

$$q = \sum_{j=0}^{m-1} h_j, \tag{2.26}$$

with $h_j = H(j)$, $N = m$, given by the Hamming window 2.17.

By plotting (t_k, η_k) the transient behavior of the flow field could be determined. If η_k approached zero, the flow was characterized as being steady. If η_k settled at a non-zero value, the flow was unsteady and a qualitative RMS level was then given by the limit of η_k. In particular, it was possible to decide if more iterations were needed in order to approach a limiting state of the flow field.

The RMS level as a function of time was calculated for the time history shown in Fig. 2.8, i.e. the time history of the axial velocity in the monitoring point for $(\mathrm{Re}_{lid}, \gamma) = (2650, 0.0)$. The result is shown in Fig. 2.10 which depicts logarithm of the RMS level as a function of time. The flow is observed be unsteady. It approaches a limiting unsteady state with an RMS level of $10^{-2.49} = 0.00321$. According to Fig. 2.9 the unsteady motion is dominated by an oscillation with the basic frequency. As the amplitude is constant, it should be proportional to the RMS level with a factor of $\sqrt{2}$ (because the RMS level is the square root of the integral of a squared harmonic function), i.e. $A = \mathrm{RMS}\sqrt{2} = 0.00454$. The distance between an upper and a lower peak of the original time history should be $2A = 0.00908$. By inspection of Fig. 2.8 this is easily verified.

The time history shown in Fig. 2.11 indicates that the flow is steady for the parameters $(\mathrm{Re}_{lid}, \gamma) = (2300, 0.0)$.

However, it can be hard to judge from the time history if a sufficient number of iterations have been carried out in order to reach the limiting state of the flow. In Fig. 2.12 the RMS level as a function of time is shown. Upon reaching an RMS level of 10^{-10} the RMS level starts to fluctuate due to numerical noise. Thus no improvement of the final state can be obtained by further iterations.

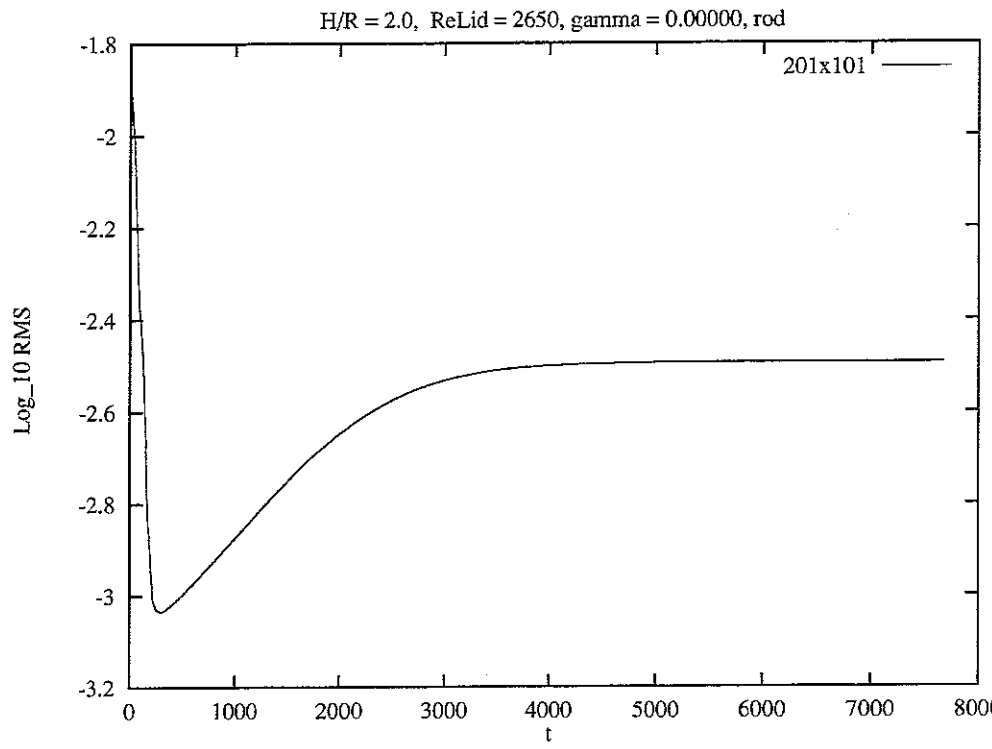

Figure 2.10: RMS level as a function of time for the parameters $\mathrm{Re}_{lid} = 2650,\ \gamma = 0.000$.

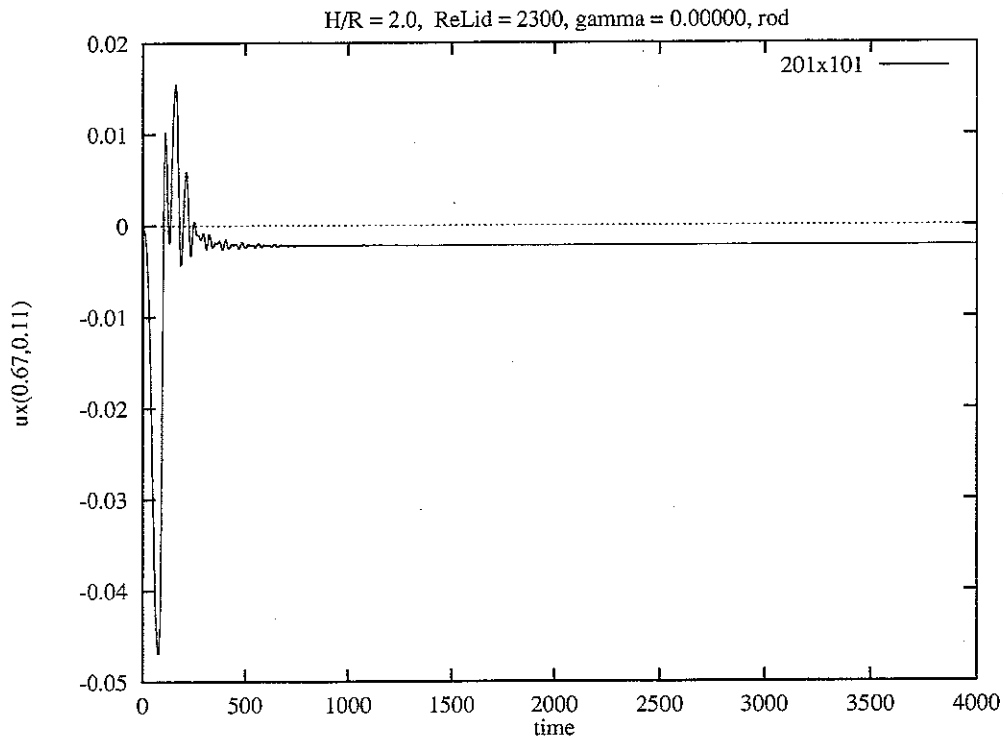

Figure 2.11: A time history of the axial velocity for the parameters $\mathrm{Re}_{lid} = 2300,\ \gamma = 0.000$.

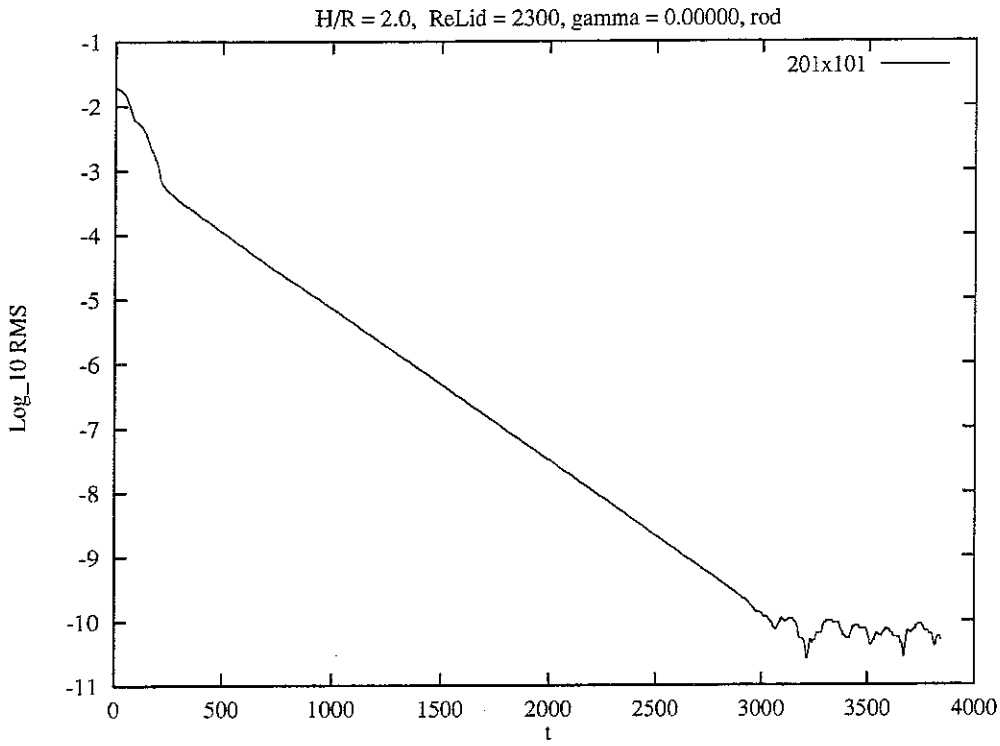

Figure 2.12: RMS level as a function of time for the parameters $\mathrm{Re}_{lid} = 2300$, $\gamma = 0.000$.

2.7.5 Prediction of the behavior of transients

Consider a transient consisting of an oscillation behaving as

$$u(t) = A(t)\sin(\omega t) + B \tag{2.27}$$

where

$$A(t) = \alpha e^{-kt} + \beta. \tag{2.28}$$

From this it can be concluded that

$$-k = \frac{1}{\Delta t}\ln\frac{A(t+2\Delta t) - A(t+\Delta t)}{A(t+\Delta t) - A(t)}, \tag{2.29}$$

$$\alpha = (A(t) - \beta)e^{kt} \tag{2.30}$$

and

$$\beta = \frac{-e^{-k\Delta t}A(t) + A(t+\Delta t)}{1 - e^{-k\Delta t}},\ k \neq 0. \tag{2.31}$$

As the amplitude A(t) is proportional to the RMS level for a harmonic signal with a slowly varying amplitude, the RMS level of the limiting state of the flow can be predicted by using the equations (2.29) and (2.31). This method was implemented in the computer program transi. It was used to decide if the limiting flow was steady or unsteady for parameter

values near critical points where only part of the necessary data for very long transients was available.

As a practical criterion of steadiness an RMS level of 10^{-7} was chosen. For limiting RMS levels below this value the flow was characterized as being steady and otherwise unsteady. For RMS levels near the value of the criterion, the simulations were continued where practical in order to improve the data and reduce the risk of wrong predictions.

2.7.6 Frequencies present in the unsteady flow

The frequencies found by application of the procedure described in 2.7.3 were plotted as a function of $\gamma \geq 0$ for $\mathrm{Re}_{lid} = 2500$ in Fig. 2.13. For $0 \leq \gamma \leq 0.00525$ the flow is steady.

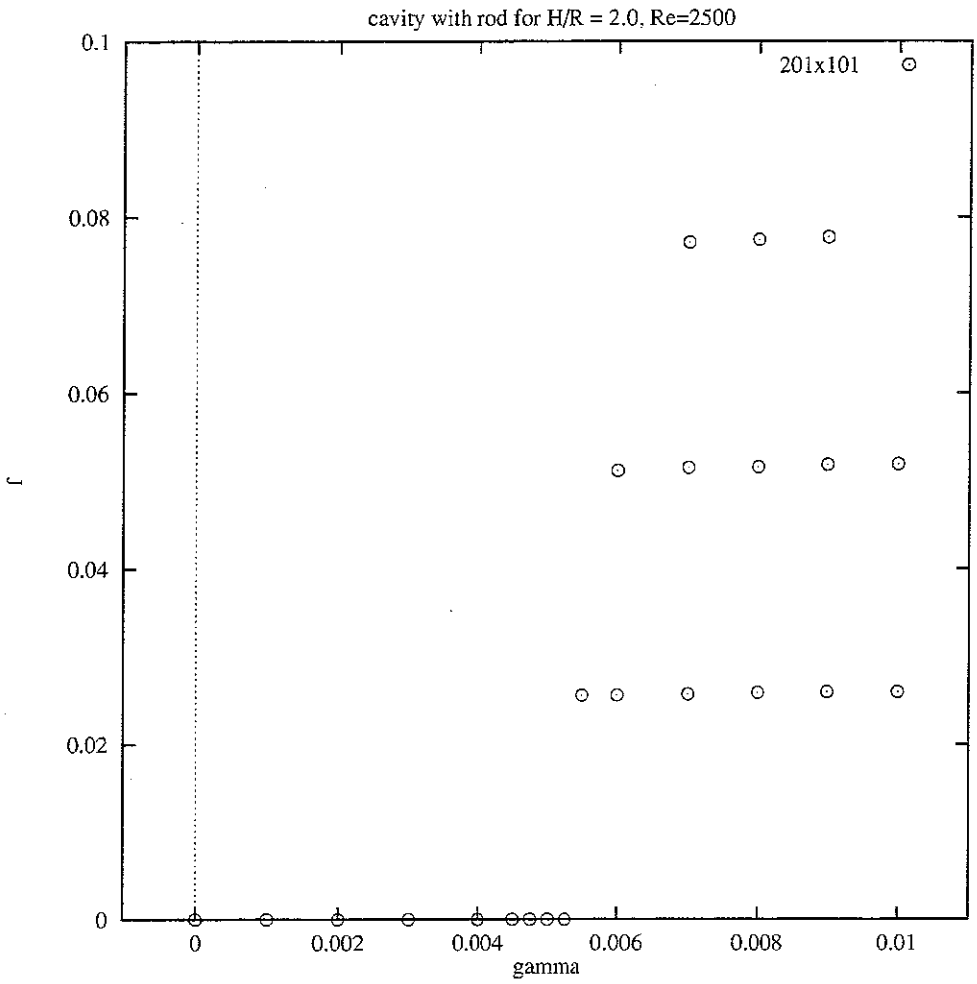

Figure 2.13: Frequencies in the unsteady flow as a function of γ for $\mathrm{Re}_{lid} = 2500$.

Between $\gamma = 0.00525$ and $\gamma = 0.00550$ a transition to unsteady flow takes place. At $\gamma = 0.00550$ the unsteady flow oscillates with the frequency $f_1 = 0.02558$. The transition from a steady flow to an unsteady flow consisting of a single harmonic oscillation indicates a Hopf

bifurcation. At $\gamma = 0.00600$ the first harmonic has appeared with a frequency of $f_2 = 0.05117$. At $\gamma = 0.00700$ a second harmonic has appeared with a frequency of $f_3 = 0.07713$.

For increasing γ the three frequencies are slightly increasing. Without the parabolic interpolation described in 2.7.3 the plotted frequencies appear somewhat fluctuating as a function of γ so that the slight increase of the frequencies with increasing γ is not obvious to the unaided human eye.

In Fig. 2.14 the frequencies are plotted as a function of $\gamma \geq 0$ for $\mathrm{Re}_{lid} = 2550$. For

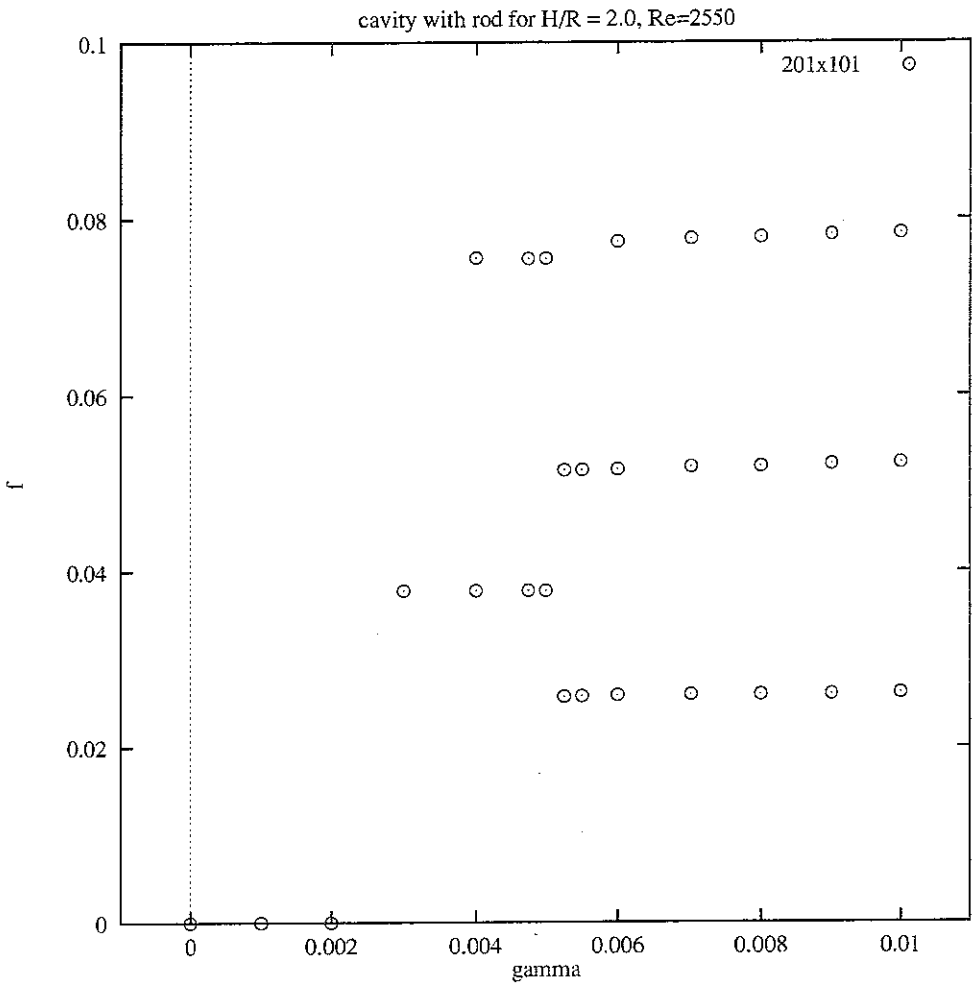

Figure 2.14: Frequencies in the unsteady flow as a function of γ for $\mathrm{Re}_{lid} = 2550$.

$\gamma \leq 0.00200$ the flow is steady. Between $\gamma = 0.00200$ and $\gamma = 0.00300$ a transition to unsteady flow takes place. The basic frequency observed at $\gamma = 0.00300$ is $f_1 = 0.03778$. At $\gamma = 0.00400$ the first harmonic has appeared with a frequency of $f_2 = 0.07564$. At $\gamma = 0.00550$ a second basic frequency, $f_3 = 0.02578$, has appeared, and the first basic frequency, f_1, has died out. This phenomenon could caused by fold bifurcations occurring in the periodic flow. However, simulations of hysteresis were not pursued in order to prove this.

Another explanation could be a torus bifurcation followed by an inverse torus bifurcation within a narrow parameter range. But no proof of this has been obtained. At $\gamma = 0.00600$ the second harmonic $2f_3$ has appeared. A slight increase of the frequencies is observed for increasing γ.

Fig. 2.15 depicts the frequencies found for $\mathrm{Re}_{lid} = 2600$. For $-0.00500 \leq \gamma \leq -0.00200$

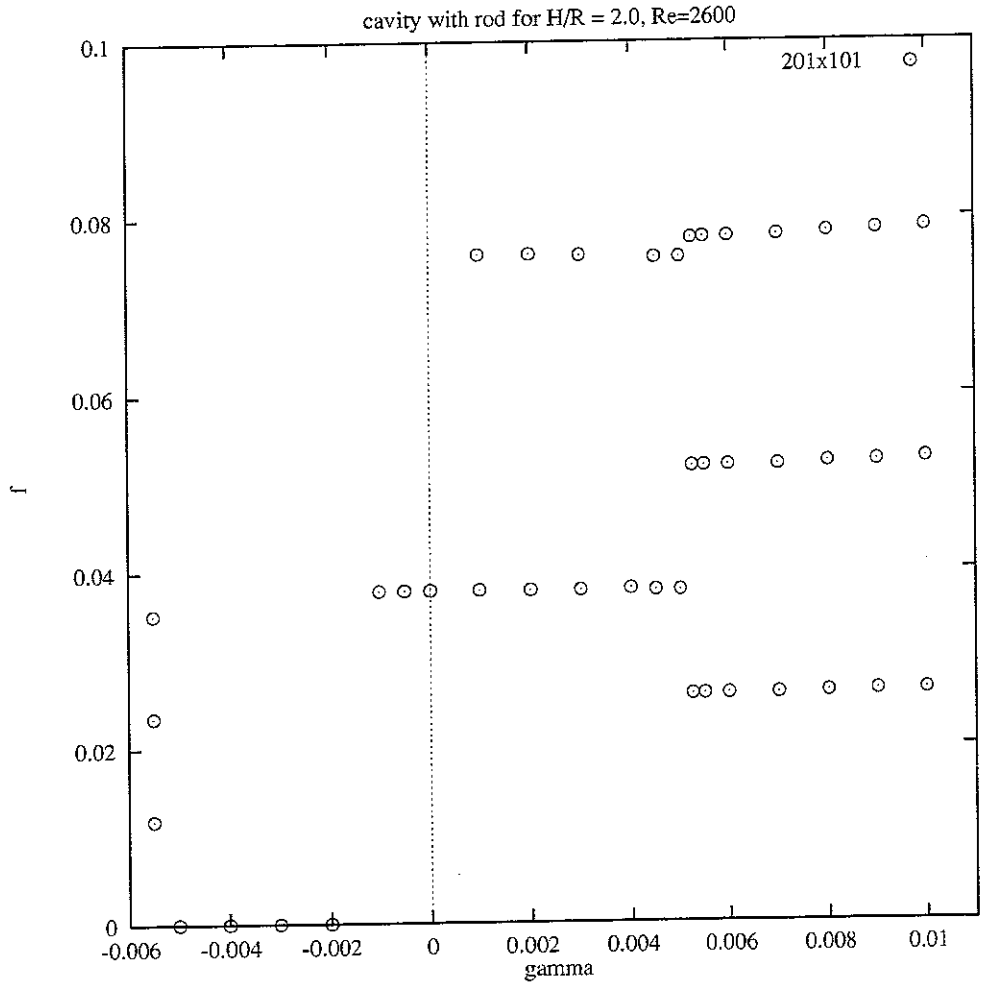

Figure 2.15: Frequencies in the unsteady flow as a function of γ for $\mathrm{Re}_{lid} = 2600$.

the flow is steady. Between $\gamma = -0.00200$ and $\gamma = -0.00100$ a transition takes place to an oscillating flow with the frequency $f_1 = 0.03781$. At $\gamma = 0.00100$ the first harmonic has appeared. A sudden change to a second basic frequency, $f_2 = 0.02592$ takes place between $\gamma = 0.00500$ and $\gamma = 0.00525$. At $\gamma = 0.00525$ the second basic frequency and its harmonics dominate the flow and the first basic frequency and its harmonics have disappeared entirely.

At $\gamma = -0.00550$ only the frequency $f_4 = 0.01179$ and its harmonics $2f_4$ and $3f_4$ appear. Although it has not been proved, it is suspected that a transition to chaos through period doublings take place within a narrow range of γ above $\gamma = -0.00600$.

2.7.7 Hopf bifurcations for constant γ

Near the critical point a Hopf bifurcation exhibits a linear relationship between the squared amplitude and the controlling parameter. From this the critical point can be estimated. As the RMS level is proportional to the amplitude for an oscillating flow with a constant amplitude, the squared RMS level should depend linearly on the Reynolds number near a Hopf bifurcation.

For $\gamma = 0.000$ a Hopf bifurcation occurs at $\mathrm{Re}_{lid} = 2590$. This can be seen by plotting the squared RMS level of the oscillating flow as a function of the Reynolds number as shown in Fig. 2.16. For the periodic flow, the data point nearest to the estimated critical point was

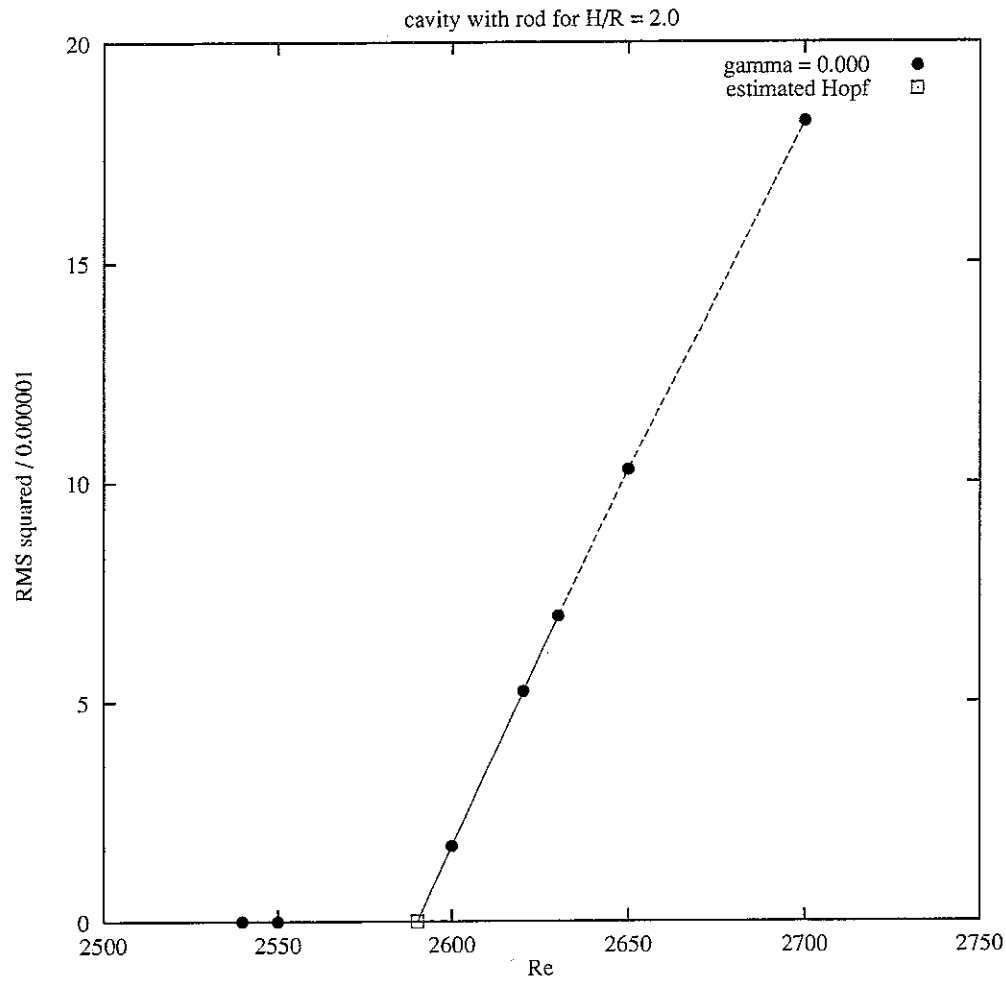

Figure 2.16: Squared RMS level as a function of the Reynolds number near the Hopf bifurcation for $\gamma = 0.000$.

found via the computer program transi as explained in 2.7.5.

As shown in Fig. 2.17, for $\gamma = -0.004$ a Hopf bifurcation occurs at $\mathrm{Re}_{lid} = 2630$. Hence, the interesting result has been obtained that the transition to unsteady flow can be sup-

pressed, by counter-rotation of the rod, so that it occurs at a higher Reynolds number than when the rod is fixed.

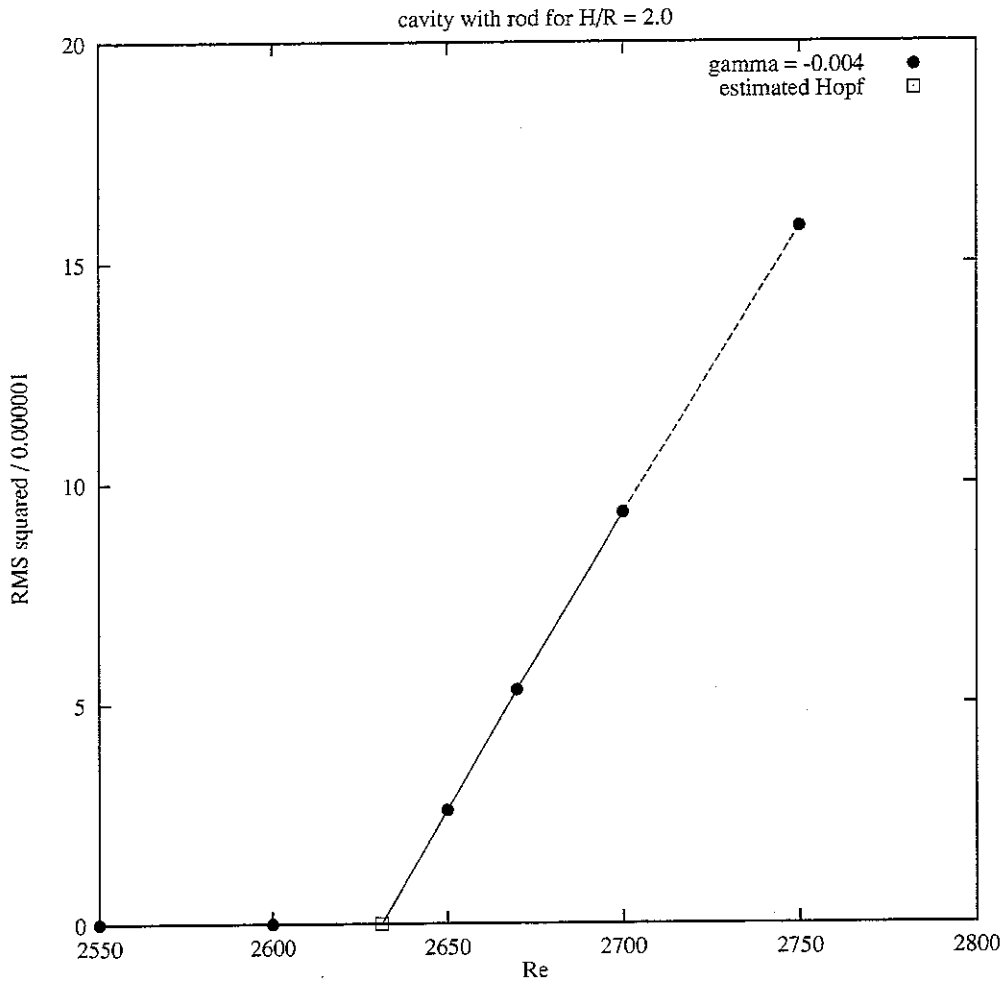

Figure 2.17: Squared RMS level as a function of the Reynolds number near the Hopf bifurcation for $\gamma = -0.004$.

It should be noted that it is possible to validate the estimated critical points by investigating the behavior of other components of the flow field. By plotting the RMS level of other velocity components or the vorticity, several estimates can be obtained for the same critical point. This was performed by Sørensen and Christensen [28] for the cavity without a rod.

2.7.8 Hopf bifurcation for constant Reynolds number

In Fig. 2.18 the squared RMS level of the oscillating flow has been plotted as a function of γ for $\mathrm{Re}_{lid} = 2550$. The linear relationship between the squared RMS level and the controlling parameter, γ, near the estimated critical point indicates that a Hopf bifurcation occurs at $\gamma = 0.00366$. Thus, the transition to unsteady flow can be enhanced by co-rotation of the

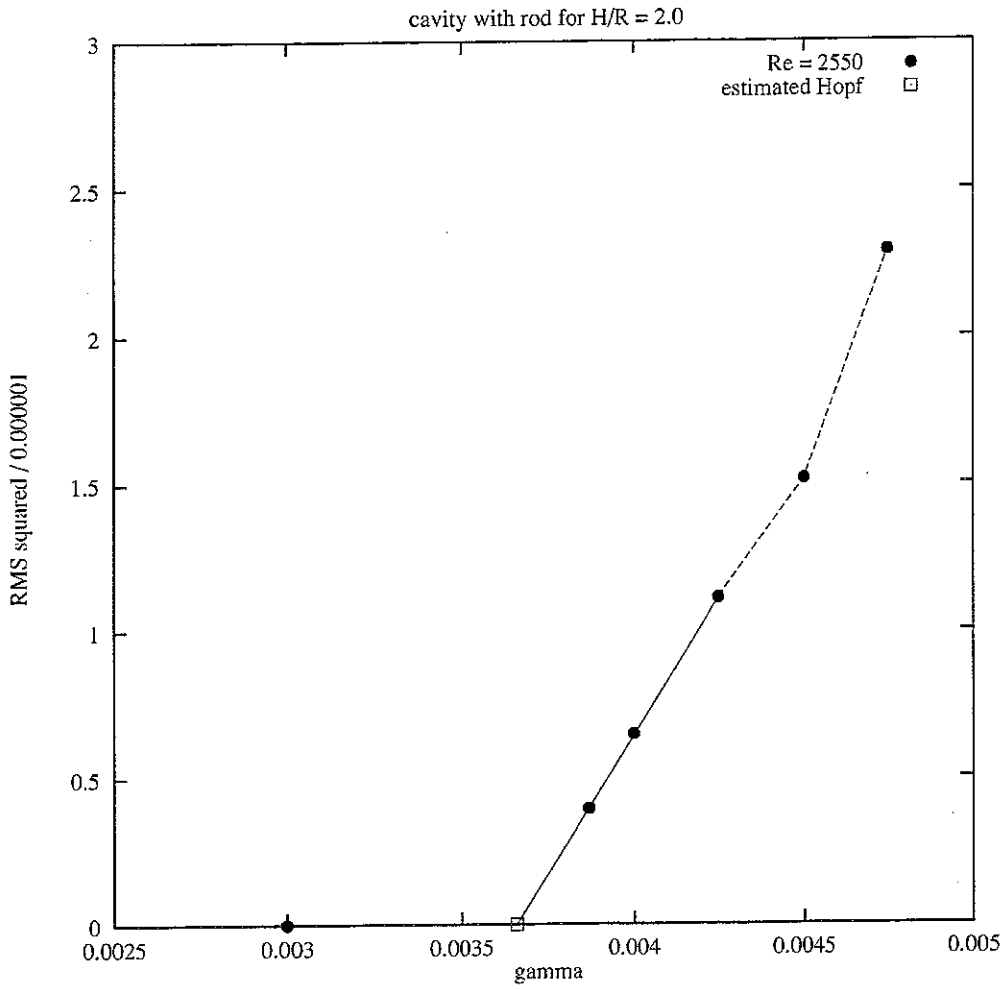

Figure 2.18: Squared RMS level as a function of γ near the Hopf bifurcation for $\mathrm{Re}_{lid} = 2550$.

rod, so that it occurs at a lower Reynolds number than when the rod is fixed.

In Fig. 2.19 the squared RMS level of the oscillating flow has been plotted as a function of γ for $\mathrm{Re}_{lid} = 2600$. The linear relationship between the squared RMS level and the controlling parameter, γ, near the estimated critical point indicates that a Hopf bifurcation occurs $\gamma = -0.00103$. This confirms the result, established in 2.7.7, that the transition to unsteady flow can be suppressed by counter-rotation of the rod so that it occurs at a higher Reynolds number than when the rod is fixed.

For $\gamma = -0.002$ the flow approaches the limiting flow very slowly. Therefore, the simulation of the transient for $\gamma = -0.002$ was not pursued to decide if the limiting flow is steady, as this would be rather expensive. However, by viewing Fig. 2.19 it can seen that the limiting flow is steady for $\gamma = -0.002$.

In Figs. 2.18 and 2.19 it should be emphasized, for the periodic flow, that the three data points nearest to the estimated critical point do not lie as close to a straight line as for the

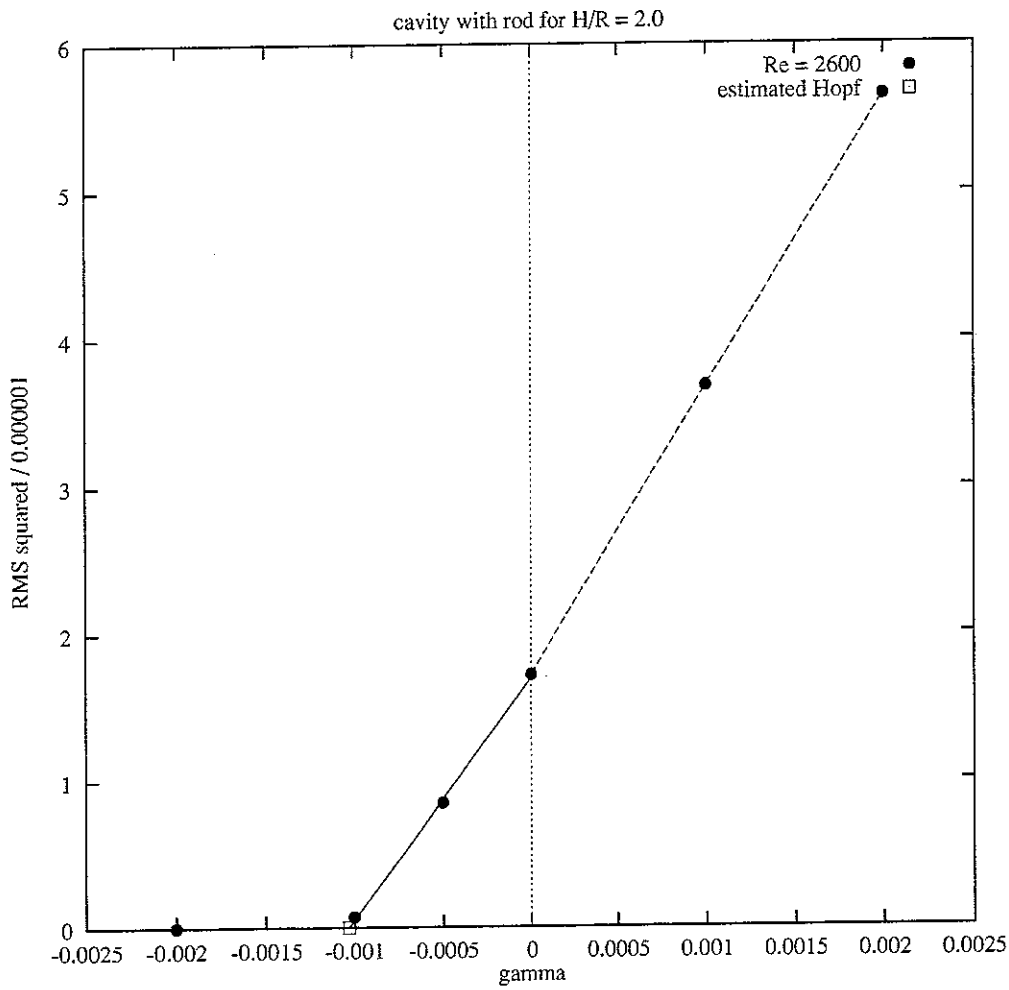

Figure 2.19: Squared RMS level as a function of γ near the Hopf bifurcation for $\mathrm{Re}_{lid} = 2600$.

results presented for the constant γ in 2.7.7. Thus, it would have been desirable to have more data points closer to the estimated critical points for the case of the constant Reynolds number.

2.7.9 Suppression of vortex breakdown in unsteady flow

The simulated periodic flow was visualized numerically by injection of tracing particles. The simulation was carried out in three steps. First, the periodic flow was allowed to approach the limiting state. Second, after the injection of tracing particles near the rod close to the fixed bottom, the simulation was carried on for approximately 40 periods. In this way, the particles were distributed for visualization of structures appearing in the flow. Third, starting at the time $t = 0$, the visualized flow was recorded at regular time intervals.

For $\mathrm{Re}_{lid} = 2800$ and $\gamma = 0.000$, a breakdown bubble in the periodic flow was visualized by injection of tracing particles. The results for $t = 0.0$, $t = 8.0$, $t = 16.0$ and $t = 24.0$ are

shown in Fig. 2.20. Only the part of the flow containing the vortex core has been plotted for each time instant. The breakdown bubble in the vortex core appears near the fixed bottom. The visualized structure spreads out in a T-shaped form near the rotating lid. The period of the flow was found to be 26.24 via a Fast Fourier Transform. Thus, nearly one period passes between the first and the last image. The breakdown bubble appears to be moving in the axial direction. From $t = 0.0$ to $t = 8.0$ the bubble moves towards the rotating lid. Furthermore, the outer tip of the bubble travels inwards along the upper surface of the bubble. Also, the inner spike attached to the upper surface of the bubble is elongated so that it attains an appearance like the thin spikes which are traveling along the rod towards the rotating lid. A new outer tip has formed at the bubble at $t = 8.0$. At $t = 16.0$ the bubble has moved further in direction towards the rotating lid. The spikes appearing on the upper surface of the bubble continue to move inwards. At $t = 24.0$ the bubble has obtained a shape which is close to the shape for $t = 0.0$, and it has moved in direction of the fixed bottom.

The periodic flow for $\mathrm{Re}_{lid} = 2800$ and $\gamma = 0.004$ has been visualized in Fig. 2.21 at $t = 0.0$, $t = 8.0$, $t = 16.0$ and $t = 24.0$. The breakdown bubble that appeared for the fixed rod at $\gamma = 0.000$ in Fig. 2.20 is clearly suppressed by co-rotation of the rod at $\gamma = 0.004$. Only a small bubble protruding from the rod is visible at $t = 0.0$. At $t = 8.0$ the small bubble has moved along the rod towards the lid. Also, closer to the fixed bottom, a new thin structure has started to form on the surface of the rod. At $t = 16.0$, the bubble has been elongated so that it appears like the spikes moving along the rod towards the rotating lid. The thin structure on the surface of the rod has been formed into a small bubble and has moved in direction of the rotating lid. At $t = 24.0$ the small bubble has moved towards the fixed bottom. Furthermore, the thin spikes attached to the rod have moved in direction of the rotating lid. For all four images, a small ring is visible on each side of the rod in the zone near the rotating lid where the visualized structure spreads out in a T-shaped form. This indicates the presence of a small annular vortex oriented with its axis of symmetry parallel to the center axis of the cavity.

The periodic flow was visualized for $\gamma = 0.000$, i.e. a fixed rod, and $\gamma = 0.004$, i.e. a co-rotating rod, at the Reynolds numbers 2600, 2700, 2800, 2900, 3000 and 3100. For all the Reynolds numbers, the breakdown bubbles appearing in the case of the fixed rod were suppressed in the case of the co-rotating rod.

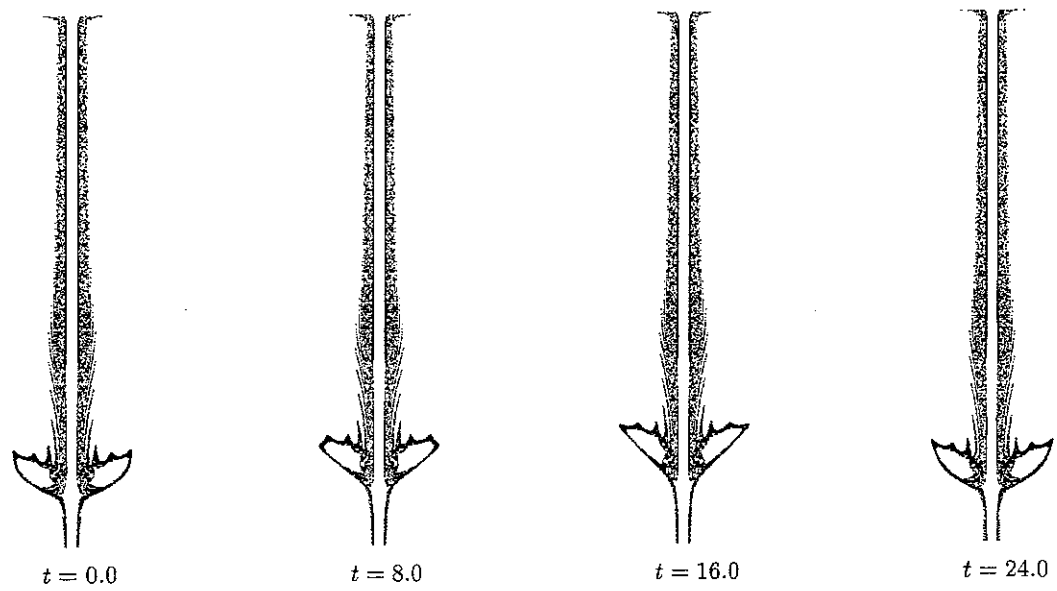

Figure 2.20: Simulated visualization of an unsteady flow at $\mathrm{Re}_{lid} = 2800$ for $\gamma = 0.000$.

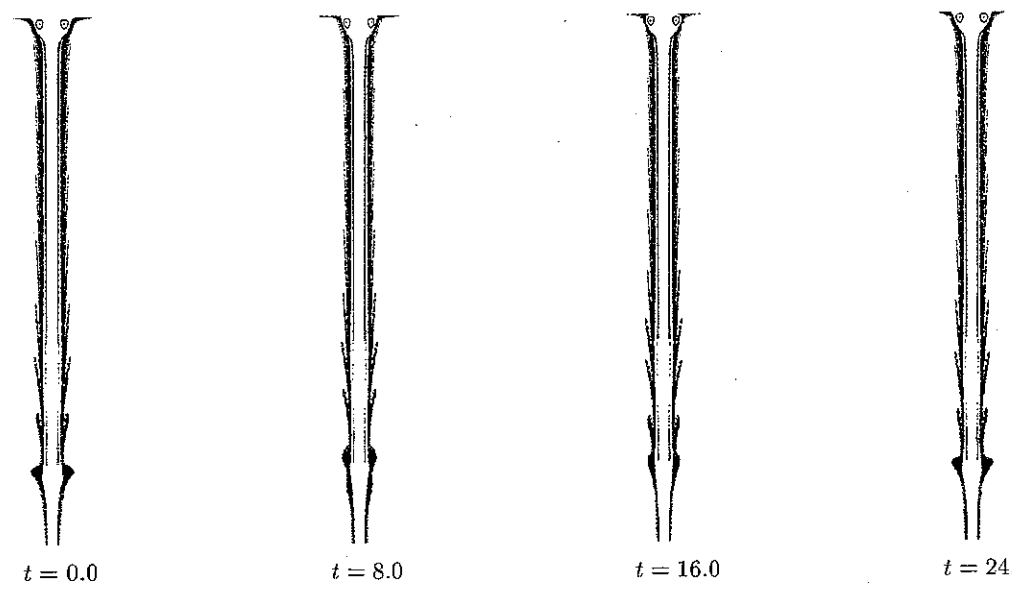

Figure 2.21: Simulated visualization of an unsteady flow at $\mathrm{Re}_{lid} = 2800$ for $\gamma = 0.004$.

2.8 Conclusion

The flow in a lid driven cavity with a rotating rod has been studied by numerical simulations utilizing an axisymmetric Navier-Stokes solver. The results of the simulations show that the breakdown bubbles of the steady flow as well as the unsteady flow can be controlled by the rotation of the rod.

In order to characterize the flow for a given set of parameters, the numerical simulations were carried out for a long time interval until a limiting state was obtained. Tools were developed to obtain a quantitative measure of the transient behavior of the flow field in the cavity. Transition of the flow was studied and the frequencies appearing in the time varying flow field were determined by applying a Fast Fourier Transform (FFT) and locating the peaks in the calculated FFT amplitudes. It has been demonstrated that the transition to unsteady flow can be suppressed, by counter-rotation of the rod, so that it occurs at a higher Reynolds number than when the rod is fixed. Also, the transition to unsteady flow can be enhanced by co-rotation of the rod, so that it occurs at a lower Reynolds number than when the rod is fixed. The data resulting from the investigation are suitable for the construction of low-dimensional models based on decomposition techniques with the purpose of analyzing bifurcations occurring in the flow.

Part II

Low-dimensional modeling

Chapter 3

Decomposition techniques

3.1 POD

Proper Orthogonal Decomposition (POD) is a transformation that produces a set of basis vectors which span the input data in such a way that the fraction of energy represented by any given number of basis vectors is the largest possible. The basis vectors are called modes. POD was first introduced to the fluid mechanics society in 1967 by Lumley [19] who suggested that eddies in turbulent flows can be interpreted as POD modes. This point of view can be somewhat misleading when taken too literally. On the other hand, it is commonly accepted to think of Fourier modes as a sort of eddies with sizes corresponding to the wavenumber. Within the context of linear functional theory, POD is simply a Fourier transformation with a different type of basis functions than the harmonic functions. Hence, one may view the POD modes as a sort of flow structures similar to the eddies.

Since its introduction in fluid mechanics, POD has been used for analyzing experimental data by Delville [13] and others, and for studying the results of numerical computations as done by Manhart [21]. A review has been written by Berkooz *et al.* [4] about POD in the analysis of turbulent flows.

POD is also known as Singular Value Decomposition (SVD), Karhunen-Loéve Transformation (KLT) and Empirical Orthogonal Functions (EOF). It is widely known as a tool of statistical pattern recognition. See for instance Fukanaga [16]. The basic idea of the transformation is to sample data, estimate the auto-covariance, solve the corresponding eigenvalue problem and then use the solution to construct an orthogonal basis. There are several ways to present the transformation. However, in the context of discretized partial differential equations, it is useful to consider the discrete transformation.

In the remaining part of this section a summary of POD is given. The following two sections contain the basic derivations of POD and a proof of the energy optimality.

The sampled data is arranged in vectors, $\mathbf{x}_1, \mathbf{x}_2, \ldots, \mathbf{x}_n$, each containing a snapshot of the flow field at a given time. This is the first step of what is called the snapshot POD. One may also sample the time evolution of flow field variables at different locations, and arrange the data into a vector for each location, which is the approach used in the classical POD. However, when considering sampling of data with 10^5 or more components, the classical POD yields an auto-covariance matrix with a prohibitively high rank. Thus, the snapshot POD is preferred.

It is customary to subtract the mean vector from the snapshot vectors by

$$\mathbf{u}_k = \mathbf{x}_k - \frac{1}{n}\sum_{i=1}^{n}\mathbf{x}_i \tag{3.1}$$

This operation turns out to be crucial for constructing POD-Galerkin models with more than one free parameter. Subtracting the mean vector decreases the number of dimensions by one, i.e. span($\mathbf{u}_1, \ldots, \mathbf{u}_n$) has $n-1$ dimensions.

The auto-covariance matrix is calculated by

$$R_{ik} = \mathbf{u}_i \cdot \mathbf{u}_k \tag{3.2}$$

Now, solving the eigenvalue problem

$$\mathbf{R}\mathbf{g}_k = \mathbf{g}_k\lambda_k, \; k = 1, \ldots, n-1 \tag{3.3}$$

and arranging the eigenvalues in descending order,

$$\lambda_1 \geq \lambda_2 \geq \cdots \geq \lambda_{n-1} > 0, \tag{3.4}$$

one obtains an orthonormal basis

$$\boldsymbol{\phi}_k = \frac{\sum_{i=1}^{n} g_{ik}\mathbf{u}_i}{\left\| \sum_{i=1}^{n} g_{ik}\mathbf{u}_i \right\|} \tag{3.5}$$

which solves the problem

$$\lambda_k = \max_{\|\boldsymbol{\phi}_k\| = 1} \left\{ \sum_{i=1}^{n} (\boldsymbol{\phi}_k \cdot \mathbf{u}_i)^2 \right\} \tag{3.6}$$

where

$$\boldsymbol{\phi}_k \cdot \boldsymbol{\phi}_l = 0 \text{ for } l = 1, 2, \ldots, k-1. \tag{3.7}$$

Therefore, the POD is an energy-optimal transformation in the sense that it produces a set of basis vectors which span the input data in such a way that the fraction of energy represented by any given number of basis vectors is the largest possible. This fact is exploited when

truncating the set of POD modes by keeping the first m modes for $m < n-1$ and ignoring the remaining modes. Thus, only the eigenvalues

$$\lambda_1 \geq \lambda_2 \geq \cdots \geq \lambda_m > 0, \tag{3.8}$$

and the modes

$$\phi_1,\ \phi_2,\ \ldots,\ \phi_m \tag{3.9}$$

are retained when truncating a POD for $m < n-1$.

3.1.1 Basic derivations of POD

When using matrix notation, the details of POD can be explained conveniently by linear algebra. Introducing the matrix

$$\mathbf{U} = [\mathbf{u}_1 \quad \cdots \quad \mathbf{u}_n], \tag{3.10}$$

the auto-covariance matrix is given by

$$\mathbf{R} = \mathbf{U}^{\mathrm{T}}\mathbf{U} \tag{3.11}$$

Defining the eigenvalue matrix,

$$\mathbf{\Lambda} = \begin{pmatrix} \lambda_1 & & \mathbf{0} \\ & \ddots & \\ \mathbf{0} & & \lambda_{n-1} \end{pmatrix}, \tag{3.12}$$

and the matrix of eigenvectors,

$$\mathbf{G} = [\mathbf{g}_1 \quad \cdots \quad \mathbf{g}_{n-1}], \tag{3.13}$$

the eigenvalue problem can be represented by

$$\mathbf{RG} = \mathbf{G\Lambda} \tag{3.14}$$

Since R is symmetrical and positive definite the eigenvalues $\lambda_1,\ \ldots,\ \lambda_{n-1}$ are *real and positive*. Furthermore, for $\|\mathbf{g}_i\| = 1$, $i \in \{1,\ \ldots,\ n-1\}$, the eigenvectors are orthonormal, i.e.

$$\mathbf{G}^{\mathrm{T}}\mathbf{G} = \mathbf{E}. \tag{3.15}$$

Defining the matrix product

$$\mathbf{B} = \mathbf{UG} \tag{3.16}$$

the matrix $\mathbf{U}$ can be reconstructed from

$$\mathbf{U} = \mathbf{BG}^{\mathrm{T}}. \tag{3.17}$$

Note from (3.14) that

$$\mathbf{\Lambda} = \mathbf{G}^{\mathrm{T}}\mathbf{R}\mathbf{G} = \mathbf{G}^{\mathrm{T}}\mathbf{G}\mathbf{B}^{\mathrm{T}}\mathbf{B}\mathbf{G}^{\mathrm{T}}\mathbf{G} = \mathbf{B}^{\mathrm{T}}\mathbf{B}. \tag{3.18}$$

Using the notation

$$\mathbf{\Lambda}^{\frac{1}{2}} = \begin{pmatrix} \lambda_1^{\frac{1}{2}} & & \mathbf{0} \\ & \ddots & \\ \mathbf{0} & & \lambda_{n-1}^{\frac{1}{2}} \end{pmatrix}, \tag{3.19}$$

and, for $\mathbf{\Lambda}^{-\frac{1}{2}} = (\mathbf{\Lambda}^{\frac{1}{2}})^{-1}$, defining

$$\mathbf{\Phi} = \mathbf{B}\mathbf{\Lambda}^{-\frac{1}{2}} \tag{3.20}$$

an orthonormal basis is obtained in the columns of $\mathbf{\Phi}$ as a consequence of (3.18) because

$$\mathbf{\Phi}^{\mathrm{T}}\mathbf{\Phi} = \mathbf{\Lambda}^{-\frac{1}{2}}\mathbf{B}^{\mathrm{T}}\mathbf{B}\mathbf{\Lambda}^{-\frac{1}{2}} = \mathbf{\Lambda}^{-\frac{1}{2}}\mathbf{\Lambda}\mathbf{\Lambda}^{-\frac{1}{2}} = \mathbf{E}. \tag{3.21}$$

Since

$$\mathbf{B} = \mathbf{\Phi}\mathbf{\Lambda}^{\frac{1}{2}} \tag{3.22}$$

the matrix $\mathbf{U}$ can be reconstructed by a linear combination of the orthonormal basis vectors

$$\mathbf{U} = \mathbf{B}\mathbf{G}^{\mathrm{T}} = \mathbf{\Phi}\mathbf{\Lambda}^{\frac{1}{2}}\mathbf{G}^{\mathrm{T}}. \tag{3.23}$$

The coefficients

$$\mathbf{A} = \mathbf{\Lambda}^{\frac{1}{2}}\mathbf{G}^{\mathrm{T}} \tag{3.24}$$

appearing in the linear combination will be called *amplitudes*. Thus,

$$\mathbf{U} = \mathbf{\Phi}\mathbf{A} \tag{3.25}$$

from which it follows that the amplitudes can also be found by

$$\mathbf{A} = \mathbf{\Phi}^{\mathrm{T}}\mathbf{U}. \tag{3.26}$$

Defining the mean vector

$$\mathbf{x}_0 = \frac{1}{n}\sum_{j=1}^{n}\mathbf{x}_j \tag{3.27}$$

the original snapshots can be reconstructed by

$$\mathbf{x}_j = \mathbf{x}_0 + \sum_{k=1}^{n-1}\phi_k a_{kj} \tag{3.28}$$

where a_{kj} are the elements of the matrix $\mathbf{A}$. Furthermore,

$$\mathbf{\Phi} = (\mathbf{U}\mathbf{G})\mathbf{\Lambda}^{-\frac{1}{2}} \tag{3.29}$$

of which a single column

$$\boldsymbol{\phi}_k = (\mathbf{U}\mathbf{g}_k)\lambda_k^{-\frac{1}{2}} \tag{3.30}$$

is a basis vector. Since $\|\boldsymbol{\phi}_k\| = 1$ the basis vector can be written as

$$\boldsymbol{\phi}_k = \frac{\mathbf{U}\mathbf{g}_k}{\|\mathbf{U}\mathbf{g}_k\|}. \tag{3.31}$$

This is simply another form of (3.5). Note that

$$\mathbf{A}\mathbf{A}^{\mathrm{T}} = \boldsymbol{\Lambda}^{\frac{1}{2}}\mathbf{G}^{\mathrm{T}}\mathbf{G}\boldsymbol{\Lambda}^{\frac{1}{2}} = \boldsymbol{\Lambda}. \tag{3.32}$$

3.1.2 Energy optimality of POD

Consider, for $\|\mathbf{h}_k\| = 1$, the vector $\mathbf{h}_k$ which can be written as a linear combination of orthonormal basis vectors,

$$\mathbf{h}_k = \boldsymbol{\Phi}\mathbf{s}_k. \tag{3.33}$$

The energy

$$\mu_k = (\mathbf{U}^{\mathrm{T}}\mathbf{h}_k)^{\mathrm{T}}(\mathbf{U}^{\mathrm{T}}\mathbf{h}_k) \tag{3.34}$$

can the be expressed as

$$\mu_k = (\mathbf{A}^{\mathrm{T}}\boldsymbol{\Phi}^{\mathrm{T}}\mathbf{h}_k)^{\mathrm{T}}(\mathbf{A}^{\mathrm{T}}\boldsymbol{\Phi}^{\mathrm{T}}\mathbf{h}_k) = (\mathbf{G}\boldsymbol{\Lambda}^{\frac{1}{2}}\boldsymbol{\Phi}^{\mathrm{T}}\boldsymbol{\Phi}\mathbf{s}_k)^{\mathrm{T}}(\mathbf{G}\boldsymbol{\Lambda}^{\frac{1}{2}}\boldsymbol{\Phi}^{\mathrm{T}}\boldsymbol{\Phi}\mathbf{s}_k) = \mathbf{s}_k^{\mathrm{T}}\boldsymbol{\Lambda}\mathbf{s}_k = \sum_{j=1}^{n-1}\lambda_j s_{jk}^2 \tag{3.35}$$

The energy can be maximized in the following manner. Since $\boldsymbol{\Phi}$ is an orthonormal basis and $\|\mathbf{h}_k\| = 1$ it follows that $\|\mathbf{s}_k\| = 1$. Thus, for a given value of k,

$$\mathbf{s}_{kk}^2 = 1 - \sum_{j\neq k} s_{jk}^2 \tag{3.36}$$

Hence,

$$(\mu_k - \lambda_k) = \sum_{j\neq k}\lambda_j s_{jk}^2 + \lambda_k(1 - \sum_{j\neq k} s_{jk}^2) - \lambda_k = \sum_{j\neq k}(\lambda_j - \lambda_k)s_{jk}^2 \tag{3.37}$$

Arranging $\boldsymbol{\Phi}$ so that $\lambda_1 \geq \lambda_2 \geq \cdots \geq \lambda_{n-1} > 0$ we may assume that $\lambda_1 = \cdots = \lambda_q > \lambda_{q+1}$ for some $q < n-1$. From (3.37) it is now seen that $(\mu_1 - \lambda_1)$ has maximum for $\mathbf{s}_{j1} = 0,\ j \neq 1,\ \ldots,\ q$, which yields

$$\mu_1 = \lambda_1. \tag{3.38}$$

Hence, μ_1 is maximized by choosing $\mathbf{h_1}$ from span$\{\boldsymbol{\phi}_1,\ \ldots,\ \boldsymbol{\phi}_q\}$. It is sufficient to choose

$$\mathbf{h}_1 = \boldsymbol{\phi}_1. \tag{3.39}$$

Similarly, for $\|\mathbf{h}_k\| = 1$ and the condition $\mathbf{h}_k^{\mathrm{T}}\boldsymbol{\phi}_j = 0,\ j = 1,\ \ldots,\ k-1$, the maximum of μ_k is obtained by

$$\mu_k = \lambda_k, \tag{3.40}$$

$$\mathbf{h}_k = \boldsymbol{\phi}_k. \tag{3.41}$$

This result can also be written

$$\lambda_k = \max_{\|\mathbf{h}_k\| = 1} \left\{ \sum_{i=1}^{n-1} (\mathbf{u}_i^{\mathrm{T}} \mathbf{h}_k)^2 \right\}, \ \mathbf{h}_k^{\mathrm{T}} \mathbf{h}_j = 0 \text{ for } j = 1, \ \ldots, \ k-1, \tag{3.42}$$

is satisfied by

$$\mathbf{h}_k = \boldsymbol{\phi}_k, \ k = 1, \ \ldots, \ n-1. \tag{3.43}$$

I.e. the POD is an energy optimal transformation.

3.1.3 Following components

Sometimes it is desirable to use only certain components of the snapshots for carrying out a POD. However, the remaining components can be transformed as well by using the method of *following components*. As before, the sampled data is arranged in vectors $\mathbf{x}_1, \ \ldots, \ \mathbf{x}_n$. But the vectors resulting from subtraction of the mean vector $\mathbf{x}_0$ are split into two parts,

$$\begin{bmatrix} \mathbf{u}_j \\ \mathbf{v}_j \end{bmatrix} = \mathbf{x}_j - \mathbf{x}_0 \tag{3.44}$$

The vectors $\mathbf{v}_j$ are called the vectors of the following components. Introducing the matrices

$$\mathbf{U} = [\mathbf{u}_1 \quad \cdots \quad \mathbf{u}_n], \quad \mathbf{V} = [\mathbf{v}_1 \quad \cdots \quad \mathbf{v}_n], \tag{3.45}$$

the auto-covariance matrix is defined as $\mathbf{R} = \mathbf{U}^{\mathrm{T}}\mathbf{U}$ and the POD is performed as usual. From the results we find

$$\mathbf{U} = \boldsymbol{\Phi}\mathbf{A} \tag{3.46}$$

and

$$\mathbf{A} = \boldsymbol{\Lambda}^{\frac{1}{2}} \mathbf{G}^{\mathrm{T}} \tag{3.47}$$

In order to transform the following components, define $\boldsymbol{\Psi}$ by

$$\mathbf{V} = \boldsymbol{\Psi}\mathbf{A}. \tag{3.48}$$

Since

$$\mathbf{V} = \boldsymbol{\Psi}\boldsymbol{\Lambda}^{\frac{1}{2}}\mathbf{G}^{\mathrm{T}}. \tag{3.49}$$

the part of the basis vectors containing the following components can now be obtained by

$$\boldsymbol{\Psi} = \mathbf{V}\mathbf{G}\boldsymbol{\Lambda}^{-\frac{1}{2}} \tag{3.50}$$

Hence, the original snapshots can be reconstructed by

$$\mathbf{x}_j = \mathbf{x}_0 + \sum_{k=1}^{n-1} \begin{bmatrix} \boldsymbol{\phi}_k \\ \boldsymbol{\psi}_k \end{bmatrix} a_{kj} \tag{3.51}$$

3.2 SPOD

Sequential Proper Orthogonal Decomposition (SPOD) is a technique developed by the author for calculating orthonormal bases suitable for low-dimensional models based on Galerkin projection of the governing equations. SPOD is capable of transforming data organized in different sets separately while still producing orthogonal modes. This feature is desirable because the POD modes with the largest eigenvalues represent data corresponding to large energy better than data corresponding to small energy. Thus, dynamically important data might not be represented unless it is either transformed separately or weighted in some fashion.

SPOD utilizes the construction of the orthogonal space to a predefined space which is used in the p-POD introduced by E. A. Christensen *et al.* [11]. In contrast to the p-POD, where all the preselected states are transformed together by a single POD, the SPOD allows the preselected states to be transformed separately in different sets. Furthermore, SPOD does not require the selection of any reference points as does the p-POD, except the mean vector of all the snapshots.

3.2.1 Calculating the SPOD

Consider the snapshots $\mathbf{x}_1, \ldots, \mathbf{x}_n$. In order to perform the SPOD, the mean vector

$$\mathbf{x}_0 = \frac{1}{n}\sum_{j=1}^{n}\mathbf{x}_j \tag{3.52}$$

is subtracted from the snapshots yielding

$$\mathbf{u}_j = \mathbf{x}_j - \mathbf{x}_0,\ j \in \{1, \ldots, n\}. \tag{3.53}$$

The resulting vectors are placed into a number, p, of separate sets, called *blocks*, each of which can be represented by a matrix $\mathbf{U}_i,\ i \in \{1, \ldots, p\}$. Furthermore, define

$$\mathbf{U} = [\mathbf{U}_1 \quad \mathbf{U}_2 \quad \cdots \quad \mathbf{U}_p]. \tag{3.54}$$

Then, a POD is performed on $\mathbf{U}_1$ yielding

$$\mathbf{U}_1 = \mathbf{\Phi}_1\mathbf{\Lambda}_1^{\frac{1}{2}}\mathbf{G}_1^{\mathrm{T}} = \mathbf{\Phi}_1\mathbf{A}_1. \tag{3.55}$$

The essential idea of the SPOD is to perform a POD of each block in the space which is orthogonal to the previous blocks. This is carried out in the following way. From each data vector of the current block its projection on the basis vectors of the previous blocks is subtracted before calculating the auto-covariance matrix of the POD. Hence,

$$\mathbf{U}_{i+1} - (\mathbf{\Phi}_1\mathbf{\Phi}_1^{\mathrm{T}} + \cdots + \mathbf{\Phi}_i\mathbf{\Phi}_i^{\mathrm{T}})\mathbf{U}_{i+1} = \mathbf{\Phi}_{i+1}\mathbf{\Lambda}_{i+1}^{\frac{1}{2}}\mathbf{G}_{i+1}^{\mathrm{T}} = \mathbf{\Phi}_{i+1}\mathbf{A}_{i+1}. \tag{3.56}$$

Defining the block diagonal matrix

$$\mathbf{A} = \begin{bmatrix} \mathbf{A}_1 & & \mathbf{0} \\ & \ddots & \\ \mathbf{0} & & \mathbf{A}_p \end{bmatrix} \tag{3.57}$$

and collecting the matrices containing the basis vectors

$$\mathbf{\Phi} = [\mathbf{\Phi}_1 \quad \cdots \quad \mathbf{\Phi}_p] \tag{3.58}$$

the following is obtained

$$\left[\mathbf{U}_1 \quad \mathbf{U}_2 - \mathbf{\Phi}_1\mathbf{\Phi}_1^{\mathrm{T}}\mathbf{U}_2 \quad \cdots \quad \mathbf{U}_p - (\mathbf{\Phi}_1\mathbf{\Phi}_1^{\mathrm{T}} + \cdots + \mathbf{\Phi}_{p-1}\mathbf{\Phi}_{p-1}^{\mathrm{T}})\mathbf{U}_p\right] = \mathbf{\Phi}\mathbf{A}. \tag{3.59}$$

Now, define the matrix of SPOD amplitudes

$$\mathbf{C} = [\mathbf{C}_1 \quad \cdots \quad \mathbf{C}_p] \tag{3.60}$$

so that

$$\mathbf{U} = \mathbf{\Phi}\mathbf{C} \tag{3.61}$$

Since

$$\mathbf{U} = \mathbf{\Phi}\mathbf{A} + \left[\mathbf{0} \quad \mathbf{\Phi}_1\mathbf{\Phi}_1^{\mathrm{T}}\mathbf{U}_2 \quad \cdots \quad (\mathbf{\Phi}_1\mathbf{\Phi}_1^{\mathrm{T}} + \cdots + \mathbf{\Phi}_{p-1}\mathbf{\Phi}_{p-1}^{\mathrm{T}})\mathbf{U}_p\right] \tag{3.62}$$

the following is obtained

$$\mathbf{C}_1 = \begin{bmatrix} \mathbf{A}_1 \\ \mathbf{0} \\ \vdots \\ \mathbf{0} \end{bmatrix}, \quad \mathbf{C}_i = \begin{bmatrix} \mathbf{\Phi}_1^{\mathrm{T}}\mathbf{U}_i \\ \vdots \\ \mathbf{\Phi}_{i-1}^{\mathrm{T}}\mathbf{U}_i \\ \mathbf{A}_i \\ \mathbf{0} \\ \vdots \\ \mathbf{0} \end{bmatrix}, \quad i \in \{2, \ldots, p\} \tag{3.63}$$

Hence, the amplitudes of the SPOD can be represented by a block diagonal matrix,

$$\mathbf{C} = \begin{bmatrix} \mathbf{A}_1 & \mathbf{\Phi}_1^{\mathrm{T}}\mathbf{U}_2 & \mathbf{\Phi}_1^{\mathrm{T}}\mathbf{U}_3 & \cdots & \mathbf{\Phi}_1^{\mathrm{T}}\mathbf{U}_p \\ \mathbf{0} & \mathbf{A}_2 & \mathbf{\Phi}_2^{\mathrm{T}}\mathbf{U}_3 & \cdots & \mathbf{\Phi}_2^{\mathrm{T}}\mathbf{U}_p \\ \mathbf{0} & \mathbf{0} & \mathbf{A}_3 & \ddots & \vdots \\ \vdots & \vdots & \ddots & \ddots & \mathbf{\Phi}_{p-1}^{\mathrm{T}}\mathbf{U}_p \\ \mathbf{0} & \mathbf{0} & \cdots & \mathbf{0} & \mathbf{A}_p \end{bmatrix} \tag{3.64}$$

It is seen that the diagonal blocks of $\mathbf{C}$ are identical to the amplitudes of the POD transformations performed in the SPOD. $\mathbf{C}$ contains only zeros below the diagonal blocks. Above

the diagonal blocks, $\mathbf{C}$ contains the inner products of $\mathbf{U}_i$ for $i \in \{1, \ldots, p\}$ and the basis vectors of the previous blocks, i.e. $\mathbf{\Phi}_1, \ldots, \mathbf{\Phi}_{i-1}$.

In the event that all the blocks $\mathbf{U}_1, \ldots, \mathbf{U}_p$ were orthogonal to each other, $\mathbf{C}$ would contain only the diagonal blocks, and (3.56) would reduce to

$$\mathbf{U}_{i+1} = \mathbf{\Phi}_{i+1}\mathbf{\Lambda}_{i+1}^{\frac{1}{2}}\mathbf{G}_{i+1}^{\mathrm{T}} = \mathbf{\Phi}_{i+1}\mathbf{A}_{i+1}. \tag{3.65}$$

meaning that the diagonal blocks of $\mathbf{C}$ would be the amplitudes of POD transformations performed independently for each block of snapshots after subtraction of the common mean vector $\mathbf{x}_0$. Since also the auto-covariance would be a block diagonal matrix, a single POD performed on $\mathbf{U}$ would yield the same amplitudes although in a different order.

When the blocks $\mathbf{U}_1, \ldots, \mathbf{U}_p$ are not orthogonal to each other, $\mathbf{C}$ is no longer zero above the diagonal blocks and the amplitudes of the SPOD are not identical to the amplitudes of the POD. Thus, the basis vectors of the SPOD are different from the basis vectors of the POD. From 3.1.2 it appears that the SPOD is not energy optimal. For simplicity, assume that $\lambda_1 > \cdots > \lambda_{n-1}$. Obtaining the maximum energies would then imply choosing vectors parallel to the basis vectors of a POD.

3.2.2 The truncated SPOD

As with the POD, truncating the SPOD is based on ignoring modes with low energy. However, in order to truncate the SPOD, a truncation must be performed for each block prior to finding the orthogonal space used for calculating the basis vectors of the next block. This is necessary because otherwise noise contained by the higher order modes of a block can be carried on to the subsequent blocks via construction of the orthogonal spaces. After truncation, the noise introduced in the modes from the last blocks cannot be balanced by a linear combination with the ignored higher order modes of the first blocks. This phenomenon causes reconstructed snapshots requiring modes from the last blocks to become noisy or non-smooth.

The requirement of truncating a block before calculating the next introduces the dilemma of knowing the energy of the modes in a block before having calculated it. How can the truncation be performed by ignoring the modes with the lowest energy? The solution is to calculate the SPOD in two stages. First, a regular POD of each block is calculated without the construction of any orthogonal spaces. This option is chosen because it is relatively fast, especially when the blocks are small compared to the total number of snapshots. The energy of the POD modes is used to estimate the number of modes of the blocks in the SPOD. Second, the truncated SPOD is calculated by, from each block, to retain exactly the number of modes decided in the first stage. After the truncation of each block, consider

the space which is orthogonal to the retained modes only. Within this orthogonal space the auto-covariance matrix, which is used in the transformation of the next block, is calculated.

One may argue that the second stage of the described algorithm for calculating the truncated SPOD yields modes with a different energy than the POD estimates of the energy resulting from the first stage. While this is perfectly true, it is considered an advantage that the algorithm is kept simple and efficient in order to harvest the benefits of dividing a large set of snapshots into more manageable blocks with fewer snapshots.

When truncating the set of modes of a block, $\mathbf{U}_i$, the modes, $\mathbf{\Phi}_{i+1}$, $\ldots$, $\mathbf{\Phi}_p$, of the successive blocks need not to be orthogonal to the ignored modes. Therefore, it may occur that

$$\mathbf{\Phi}_{i+1}^{\mathrm{T}}\mathbf{U}_i,\ \ldots,\ \mathbf{\Phi}_p^{\mathrm{T}}\mathbf{U}_i \neq 0. \tag{3.66}$$

A reconstruction better than

$$\mathbf{U}_i \approx \mathbf{\Phi}_i\mathbf{A}_i + (\mathbf{\Phi}_1\mathbf{\Phi}_1^{\mathrm{T}} + \cdots + \mathbf{\Phi}_{i-1}\mathbf{\Phi}_{i-1}^{\mathrm{T}})\mathbf{U}_i \tag{3.67}$$

can be obtained by including the contributions of the successive blocks, i.e.

$$\mathbf{U}_i \approx (\mathbf{\Phi}_1\mathbf{\Phi}_1^{\mathrm{T}} + \cdots + \mathbf{\Phi}_{i-1}\mathbf{\Phi}_{i-1}^{\mathrm{T}})\mathbf{U}_i + \mathbf{\Phi}_i\mathbf{A}_i + (\mathbf{\Phi}_{i+1}\mathbf{\Phi}_{i+1}^{\mathrm{T}} + \cdots + \mathbf{\Phi}_p\mathbf{\Phi}_p^{\mathrm{T}})\mathbf{U}_i \tag{3.68}$$

Thus, introduce the matrix, $\tilde{\mathbf{C}}$, of extended amplitudes for the truncated SPOD by

$$\tilde{\mathbf{C}} = \begin{bmatrix} \mathbf{A}_1 & \mathbf{\Phi}_1^{\mathrm{T}}\mathbf{U}_2 & \mathbf{\Phi}_1^{\mathrm{T}}\mathbf{U}_3 & \cdots & \mathbf{\Phi}_1^{\mathrm{T}}\mathbf{U}_p \\ \mathbf{\Phi}_2^{\mathrm{T}}\mathbf{U}_1 & \mathbf{A}_2 & \mathbf{\Phi}_2^{\mathrm{T}}\mathbf{U}_3 & \cdots & \mathbf{\Phi}_2^{\mathrm{T}}\mathbf{U}_p \\ \mathbf{\Phi}_3^{\mathrm{T}}\mathbf{U}_1 & \mathbf{\Phi}_3^{\mathrm{T}}\mathbf{U}_2 & \mathbf{A}_3 & \ddots & \vdots \\ \vdots & \vdots & \ddots & \ddots & \mathbf{\Phi}_{p-1}^{\mathrm{T}}\mathbf{U}_p \\ \mathbf{\Phi}_p^{\mathrm{T}}\mathbf{U}_1 & \mathbf{\Phi}_p^{\mathrm{T}}\mathbf{U}_2 & \cdots & \mathbf{\Phi}_p^{\mathrm{T}}\mathbf{U}_{p-1} & \mathbf{A}_p \end{bmatrix}. \tag{3.69}$$

The improved reconstruction can then be written as

$$\mathbf{U} = \mathbf{\Phi}\tilde{\mathbf{C}}. \tag{3.70}$$

When a sufficiently large number of modes are included for each block the sum of eigenvalues for the ignored modes of each block becomes small. Then, the matrix, $\tilde{\mathbf{C}}$, of extended amplitudes becomes nearly identical to the matrix, $\mathbf{C}$, of amplitudes.

3.2.3 SPOD with following components

When transforming

$$\begin{bmatrix} \mathbf{U} \\ \mathbf{V} \end{bmatrix} = \begin{bmatrix} \mathbf{U}_1 & \cdots & \mathbf{U}_p \\ \mathbf{V}_1 & \cdots & \mathbf{V}_p \end{bmatrix} \tag{3.71}$$

by using only

$$\mathbf{U}_{i+1} - (\mathbf{\Phi}_1\mathbf{\Phi}_1^{\mathrm{T}} + \cdots + \mathbf{\Phi}_i\mathbf{\Phi}_i^{\mathrm{T}})\mathbf{U}_{i+1} = \mathbf{\Phi}_{i+1}\mathbf{\Lambda}_{i+1}^{\frac{1}{2}}\mathbf{G}_{i+1}^{\mathrm{T}} = \mathbf{\Phi}_{i+1}\mathbf{A}_{i+1}. \tag{3.72}$$

and

$$\mathbf{U} = \mathbf{\Phi}\mathbf{C} \tag{3.73}$$

it is desired that

$$\mathbf{\Psi} = [\mathbf{\Psi}_1 \quad \cdots \quad \mathbf{\Psi}_p] \tag{3.74}$$

where

$$\mathbf{V} = \mathbf{\Psi}\mathbf{C} \tag{3.75}$$

This yields

$$\mathbf{V} = \mathbf{\Psi}\mathbf{A} + \begin{bmatrix}\mathbf{0} & \mathbf{\Psi}_1\mathbf{\Phi}_1^{\mathrm{T}}\mathbf{U}_2 & \cdots & (\mathbf{\Psi}_1\mathbf{\Phi}_1^{\mathrm{T}} + \cdots + \mathbf{\Psi}_{p-1}\mathbf{\Phi}_{p-1}^{\mathrm{T}})\mathbf{U}_p\end{bmatrix} \tag{3.76}$$

i.e.

$$\mathbf{V}_{i+1} - (\mathbf{\Psi}_1\mathbf{\Phi}_1^{\mathrm{T}} + \cdots + \mathbf{\Psi}_i\mathbf{\Phi}_i^{\mathrm{T}})\mathbf{U}_{i+1} = \mathbf{\Psi}_{i+1}\mathbf{A}_{i+1}. = \mathbf{\Psi}_{i+1}\mathbf{\Lambda}_{i+1}^{\frac{1}{2}}\mathbf{G}_{i+1}^{\mathrm{T}} \tag{3.77}$$

Chapter 4

A low-dimensional model for the cylinder with a rod

4.1 Introduction to low-dimensional models

Low-dimensional models of systems governed by differential equations can be constructed by projecting the equations on a truncated basis of Fourier modes, wavelets, polynomials, POD modes or modes resulting from combinations of several different transformations. The advantage of using POD modes is that the modes are calculated in order to suit the specific problem in contrast to for instance the Fourier modes which are given a priori. Of course, this is also a disadvantage because the solution of the problem must be known before the POD modes can be found.

4.1.1 POD-Galerkin models

The type of low-dimensional model based on POD modes has been termed a POD-Galerkin model because the projection of the equations on the modes is called a Galerkin projection. It is sometimes also called an empirical pseudo-spectral model. In the literature, POD is also known as Singular Value Decomposition (SVD), Karhunen-Loéve Transformation (KLT) and Empirical Orthogonal Functions (EOF). Strictly speaking, a Galerkin projection requires the modes to satisfy the boundary conditions individually. However, this requirement is not necessarily satisfied for low-dimensional models based on projection on POD modes. Without consideration of the boundary conditions, the term *POD-Galerkin model* is commonly used for this type of low-dimensional model within the context of hydrodynamics.

POD-Galerkin models have appeared not only in hydrodynamics, but in such diverse areas as for instance rapid thermal processing systems for manufacturing of semiconductor devices [2], control of chaos in reaction and diffusion processes [30] and stabilization of laser

arrays by means of delayed optical feedback [24].

POD was first introduced to the fluid mechanics society in 1967 by Lumley [19] who suggested that eddies in turbulent flows can be interpreted as POD modes. Since this initial motivation for using POD to resolve turbulent fluid flow fields, the first model capable of reproducing realistic low-dimensional dynamics of a turbulent flow system was presented in the pioneering paper of Aubry *et al.* [1]. More recent work has been carried out by Cazemier *et al.* [9] for a turbulent driven cavity flow. Several researchers have pursued investigation of transitional flows by means of POD-Galerkin models. A transitional rotating driven cavity flow has been investigated by Christensen *et al.* [10], [11], and a transitional grooved channel flow has been investigated by Bangia *et al.* [3] and, involving heat transfer, by Sahan *et al.* [26].

4.1.2 A basic POD-Galerkin model

As an example of a basic POD-Galerkin model consider the following. Using a fixed grid, discretization of the Navier-Stokes equations

$$\frac{\partial}{\partial t}\mathbf{u} + (\mathbf{u}\cdot\nabla)\mathbf{u} = \nabla p + \frac{1}{\mathrm{Re}}\nabla^2\mathbf{u} \tag{4.1}$$

and the continuity equation for incompressible flow

$$\nabla\cdot\mathbf{u} = 0 \tag{4.2}$$

results in a large system of autonomous ODE's (i.e. ordinary differential equations with no time-dependent coefficients) on the form

$$\frac{d}{dt}\mathbf{x}(t) = \mathbf{f}(\mathbf{x}(t), \mathrm{Re}). \tag{4.3}$$

When solving this system by numerical methods a set of data is generated

$$\{\mathbf{x}(t) \mid t = t_1,\ t_2,\ \ldots,\ t_n\} \tag{4.4}$$

for which a POD can be calculated. Defining the mean vector,

$$\mathbf{x}_0 = \frac{1}{n}\sum_{i=1}^{n}\mathbf{x}(t_i), \tag{4.5}$$

and denoting the matrix of POD modes by $\mathbf{\Phi}$, the system data can be reconstructed by

$$\mathbf{x}(t) = \mathbf{x}_0 + \mathbf{\Phi}\mathbf{a}(t) \tag{4.6}$$

where $\mathbf{a}(t)$ denotes the POD amplitudes for $t = t_1,\ t_2,\ \ldots,\ t_n$.

Taking the time derivative,

$$\frac{d}{dt}\mathbf{x}(t) = \mathbf{\Phi}\frac{d}{dt}\mathbf{a}(t), \tag{4.7}$$

and multiplying by $\mathbf{\Phi}^{\mathrm{T}}$ one obtains

$$\frac{d}{dt}\mathbf{a}(t) = \mathbf{\Phi}^{\mathrm{T}}\frac{d}{dt}\mathbf{x}(t). \tag{4.8}$$

Thus, projecting (4.3) on the POD modes,

$$\mathbf{\Phi}^{\mathrm{T}}\frac{d}{dt}\mathbf{x}(t) = \mathbf{\Phi}^{\mathrm{T}}\mathbf{f}(\mathbf{x}(t), \mathrm{Re}), \tag{4.9}$$

and substituting using (4.6) and (4.8), a Galerkin projection on the POD modes of the ODE system is obtained

$$\frac{d}{dt}\mathbf{a}(t) = \mathbf{\Phi}^{\mathrm{T}}\mathbf{f}(\mathbf{x}_0 + \mathbf{\Phi}\mathbf{a}(t), \mathrm{Re}), \tag{4.10}$$

This type of model is known as a *POD-Galerkin model* or an *empirically based pseudo-spectral model.* Truncating the set of POD basis vectors results in a *reduced model* or a *low-dimensional model.*

4.2 The discretized equations

For the lid driven cavity with a rotating rod a low-dimensional model of the axisymmetric flow can be produced by Galerkin projection on orthogonal modes of the azimuthal transport equations for vorticity and velocity.

4.2.1 The transport equations

Defining $u = v_r$, $v = v_\theta$ and $w = v_z$, the vorticity transport equation (2.9) becomes

$$\frac{\partial\omega}{\partial t} = -\frac{\partial}{\partial r}(u\omega) - \frac{\partial}{\partial z}(w\omega) + \frac{1}{r}\frac{\partial}{\partial z}(v^2) + \frac{1}{\mathrm{Re}}\left(-\frac{1}{r^2}\omega + \frac{1}{r}\frac{\partial}{\partial r}\left(r\frac{\partial\omega}{\partial r}\right) + \frac{\partial^2\omega}{\partial z^2}\right) \tag{4.11}$$

and the azimuthal velocity transport equation (2.10) becomes

$$\frac{\partial}{\partial t}v = -\frac{\partial}{\partial r}(uv) - \frac{\partial}{\partial z}(wv) - \frac{2}{r}uv + \frac{1}{\mathrm{Re}}\left(-\frac{1}{r^2}v + \frac{1}{r}\frac{\partial}{\partial r}\left(r\frac{\partial v}{\partial r}\right) + \frac{\partial^2 v}{\partial z^2}\right). \tag{4.12}$$

4.2.2 The Poisson equation is not projected

It is not necessary to include the Poisson equation (2.8),

$$r\omega = \frac{\partial^2\psi}{\partial r^2} - \frac{1}{r}\frac{\partial\psi}{\partial r} + \frac{\partial^2\psi}{\partial z^2}, \tag{4.13}$$

in the Galerkin projection because once the vorticity is known from the transport equations, the stream function and its spatial derivatives are known from the orthogonal modes as following components.

4.2.3 Discretization

Since the spatial information of the low-dimensional model is included via the modes, it is not necessary to employ any special or high-order spatial discretization. By using second order central differences the following is obtained,

$$\begin{aligned}\frac{d}{dt}\omega_{i,j} &= \frac{1}{\mathrm{Re}}\left\{\frac{r_{j+1}+r_j}{2r_j\Delta r^2}\omega_{i,j+1} - \left(\frac{1}{r_j^2}+\frac{r_{j+1}+2r_j+r_{j-1}}{2r_j\Delta r^2}\right)\omega_{i,j}\right.\\ &\left.+\frac{r_j+r_{j-1}}{2r_j\Delta r^2}\omega_{i,j-1}+\frac{1}{\Delta z^2}\left(\omega_{i+1,j}-2\omega_{i,j}+\omega_{i-1,j}\right)\right\}\\ &-\frac{1}{2\Delta r}u_{i,j+1}\omega_{i,j+1}+\frac{1}{2\Delta r}u_{i,j-1}\omega_{i,j-1}\\ &-\frac{1}{2\Delta z}w_{i+1,j}\omega_{i+1,j}+\frac{1}{2\Delta z}w_{i-1,j}\omega_{i-1,j}\\ &+\frac{1}{2r_j\Delta z}v_{i+1,j}v_{i+1,j}-\frac{1}{2r_j\Delta z}v_{i-1,j}v_{i-1,j}\end{aligned} \tag{4.14}$$

$$\begin{aligned}\frac{d}{dt}v_{i,j} &= \frac{1}{\mathrm{Re}}\left\{\frac{r_{j+1}+r_j}{2r_j\Delta r^2}v_{i,j+1} - \left(\frac{1}{r_j^2}+\frac{r_{j+1}+2r_j+r_{j-1}}{2r_j\Delta r^2}\right)v_{i,j}\right.\\ &\left.+\frac{r_j+r_{j-1}}{2r_j\Delta r^2}v_{i,j-1}+\frac{1}{\Delta z^2}\left(v_{i+1,j}-2v_{i,j}+v_{i-1,j}\right)\right\}\\ &-\frac{1}{2\Delta r}u_{i,j+1}v_{i,j+1}-\frac{2}{r_j}u_{i,j}v_{i,j}+\frac{1}{2\Delta r}u_{i,j-1}v_{i,j-1}\\ &-\frac{1}{2\Delta z}w_{i+1,j}v_{i+1,j}+\frac{1}{2\Delta z}w_{i-1,j}v_{i-1,j}\end{aligned} \tag{4.15}$$

The mean value of v_{ij} is called v_{ij}^0. Then v_{ij} is redefined so that v_{ij} is replaced by $v_{ij}+v_{ij}^0$. Similarly, ω_{ij} redefined to be replaced by $\omega_{ij}+\omega_{ij}^0$, u_{ij} is redefined to be replaced by $u_{ij}+u_{ij}^0$ and w_{ij} is redefined to be replaced by $w_{ij}+w_{ij}^0$. Before the Galerkin projection is carried out the equations are written as

$$\begin{aligned}\frac{d\omega_{ij}}{dt} &= \frac{1}{\mathrm{Re}}G_{ijkl}(\omega_{kl}+\omega_{kl}^0)\\ &+(u_{mn}+u_{mn}^0)M_{ijklmn}(\omega_{kl}+\omega_{kl}^0)\\ &+(w_{mn}+w_{mn}^0)N_{ijklmn}(\omega_{kl}+\omega_{kl}^0)\\ &+(F_{mnef}v_{ef}+F_{mnef}v_{ef}^0+I_{mn}+\gamma J_{mn})\\ &P_{ijklmn}(F_{klgh}v_{gh}+F_{klgh}v_{gh}^0+I_{kl}+\gamma J_{kl})\end{aligned} \tag{4.16}$$

$$\begin{aligned}\frac{dv_{ij}}{dt} &= \frac{1}{\mathrm{Re}}H_{ijkl}(F_{klef}v_{ef}+F_{klef}v_{ef}^0+I_{kl}+\gamma J_{kl})\\ &+(u_{mn}+u_{mn}^0)S_{ijklmn}(F_{klef}v_{ef}+F_{klef}v_{ef}^0+I_{kl}+\gamma J_{kl})\\ &+(w_{mn}+w_{mn}^0)T_{ijklmn}(F_{klef}v_{ef}+F_{klef}v_{ef}^0+I_{kl}+\gamma J_{kl}).\end{aligned} \tag{4.17}$$

where $I_{ij}+\gamma J_{ij}$ contains the inhomogeneous boundary conditions for the azimuthal velocity.

4.2.4 The boundary conditions

$I_{ij} + \gamma J_{ij}$ contains the inhomogeneous boundary conditions for the azimuthal velocity on the lid and the rod. These boundary conditions are implemented by letting $F_{ijkl} = 1$ for $(i,j) = (k,l)$ except for (i,j) on the boundaries for the lid and the rod. For i and j on the boundary of the lid and on the boundary of the rod $F_{ijkl} = 0$. For i on the lid, $I_{ij} = 1/r_j$, otherwise $I_{ij} = 0$. For j on the rod, $J_{ij} = 1/r_j$, otherwise $J_{ij} = 0$. The azimuthal velocity is zero on the two other boundaries, i.e. on the cylinder wall and the fixed bottom.

The author has not previously seen any records in the literature of inhomogeneous boundary conditions of velocity implemented by other means than via the mean field in low-dimensional models based on projection on POD modes.

According to (2.13), (2.14), (2.15) and (2.16), the boundary conditions for the vorticity are linear relationships between the vorticity and the stream function. Thus, any mode satisfies the boundary conditions for the vorticity because it is a linear combination of the original snapshots. Since the vorticity is replaced by a linear combination of modes, the boundary conditions for the vorticity are automatically satisfied by the equations resulting from the projection of the governing equations on the modes.

4.2.5 Collected form

In order to state the discretized equations in a form, which is more suitable for the projection on the orthogonal modes, the tensors v_{ij} and ω_{ij} are collected into a single tensor and the coefficients are reorganized accordingly. The notation utilized for this purpose needs to be explained at this point. Introducing

$$\{y_{ij}\} = \begin{pmatrix} \{u_{i_* j_-}\} \\ \{w_{i_* j_*}\} \end{pmatrix},$$

$$\{A_{ijkl}\} = \begin{pmatrix} \{A^1_{i_* j_- k_* l_-}\} & \{A^2_{i_* j_- k_* l_*}\} \\ \{A^3_{i_* j_- k_* l_-}\} & \{A^4_{i_* j_- k_* l_-}\} \end{pmatrix},$$

$$\{Q_{ijklmn}\} = \begin{pmatrix} \left(\{B^1_{i_* j_- k_* l_- m_* n_*}\} & \{C^1_{i_* j_* k_* l_* m_- n_-}\}\right) & \left(\{B^2_{i_* j_- k_* l_- m_* n_*}\} & \{C^2_{i_* j_* k_* l_* m_- n_-}\}\right) \\ \left(\{B^3_{i_* j_- k_* l_- m_* n_*}\} & \{C^3_{i_* j_* k_* l_* m_- n_-}\}\right) & \left(\{B^4_{i_* j_- k_* l_- m_* n_*}\} & \{C^4_{i_* j_* k_* l_* m_- n_-}\}\right) \end{pmatrix},$$

it is understood that

$$\{A_{ijkl} y_{kl}\} = \begin{pmatrix} \{A^1_{i_* j_- k_* l_-} u_{k_* l_-} + A^2_{i_* j_* k_- l_*} w_{k_- l_*}\} \\ \{A^3_{i_* j_- k_* l_-} u_{k_* l_-} + A^4_{i_* j_* k_- l_*} w_{k_- l_*}\} \end{pmatrix}$$

and

$$\{Q_{ijklmn} y_{mn}\} = \begin{pmatrix} \{D^1_{i_* j_* k_- l_-}\} & \{D^2_{i_* j_* k_* l_*}\} \\ \{D^3_{i_* j_* k_- l_-}\} & \{D^4_{i_* j_- k_* l_*}\} \end{pmatrix}$$

where

$$
\begin{aligned}
D^1_{i_*j_*k_*l_*} &= B^1_{i_*j_*k_*l_*m_*n_*}u_{m_*n_*} + C^1_{i_*j_*k_*l_*m_*n_*}w_{m_*n_*},\\
D^2_{i_*j_*k_*l_*} &= B^2_{i_*j_*k_*l_*m_*n_*}u_{m_*n_*} + C^2_{i_*j_*k_*l_*m_*n_*}w_{m_*n_*},\\
D^3_{i_*j_*k_*l_*} &= B^3_{i_*j_*k_*l_*m_*n_*}u_{m_*n_*} + C^3_{i_*j_*k_*l_*m_*n_*}w_{m_*n_*},\\
D^4_{i_*j_*k_*l_*} &= B^4_{i_*j_*k_*l_*m_*n_*}u_{m_*n_*} + C^4_{i_*j_*k_*l_*m_*n_*}w_{m_*n_*}.
\end{aligned}
$$

Now, define

$$\{x_{ij}\} = \begin{pmatrix} \{\omega_{i_*j_*}\} \\ \{v_{i_*j_*}\} \end{pmatrix}, \quad \{y_{ij}\} = \begin{pmatrix} \{u_{i_*j_*}\} \\ \{w_{i_*j_*}\} \end{pmatrix} \tag{4.18}$$

$$\{B_{ij}\} = \begin{pmatrix} \mathbf{0} \\ \{I_{i_*j_*}\} \end{pmatrix}, \quad \{C_{ij}\} = \begin{pmatrix} \mathbf{0} \\ \{J_{i_*j_*}\} \end{pmatrix} \tag{4.19}$$

$$\{A_{ijkl}\} = \begin{pmatrix} \{G_{i_*j_*k_*l_*}\} & \mathbf{0} \\ \mathbf{0} & \{H_{i_*j_*k_*l_*}\} \end{pmatrix}, \quad \{L_{ijkl}\} = \begin{pmatrix} \{E_{i_*j_*k_*l_*}\} & \mathbf{0} \\ \mathbf{0} & \{F_{i_*j_*k_*l_*}\} \end{pmatrix} \tag{4.20}$$

$$\{Q_{ijklmn}\} = \begin{pmatrix} \begin{pmatrix} \{M_{i_*j_*k_*l_*m_*n_*}\} & \{N_{i_*j_*k_*l_*m_*n_*}\} \end{pmatrix} & \begin{pmatrix} \mathbf{0} & \mathbf{0} \end{pmatrix} \\ \begin{pmatrix} \mathbf{0} & \mathbf{0} \end{pmatrix} & \begin{pmatrix} \{S_{i_*j_*k_*l_*m_*n_*}\} & \{T_{i_*j_*k_*l_*m_*n_*}\} \end{pmatrix} \end{pmatrix} \tag{4.21}$$

$$\{K_{ijklmn}\} = \begin{pmatrix} \begin{pmatrix} \mathbf{0} & \mathbf{0} \end{pmatrix} & \begin{pmatrix} \mathbf{0} & \{P_{i_*j_*k_*l_*m_*n_*}\} \end{pmatrix} \\ \begin{pmatrix} \mathbf{0} & \mathbf{0} \end{pmatrix} & \begin{pmatrix} \mathbf{0} & \mathbf{0} \end{pmatrix} \end{pmatrix} \tag{4.22}$$

The equations (4.16) and (4.17) can then be stated on the collected form

$$
\begin{aligned}
\frac{d}{dt}x_{ij} &= \frac{1}{\mathrm{Re}}A_{ijkl}(L_{klef}x_{ef} + L_{klef}x^0_{ef} + B_{kl} + \gamma C_{kl})\\
&\quad + Q_{ijklmn}(y_{mn} + y^0_{mn})(L_{klef}x_{ef} + L_{klef}x^0_{ef} + B_{kl} + \gamma C_{kl})\\
&\quad + K_{ijklmn}(L_{mnef}x_{ef} + L_{mnef}x^0_{ef} + B_{mn} + \gamma C_{mn})\\
&\quad (L_{klgh}x_{gh} + L_{klgh}x^0_{gh} + B_{kl} + \gamma C_{kl}).
\end{aligned} \tag{4.23}
$$

4.3 Projection of equations on orthogonal modes

The equation (4.23) is not evaluated for (i, j) on the boundary. In order to project the equation on the orthogonal modes, $\boldsymbol{\phi}_p$, the boundary components are excluded from the snapshots before calculating the orthogonal modes which are then zero on the boundary. I.e. $\phi_{ijp} = 0$ for (i, j) on the boundary. However, in order to evaluate eq. (4.23) it is necessary to include the boundary components as *following components* by introducing the extended modes, $\tilde{\boldsymbol{\phi}}_p$, and letting $\tilde{\phi}_{ijp} = \phi_{ijp}$ for (i, j) not on the boundary. Furthermore, the components of $\mathbf{y}$ are treated as following components and include the boundary.

By projecting (4.23) on the orthogonal modes, ϕ_{ijp}, replacing

$$x_{ij} = \tilde{\phi}_{ijp} a_p, \quad y_{ij} = \xi_{ijp} a_p \tag{4.24}$$

and observing

$$\phi_{ijq}\phi_{ijp}\frac{da_p}{dt} = \frac{da_q}{dt}, \quad \frac{dx_{ij}}{dt} = \phi_{ijp}\frac{da_p}{dt}, \tag{4.25}$$

it is obtained that

$$\begin{aligned}
\frac{da_q}{dt} &= \frac{1}{\mathrm{Re}}\phi_{ijq}A_{ijkl}(L_{klef}\tilde{\phi}_{efp}a_p + L_{klef}x^0_{ef} + B_{kl} + \gamma C_{kl}) \\
&+\phi_{ijq}Q_{ijkklmn}(\xi_{mnr}a_r + y^0_{mn})(L_{klef}\tilde{\phi}_{efp}a_p + L_{klef}x^0_{ef} + B_{kl} + \gamma C_{kl}) \\
&+\phi_{ijq}K_{ijkklmn}(L_{mnef}\tilde{\phi}_{efr}a_r + L_{mnef}x^0_{ef} + B_{mn} + \gamma C_{mn}) \\
&(L_{klgh}\tilde{\phi}_{ghp}a_p + L_{klgh}x^0_{gh} + B_{kl} + \gamma C_{kl}),
\end{aligned} \tag{4.26}$$

where i and j on the boundaries are not included. Collecting terms,

$$\frac{da_q}{dt} = \frac{1}{\mathrm{Re}}\alpha_{pq}a_p + \frac{1}{\mathrm{Re}}\beta_q + \frac{\gamma}{\mathrm{Re}}\delta_q + \zeta_{pq}a_p + \gamma\eta_{pq}a_p + \kappa_{prq}a_p a_r + \gamma^2\sigma_q + \gamma\mu_q + \tau_q. \tag{4.27}$$

The coefficients of the collected terms are given by

$$\alpha_{pq} = \phi_{ijq}A_{ijkl}L_{klef}\tilde{\phi}_{efp} \tag{4.28}$$

$$\beta_{pq} = \phi_{ijq}A_{ijkl}(L_{klef}x^0_{ef} + B_{kl}) \tag{4.29}$$

$$\delta_{pq} = \phi_{ijq}A_{ijkl}C_{kl} \tag{4.30}$$

$$\begin{aligned}
\zeta_{pq} &= \phi_{ijq}Q_{ijklmn}(\xi_{mnp}(L_{klef}x^0_{ef} + B_{kl}) + y^0_{mn}L_{klef}\tilde{\phi}_{efp}) \\
&+\phi_{ijq}K_{ijklmn}\Big(L_{mnef}\tilde{\phi}_{efp}(L_{klgh}x^0_{gh} + B_{kl}) \\
&+L_{klgh}\phi_{ghp}(L_{mnef}x^0_{ef} + B_{mn})\Big)
\end{aligned} \tag{4.31}$$

$$\begin{aligned}
\eta_{pq} &= \phi_{ijq}Q_{ijklmn}\xi_{mnp}C_{kl} \\
&+\phi_{ijq}K_{ijklmn}(L_{mnef}\tilde{\phi}_{efp}C_{kl} + L_{klgh}\tilde{\phi}_{ghp}C_{mn})
\end{aligned} \tag{4.32}$$

$$\begin{aligned}
\kappa_{prq} &= \phi_{ijq}Q_{ijklmn}\xi_{mnr}L_{klef}\tilde{\phi}_{efp} \\
&+\phi_{ijq}K_{ijklmn}L_{mnef}\tilde{\phi}_{efr}L_{klgh}\tilde{\phi}_{ghp}
\end{aligned} \tag{4.33}$$

$$\sigma_q = \phi_{ijq}K_{ijklmn}C_{mn}C_{kl} \tag{4.34}$$

$$\begin{aligned}
\mu_q &= \phi_{ijq}Q_{ijklmn}y^0_{mn}C_{kl} \\
&+\phi_{ijq}K_{ijklmn}((L_{mnef}x^0_{ef} + B_{mn})C_{kl} + (L_{klgh}x^0_{gh} + B_{kl})C_{mn})
\end{aligned} \tag{4.35}$$

$$\begin{aligned}
\tau_q &= \phi_{ijq}Q_{ijklmn}y^0_{mn}(L_{klgh}x^0_{gh} + B_{kl}) \\
&+\phi_{ijq}K_{ijklmn}(L_{mnef}x^0_{ef} + B_{mn})(L_{klgh}x^0_{gh} + B_{kl})
\end{aligned} \tag{4.36}$$

At this point, it can be seen from (4.32) that

$$\eta_{pq} = 0 \tag{4.37}$$

because according to (4.19) C_{kl} is zero except for the part called J_{ij} representing the boundary condition for the azimuthal velocity on the rod. The term of (4.32) containing Q_{ijklmn} only involves terms containing M_{ijklmn}, N_{ijklmn}, S_{ijklmn} and T_{ijklmn}. Regarding (4.16) and (4.17) it is seen that these terms are the convection terms, i.e. the nonlinear terms containing the axial and radial velocities. By looking at (4.14) and (4.15) one may conclude that the relevant terms only involve identical radial indices for the azimuthal velocity and the two other velocity components. Recalling the boundary conditions for the rod given in (2.16) it is readily seen that the axial and radial velocities are zero on the rod. Thus, the term of (4.32) containing Q_{ijklmn} is zero. The term of (4.32) containing K_{ijklmn} is zero because it represents the nonlinear terms of (4.14) involving only the azimuthal velocity. By similar arguments it is found that

$$\sigma_q = 0, \tag{4.38}$$

$$\mu_q = 0. \tag{4.39}$$

Thus, (4.27) reduces to

$$\frac{da_q}{dt} = \frac{1}{\mathrm{Re}}\alpha_{pq}a_p + \frac{1}{\mathrm{Re}}\beta_q + \frac{\gamma}{\mathrm{Re}}\delta_q + \zeta_{pq}a_p + \kappa_{prq}a_p a_r + \tau_q. \tag{4.40}$$

4.4 Runge-Kutta solver

Representing the model by

$$\frac{d}{dt}\mathbf{a} = \boldsymbol{\Upsilon}(\mathbf{a}) \tag{4.41}$$

for given γ and Re, it can be solved numerically by the Runge-Kutta method

$$\boldsymbol{\Gamma}_1 = \Delta t\boldsymbol{\Upsilon}(\mathbf{a}^n) \tag{4.42}$$

$$\boldsymbol{\Gamma}_2 = \Delta t\boldsymbol{\Upsilon}(\mathbf{a}^n + \frac{1}{2}\boldsymbol{\Gamma}_1) \tag{4.43}$$

$$\boldsymbol{\Gamma}_3 = \Delta t\boldsymbol{\Upsilon}(\mathbf{a}^n + \frac{1}{2}\boldsymbol{\Gamma}_2) \tag{4.44}$$

$$\boldsymbol{\Gamma}_4 = \Delta t\boldsymbol{\Upsilon}(\mathbf{a}^n + \boldsymbol{\Gamma}_3) \tag{4.45}$$

$$\mathbf{a}^{n+1} = \mathbf{a}^n + \frac{1}{6}(\boldsymbol{\Gamma}_1 + 2\boldsymbol{\Gamma}_2 + 2\boldsymbol{\Gamma}_3 + \boldsymbol{\Gamma}_4). \tag{4.46}$$

4.5 Verification of simple properties

The equations (4.11), (4.12) and (4.13) governing the original problem can be represented by

$$\frac{d}{dt}\mathbf{x}(t) = \mathbf{f}(\mathbf{x}(t),\ \mathbf{y}(t),\ \mathrm{Re},\ \gamma), \tag{4.47}$$

$$\mathbf{y}(t) = \mathbf{g}(\mathbf{x}(t)). \tag{4.48}$$

Hence, it can be stated that

$$\frac{d}{dt}\mathbf{x}(t) = \mathbf{h}(\mathbf{x}(t),\ \mathrm{Re},\ \gamma). \tag{4.49}$$

For parameters (Re, γ) corresponding to a steady state, i.e.

$$\mathbf{h}(\mathbf{x}(t),\ \mathrm{Re},\ \gamma) = \mathbf{0}, \tag{4.50}$$

the eigenvalue problem

$$\left\{\frac{\partial h_k}{\partial x_i}\right\}\mathbf{\Phi} = \mathbf{\Phi}\begin{pmatrix} \mu_1 & & 0 \\ & \ddots & \\ 0 & & \mu_n \end{pmatrix} \tag{4.51}$$

must yield eigenvalues satisfying $\mu_k \leq 0$ for $k = 1, 2, \ldots, n$. The low-dimensional model assumes a linear relationship between $\mathbf{x}$ and $\mathbf{a}$ given by (4.24). Thus if the low-dimensional model is a faithful representation of the original problem, it should be able to reproduce a steady state, i.e.

$$\frac{d\mathbf{a}}{dt} = \mathbf{0}, \tag{4.52}$$

and the eigenvalue problem

$$\left\{\frac{\partial}{\partial a_p}\frac{da_q}{dt}\right\}\mathbf{\Psi} = \mathbf{\Psi}\begin{pmatrix} \eta_1 & & 0 \\ & \ddots & \\ 0 & & \eta_m \end{pmatrix} \tag{4.53}$$

should yield eigenvalues satisfying $\eta_p \leq 0$ for $p = 1, 2, \ldots, m$. From the low-dimensional model (4.40) it is easily found that

$$\frac{\partial}{\partial a_p}\frac{da_q}{dt} = \frac{1}{\mathrm{Re}}\alpha_{pq} + \zeta_{pq} + (\kappa_{prq} + \kappa_{rpq})a_r. \tag{4.54}$$

This fact can be used for a simple verification of the low-dimensional model.

In order to analyze more complicated features of the low-dimensional model it noted from (4.40) that

$$\frac{\partial}{\partial(\mathrm{Re})}\frac{da_q}{dt} = -\frac{1}{\mathrm{Re}^2}\alpha_{pq}a_p - \frac{1}{\mathrm{Re}^2}\beta_q - \frac{\gamma}{\mathrm{Re}^2}\delta_q, \tag{4.55}$$

$$\frac{\partial}{\partial\gamma}\frac{da_q}{dt} = \frac{1}{\mathrm{Re}}\delta_q. \tag{4.56}$$

Chapter 5

Low-dimensional models of transition

5.1 Introduction

Very little is known about how the properties of a low-dimensional model are affected by the procedures applied in its construction. How should the data used be sampled? Which decomposition technique is optimal for transforming the data into modes? How should the modes be selected? What is the effect of numerical noise? These are questions that are difficult to answer.

The goal of the present study is to construct low-dimensional models of the flow in the lid driven cavity with a rod and to explore the transition occurring for varying parameter values. Some investigation was performed with different methods of data sampling and variations of the decomposition procedure.

The models were analyzed with AUTO 97, continuation and bifurcation software for ordinary differential equations. This software was developed by E. J. Doedel *et al.* [14]. Via the computer program odecav, the Runge-Kutta solver described in 4.4 was used to solve the ODE's of the low-dimensional models for different parameter values in order to verify the results of AUTO 97.

Unfortunately, only few validation methods exist. Furthermore, the body of literature, to which the performance of the models can be compared, is very limited. However, the articles of E. A. Christensen *et al.* [10] and E. A. Christensen *et al.* [11] were available for the cavity without a rod.

Section 5.2 presents the validations that were performed. In the remaining part of Chapter 5 the various low-dimensional models and their solutions will be presented.

5.2 Validation

5.2.1 A low-dimensional model of the lid driven cavity without a rod

In order to compare the solutions of the current type of low-dimensional model with results obtained in the earlier work of E. A. Christensen *et al.* [10] a special version of the low-dimensional model was implemented for the lid driven cavity without a rod. In this version, the boundary condition for the rod was replaced with a symmetry condition for the center axis by letting the azimuthal velocity $v_\theta = 0$ at this boundary in the projected equations. Furthermore, the computational grid was changed to incorporate the axis of symmetry instead of the rod.

5.2.2 Reproducing steady states

As a minimum, the low-dimensional model should be able to reproduce the steady states appearing in an ensemble consisting of steady states only. This was verified by using the model without the rod for an ensemble consisting of data for the Reynolds numbers 2200, 2300, 2400 and 2500. The ensemble mean field was subtracted from the snapshots and a POD with three modes was performed. the resulting model yielded solutions at the four Reynolds numbers for which the stream line plots, iso-vorticity plots and iso-circulation plots were compared to those of the original data. By visual inspection no differences were found between the two sets of plots.

5.2.3 Reproducing a Hopf bifurcation

Sørensen *et al.* [28] found that the transition from steady to unsteady flow in the lid driven cavity without a rod occurs via a Hopf bifurcation with a critical Reynolds number of 2550. The period of oscillation was found to be 26. E. A. Christensen *et al.* [10] used a low-dimensional model, referred to as type 1, to reproduce the Hopf bifurcation. For 5-10 modes plus 6 of the so-called displacement modes, the critical Reynolds number and the period deviated approximately 1% from the actual values.

In order to compare the performance of the current type of low-dimensional model with their model, it was necessary to implement the displacement modes in the current model and to calculate a data ensemble similar to the data used for their type 1.

The displacement modes are based on displacement vectors defined as the differences between sub-ensemble averages at fixed Reynolds numbers. The displacement modes are produced by adding the displacement vectors to the set of modes generated by POD and then perform Gram-Schmidt orthogonalization. In the current model, displacement vectors

can be calculated upon demand. By placing the snapshots to be transformed via the POD in the first block of the SPOD and placing each displacement vector in a separate block after the first block, the displacement modes were obtained.

For type 1, snapshots from $\mathrm{Re}_{lid} = 2600$ were used in the POD. Displacement modes were generated from all displacement vectors from neighboring sub-ensemble averages. With the notation used in Christensen *et al.* [10] the mentioned displacement vectors can be expressed as $X_{2500} - X_{2200}$, $\mu_{2600} - X_{2500}$, $\mu_{2700} - \mu_{2600}$, $\mu_{2800} - \mu_{2700}$, $\mu_{2900} - \mu_{2800}$ and $\mu_{3000} - \mu_{2900}$.

The unsteady data for the current model were sampled for a whole number of periods. The period was calculated for each Reynolds number via the FFT as described in 2.7.2. Before sampling of both the steady and the unsteady data it was verified, via plots of the RMS level explained in 2.7.4, that a sufficient number of time steps had been carried out in order to reach a state close to the limiting flow. Approximately 60-100 snapshots were included in each of the sub-ensembles of an unsteady limiting flow.

Type 1 models with 15 and 20 modes were produced (corresponding to 9 and 14 modes plus 6 displacement modes in the work of E. A. Christensen *et al.*). Using AUTO 97, for 15 modes the critical Reynolds number and period was found to be 2526 and 26.66 respectively. For 20 modes the results were 2532 and 26.58 respectively.

The SPOD is thought of as a more modern alternative to the use of displacement modes. An alternative to the type 1 model was tested in which the sub-ensemble for $\mathrm{Re}_{lid} = 2600$ was placed in the first block and the sub-ensembles for the Reynolds numbers 2200, 2500, 2700, 2800, 2900 and 3000 were placed in the following six blocks. Only one mode was allowed from each of the last four blocks (in effect this means that the sub-ensemble averages for the Reynolds numbers 2700, 2800, 2900 and 3000 were included via Gram-Schmidt orthogonalization). Using AUTO 97, for 15 modes this model yielded a Hopf bifurcation with a critical Reynolds number and period of 2541 and 26.42 respectively. For 20 modes, the result was 2550 and 26.36 respectively. Hence, the performance of the model compares favorably with type 1.

5.3 Modeling Hopf bifurcations for constant γ

5.3.1 Hopf bifurcation for a fixed rod

For the parameter $\gamma = 0$, i.e. for a fixed rod, the transition from steady to unsteady flow occurs via a Hopf bifurcation. In 2.7.7 the critical Reynolds number was estimated to be 2590. The full solution for a 201x101 computational grid and a time step of $\Delta t = 0.04$ has a period of 26.44 at $\mathrm{Re}_{lid} = 2600$. In order to establish data for constructing low-dimensional models of the Hopf bifurcation, the full solution was calculated for the Reynolds numbers

2300, 2540, 2620, 2700, 2800, 2900 and 3000. For each solution, the RMS level described in 2.7.4 was allowed to settle at a constant level in order to reach a state close to the limiting flow before the snapshots were sampled. This required $8 \cdot 10^5$ time steps with a time step of $\Delta t = 0.04$ for a 201x101 computational grid at $\mathrm{Re}_{lid} = 2540$, $5 \cdot 10^5$ time steps at $\mathrm{Re}_{lid} = 2620$ and at least 10^5 time steps further away from the critical Reynolds number. For unsteady flow, FFT's were calculated as described in 2.7.2 for ensembles with 2^{16} data points. The peak frequencies were found as in 2.7.3 and the periods were calculated.

At $\mathrm{Re}_{lid} = 2620$ a snapshot was sampled for every 58 time steps, yielding 68 snapshots corresponding to 6 periods of 26.2932. The actual period was found to be 26.2941. In this way it was ensured that each part of the period was represented nearly equally well.

The models to be presented in the following have been named arbitrarily. Thus, the letters of the model names do not refer to any specific concepts.

The skx model

The snapshot calculated for $\mathrm{Re}_{lid} = 2540$ was placed in the first block of the SPOD and the sub-ensemble containing the snapshots for $\mathrm{Re}_{lid} = 2620$ was placed in the second block. The ensemble consisting of the sub-ensembles arranged in the described order was assigned the label skx. The SPOD was carried out as described in 3.2. In order to obtain as high numerical accuracy as possible, a LAPACK SVD routine mentioned in Appendix B was used to calculate the POD's involved in the SPOD. By this method, a direct calculation of the auto-covariance matrix is avoided for the POD's. The relative eigenvalue spectrum of the SPOD is shown in Fig. 5.1.

The mode resulting from the first block is shown as mode number 1. The corresponding eigenvalue is less than the eigenvalue of mode number 2 which is the first mode of the second block. The eigenvalues decrease for increasing mode numbers. For mode number 12 the relative eigenvalue is less than 10^{-10} and the decay of the eigenvalues becomes much smaller than for the previous modes. This indicates that the ratio between the smallest and the largest eigenvalue is near the limit that can be obtained for the given ensemble of data. As mentioned in Appendix B, the SPOD utilizing the LAPACK SVD routine can represent the eigenvalues with at least 20 decades of accuracy. Thus, the observed change in the rate of decay of the eigenvalues with increasing numbers of modes cannot be caused by inaccuracies in the decomposition method. Instead, it must be due to the properties of the data ensemble that was used for the decomposition.

The SPOD of the skx ensemble was calculated for 5-20 modes. Each set of modes was used to construct a low-dimensional model as explained in Chapter 4.

The models were analyzed with AUTO 97 in order to find the critical Reynolds number

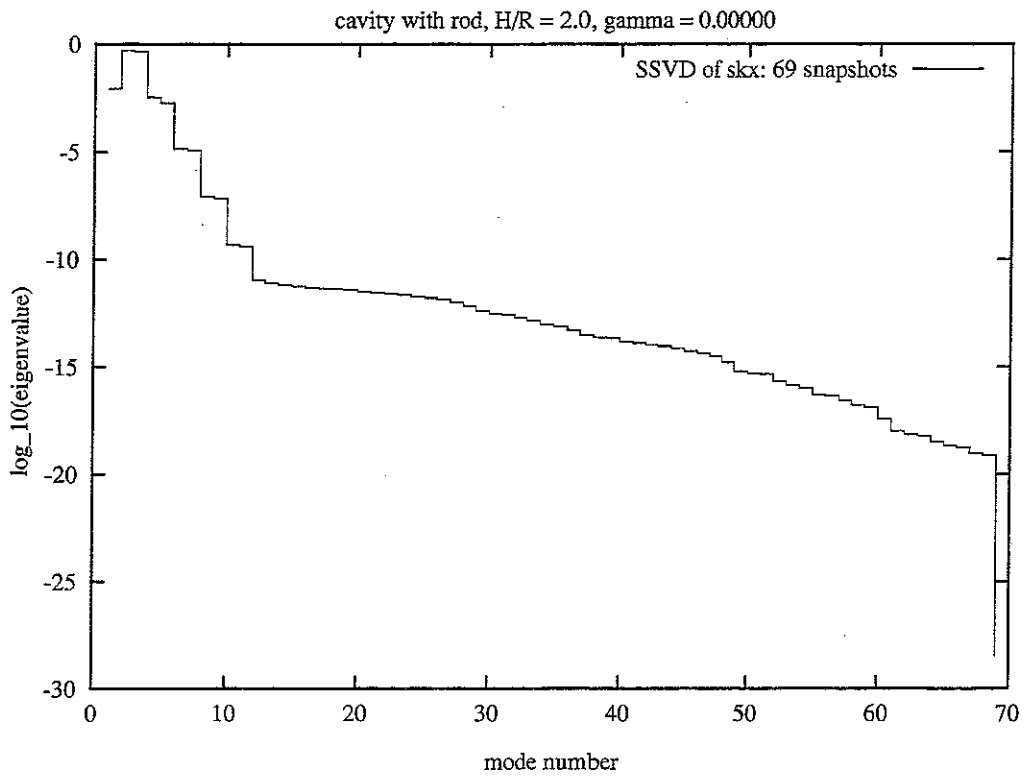

Figure 5.1: Relative eigenvalue spectrum for the SPOD of the skx data ensemble for $\gamma = 0.000$.

and the period. An example of the graphical output from AUTO 97 is shown for 6 modes in Fig. 5.4. The horizontal axis represents the Reynolds number and the vertical axis represents an L_2-norm used by AUTO 97. The diagram shows a steady solution. The full line represents a stable solution and the filled square indicates a Hopf bifurcation. The dashed line represents an unsteady solution or a solution for which stability is unknown.

In Fig. 5.2 the critical Reynolds number is shown as a function of the number of modes. It appears that more than 5 modes should be used. With only 6 modes a critical Reynolds number of 2602 is obtained. The deviation from the true value of 2590 is less than 0.5%. The corresponding period is 26.33 which deviates less than 0.5% from the true value of 24.4. For 6-18 modes, critical Reynolds numbers within the range $2601 - 2614$ are obtained. The deviation from the actual value of 2590 is less than 1%. The period shown in Fig. 5.3 lies within the range $26.32 - 26.40$.

Thus, very good representation of the period is obtained. For more than 19 modes the results of the low-dimensional model deviates significantly from the results of the full model. However, this was expected to occur for some number of modes larger than 12. It can be concluded that the skx model has a quite good performance and a consistent behavior within a reasonable large range of the number of modes.

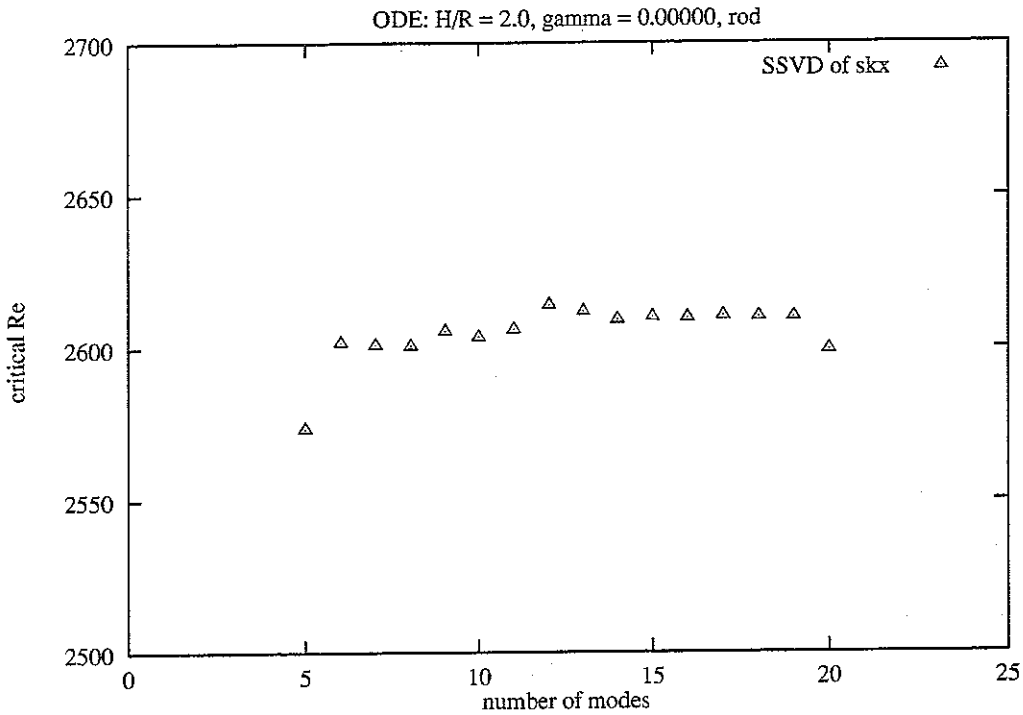

Figure 5.2: The critical Reynolds number of the skx model for $\gamma = 0.000$.

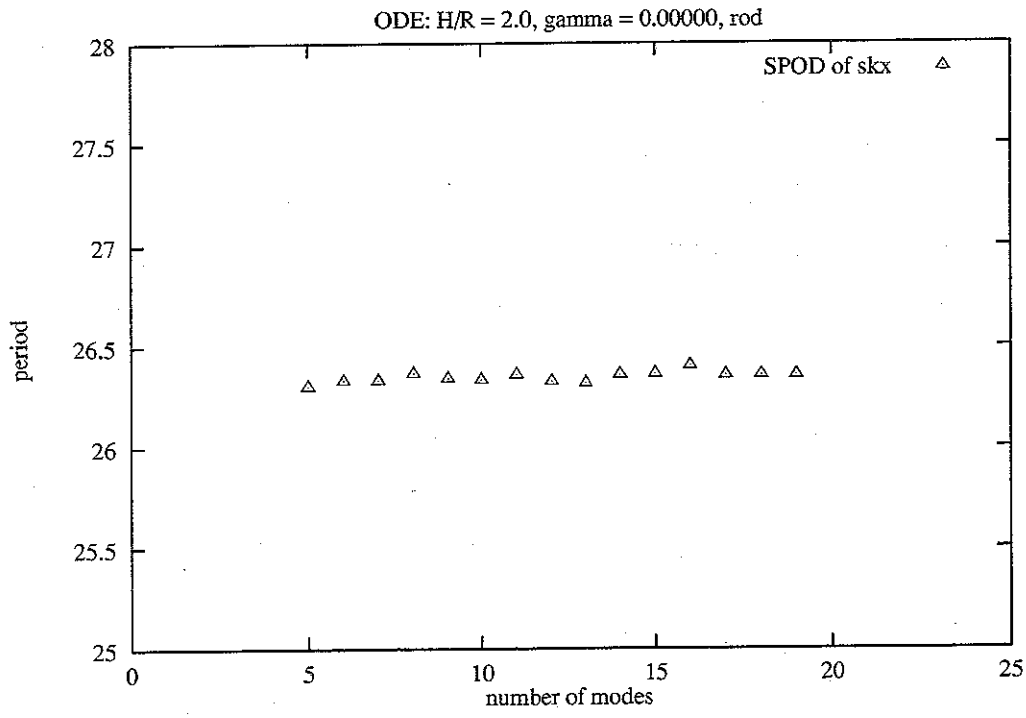

Figure 5.3: The period at the Hopf bifurcation of the skx model for $\gamma = 0.000$.

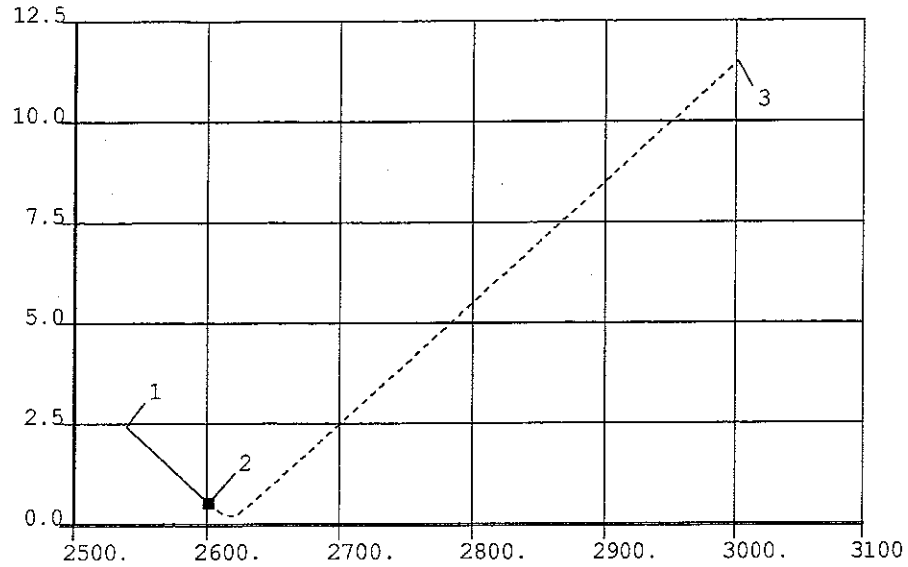

Figure 5.4: Graphical output from AUTO 97 of the steady solution of the skx model for $\gamma = 0.000$ with 6 modes. The horizontal axis represents the Reynolds number and the vertical axis represents an L_2-norm used by AUTO 97.

It is worth to note that this model is relatively simple. It is based only on a snapshot from the steady regime and a sub-ensemble of snapshots for one Reynolds number in the unsteady regime. Hence, in order to model a Hopf bifurcation, it is not necessary to use snapshots at several Reynolds numbers and displacement vectors as proposed in the conclusion of E. A. Christensen *et al.* [10].

The smx model

A model similar to the alternative model in 5.2.3 was tested in order to explore the effect of including sub-ensembles for several Reynolds numbers. This model was labeled smx. A steady snapshot for $\mathrm{Re}_{lid} = 2300$ was placed in the first block of the SPOD. The snapshot for $\mathrm{Re}_{lid} = 2540$ was placed in the second block. The third block consisted of the 68 snapshots for $\mathrm{Re}_{lid} = 2620$. Also, snapshots for the Reynolds numbers 2700, 2800, 2900 and 3000 were placed in the last four blocks. But only one mode was allowed from each of the last four blocks. The relative eigenvalue spectrum of the SPOD is shown in Fig. 5.5. At mode number 14 the relative eigenvalue is less than 10^{-11} and the decay of the eigenvalues is much less rapid than for the previous modes. However, four more modes with large eigenvalues appear at the end of the spectrum due to the last four blocks. Thus, it is expected that the performance of the low-dimensional model will degrade for some number of modes above 18 modes.

Fig. 5.6 shows the critical Reynolds number for 8-20 modes for the smx model. The

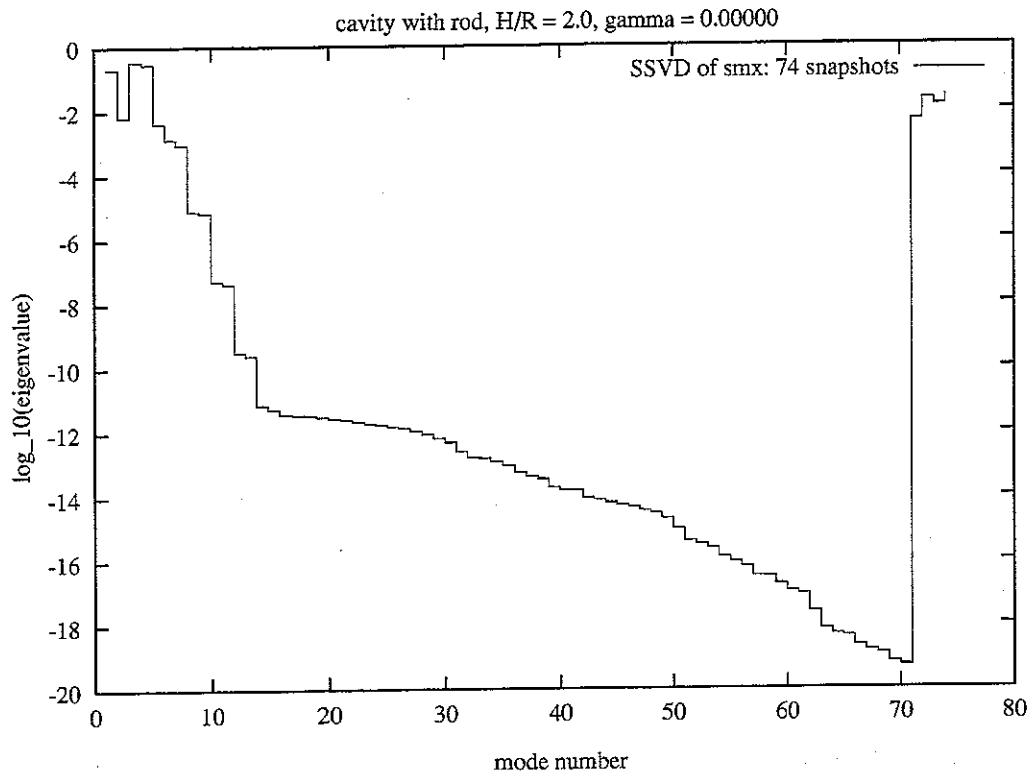

Figure 5.5: Relative eigenvalue spectrum for the SPOD of the smx data ensemble for $\gamma = 0.000$.

depicted points appear more scattered than for the skx model in Fig. 5.2. For 8-19 modes the critical Re_{lid} lies within the range 2579 – 2610. However, the deviation from the actual critical Reynolds number of 2590 is less than 1% and slightly better than for the skx model. For more than 19 modes the low-dimensional model deviates significantly from the full model. The period of the smx model shown in Fig. 5.7 lies within the range 26.29 – 26.42 for 8-19 modes. It seems that the major effect of adding sub-ensembles for several Re_{lid} further away from the critical point is that the minimum number of modes required to model the Hopf bifurcation is increased. One interpretation of this is that adding information, which is less important for the Hopf bifurcation, increases the number of modes required to represent both the Hopf bifurcation and the added information.

The sbx model

The order of the sub-ensembles of the SPOD could be important. For a sub-ensemble, only the part orthogonal to the modes of the previous sub-ensembles is represented in the modes of that sub-ensemble. By reserving the first blocks of the SPOD for the sub-ensembles of the Re_{lid} nearest to the critical Re_{lid}, these sub-ensembles can be represented without the addition of modes from any sub-ensembles for Re_{lid} further away from the critical Re_{lid}.

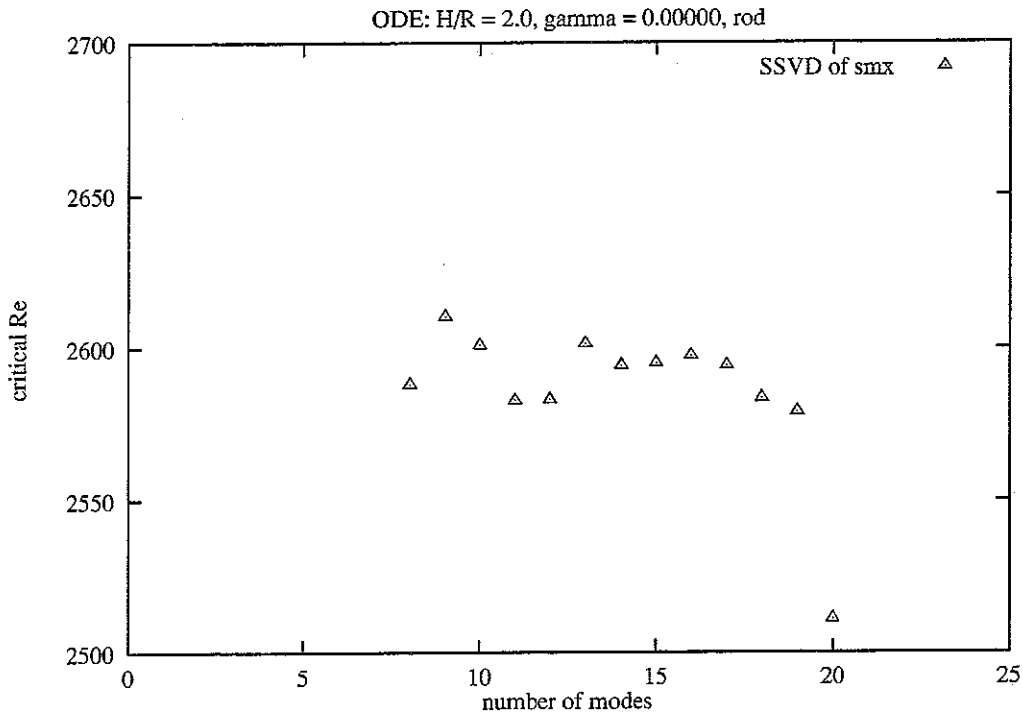

Figure 5.6: The critical Reynolds number of the smx model for $\gamma = 0.000$.

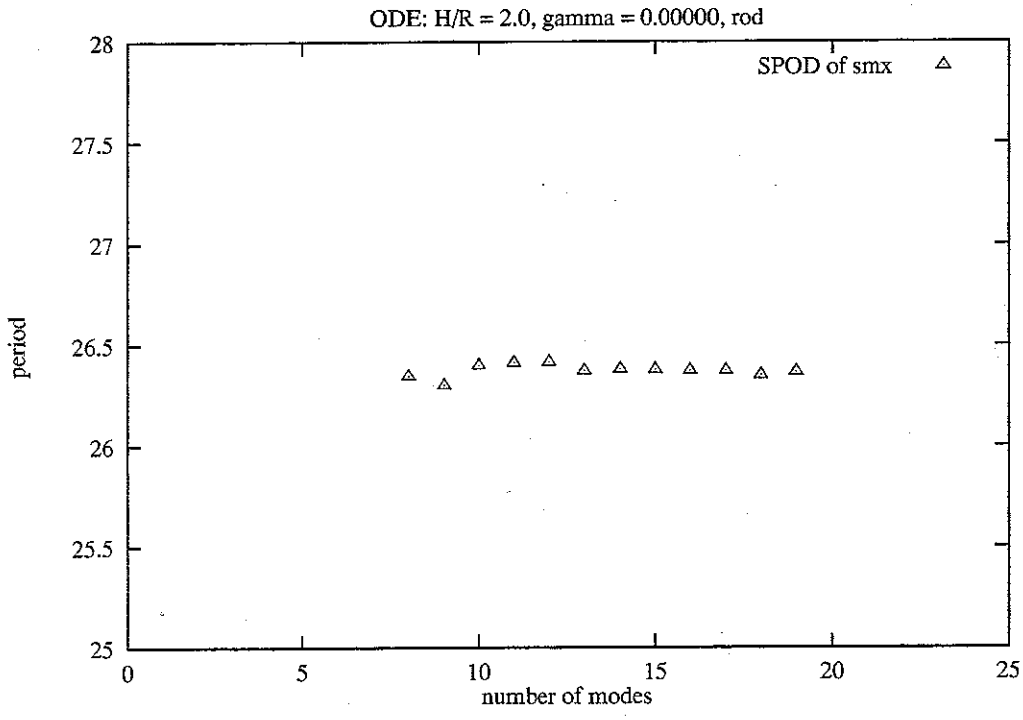

Figure 5.7: The period at the Hopf bifurcation of the smx model for $\gamma = 0.000$.

This principle was implemented in the model called sbx. The blocks of the SPOD were arranged according to the Reynolds numbers 2620, 2540, 2300, 2700, 2800, 2900, and 3000 in that order. The relative eigenvalue spectrum is shown in Fig. 5.8. At mode number 12

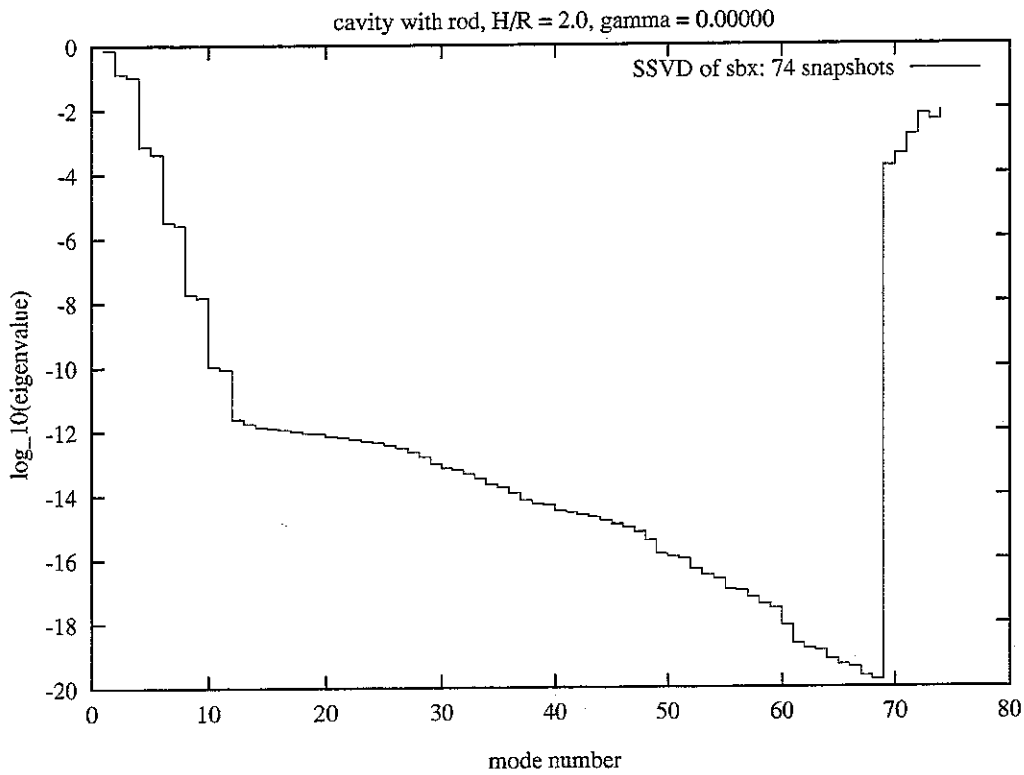

Figure 5.8: Relative eigenvalue spectrum for the SPOD of the sbx data ensemble for $\gamma = 0.000$.

the relative eigenvalue has dropped below 10^{-11} and the decay becomes slow. 6 modes with large eigenvalues appear at the end of the spectrum. For 7-18 modes the critical Reynolds number lies within the interval $2574 - 2609$ as shown in Fig. 5.9. The corresponding periods shown in Fig. 5.10 lie within the range $26.28 - 26.52$. For more than 18 modes the low-dimensional model deviates significantly from the full model. In conclusion, the sbx model does not perform better than the smx model. Thus, in this case the different order of the sub-ensembles does not seem to have any significant effect on the performance of the model.

The scx model

The effect of including several modes from each of more than one sub-ensemble was explored with the model called scx. This model is identical to the sbx model except from allowing more than one mode from the sub-ensemble corresponding to $\mathrm{Re}_{lid} = 2700$.

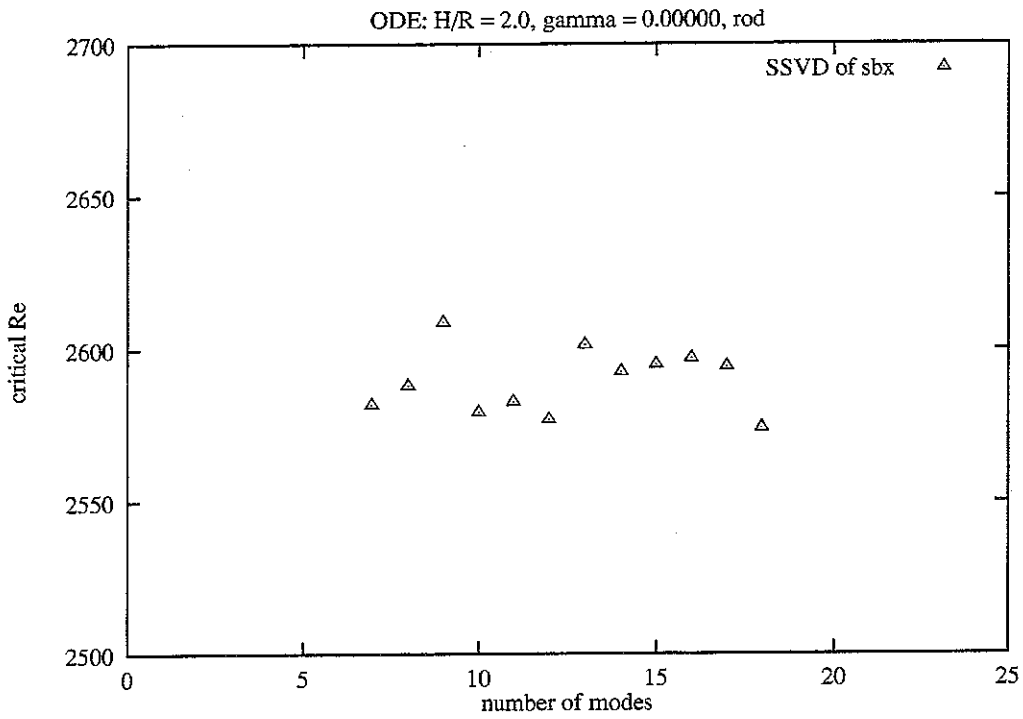

Figure 5.9: The critical Reynolds number of the sbx model for $\gamma = 0.000$.

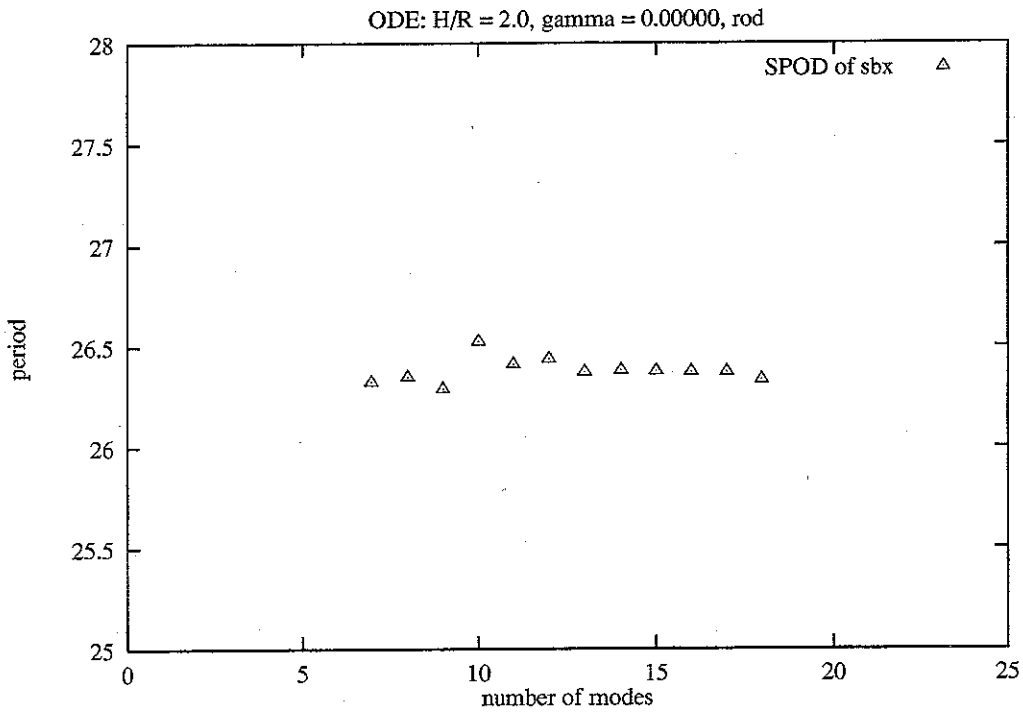

Figure 5.10: The period at the Hopf bifurcation of the sbx model for $\gamma = 0.000$.

However, the two-stage sequential POD has a tendency to include modes with smaller eigenvalues from the last blocks than from the first blocks because, in the first stage, part of the vector space spanned by the snapshots of the last blocks is represented by the first blocks and removed by orthogonalization from the last blocks in the second stage. Therefore, the first stage eigenvalues of the block corresponding to $\mathrm{Re}_{lid} = 2700$ were weighted with a factor of 10^{-3} in the mode selection procedure.

The relative eigenvalue spectrum for the SPOD with 20 modes is shown in Fig. 5.11. Although the full number of eigenvalues are shown, the eigenvalues from the second block to

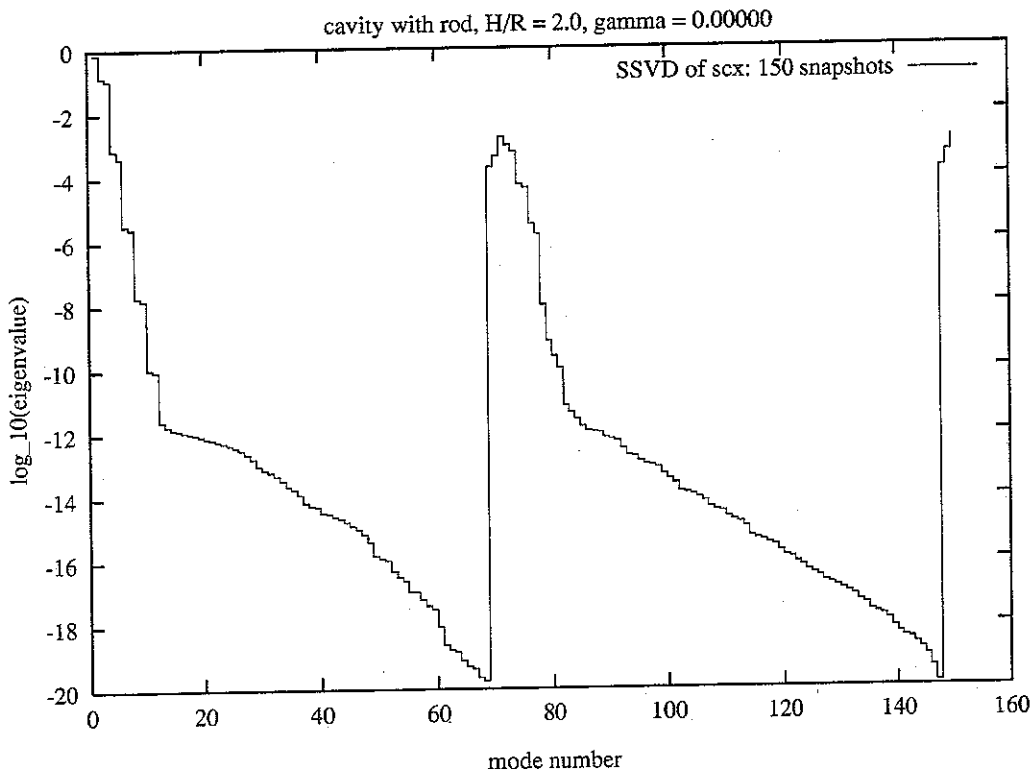

Figure 5.11: Relative eigenvalue spectrum for the SPOD of the scx data ensemble for $\gamma = 0.000$.

the last block depend on the number of modes included from each block which again depend on the total number of modes of the SPOD, i.e. 20. The eigenvalues of the first three blocks are similar to those of the first three blocks in the SPOD of the sbx model shown in Fig. 5.8. The fourth block starts at mode number 71. At mode number 82 the eigenvalues decay much slower than for the previous modes. At the end of the spectrum three large eigenvalues appear due to the last three blocks. The first block is expected to support a maximum of 12 modes. The second block and the third block support one mode each. Thus, it can be expected that the ratio between the smallest and the largest eigenvalue, that can be represented with the given ensemble of data, will be near the limit for 29 modes.

The critical Reynolds numbers for 15-30 modes are shown in Fig. 5.12. For 17-29 modes the critical Reynolds number lies within the range $2573 - 2588$ and the data points appear less scattered than for the smx and the sbx models. For 20-28 modes the critical Reynolds number lies within the range $2580 - 2588$ and the deviation from the actual value of 2590 is less than 0.4%. The period is shown in Fig. 5.13. For 17-28 modes the period lies within the range $26.40 - 26.43$ and the deviation from the value of the full model is less than 0.2%. This model allows a representation of the Hopf bifurcation which is superior to the other three models for a relatively wide range of the number of modes, i.e. for 20-28 modes. On the other hand, it requires a higher minimum number of modes to model the Hopf bifurcation.

Conclusion for the models with a fixed rod

In conclusion, for all the four low-dimensional models with a fixed rod it is not obvious how many modes should be included to satisfy the minimum number of modes required to model a Hopf bifurcation. However, the more data included from sub-ensembles corresponding to parameter values far away from the critical point the more modes are needed.

It is possible to predict an upper limit for the number of modes. For a few number of modes above this limit, all the low-dimensional models deviate significantly from the full model. For a few number of modes below this limit, all the models attain their best performance with respect to modeling a Hopf bifurcation. The upper limit is decided by the number of modes at which the eigenvalues of the SPOD decay with the number of modes at a much smaller rate than for the previous modes.

5.4 Hopf bifurcation for a counter-rotating rod

In 2.7.7 a Hopf bifurcation was found for $\gamma = -0.00400$. The critical Reynolds number was estimated to be 2630. For the full simulation with a time step of $\Delta t = 0.04$ and a 201x101 computational grid at $\mathrm{Re}_{lid} = 2650$ the period was found to be 26.46. Low-dimensional modeling was utilized to reproduce the Hopf bifurcation.

The skx model

A low-dimensional model of the Hopf bifurcation for constant $\gamma = -0.00400$, i.e. for a counter-rotating rod, was constructed for 6-19 modes. This model was called skx. The modes were based on the data ensemble consisting of a snapshot for $\mathrm{Re}_{lid} = 2550$ and 63 snapshots for $\mathrm{Re}_{lid} = 2700$. As in 5.3.1 care was taken so that the full solutions were close to the limiting state before the snapshots were sampled. Also, a whole number of periods were represented by the unsteady snapshots.

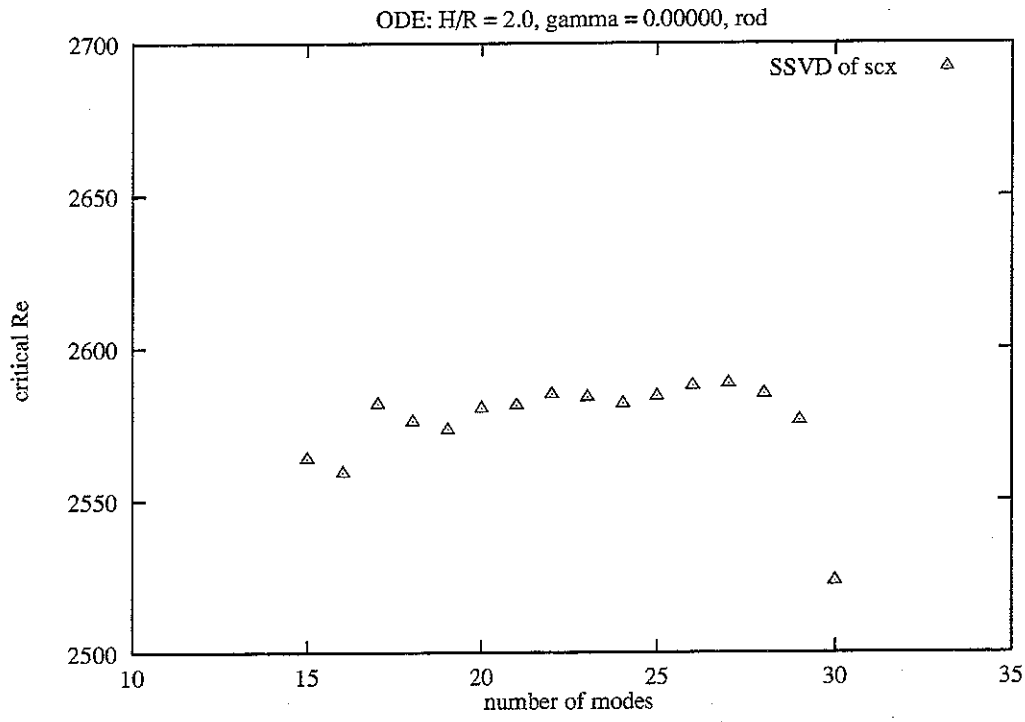

Figure 5.12: The critical Reynolds number of the scx model for $\gamma = 0.000$.

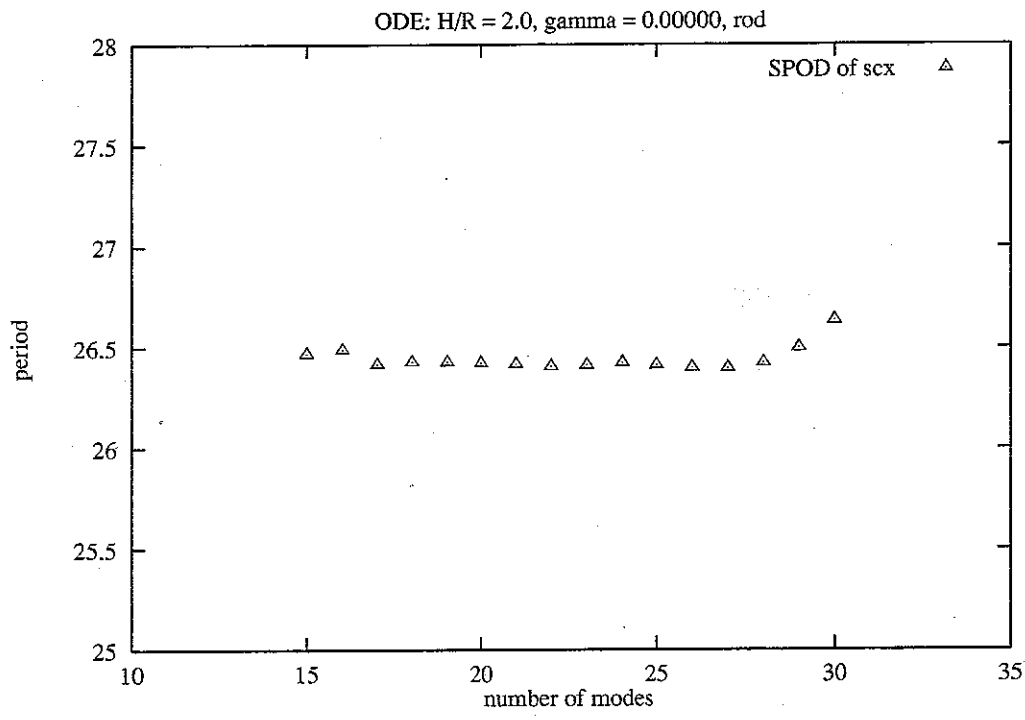

Figure 5.13: The period at the hopf bifurcation of the scx model for $\gamma = 0.000$.

The steady snapshot was placed in the first block of the SPOD and the unsteady snapshots in the second block. The resulting model was called skx. The relative eigenvalue spectrum of the SPOD is shown in Fig. 5.14. At mode number 14 the relative eigenvalue is less than

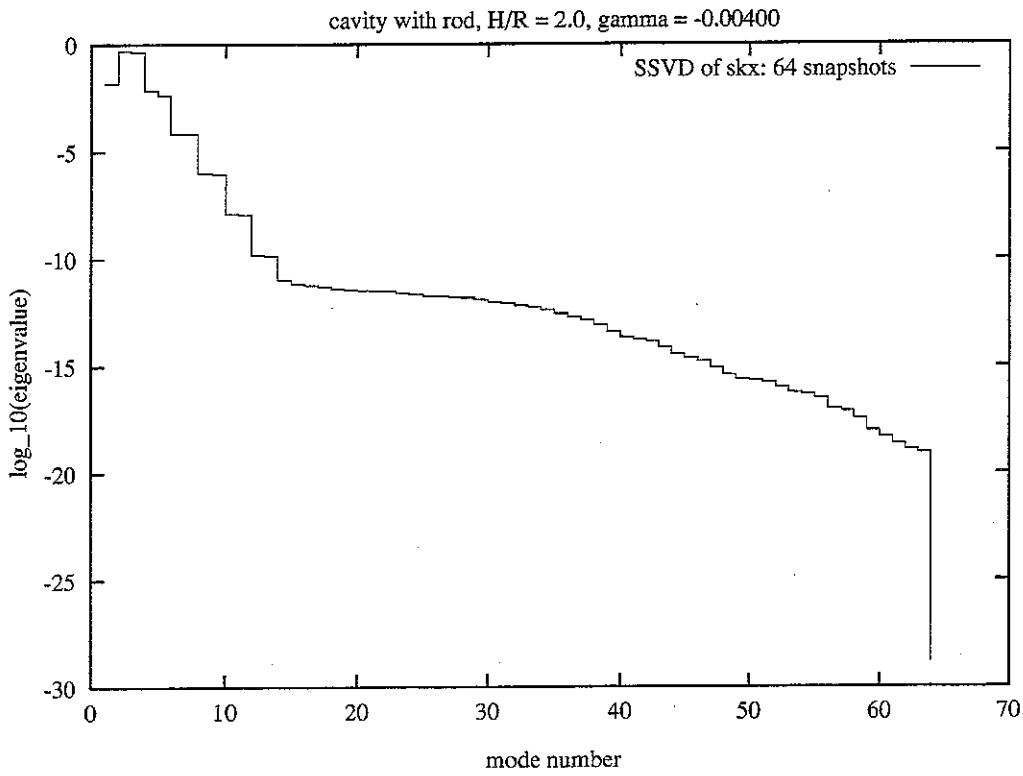

Figure 5.14: Relative eigenvalue spectrum for the SPOD of the skx data ensemble for $\gamma = -0.004$.

10^{-11} and the decay of the eigenvalues with an increasing number of modes becomes slow as compared to the previous modes. Like in 2.7.7, this indicates that the ratio between the smallest and the largest eigenvalue is near the limit that can be obtained for the given ensemble of data. As mentioned in Appendix B, the SPOD utilizing the LAPACK SVD routine can represent the eigenvalues with at least 20 decades of accuracy. Thus, the observed change in the rate of decay of the eigenvalues with increasing numbers of modes cannot be caused by inaccuracies in the decomposition method. Instead, it must be due to the properties of the data ensemble that was used for the decomposition.

In Fig. 5.15 the critical Reynolds number of the skx model is shown. For 6-15 modes the value lies within the interval $2640 - 2662$. The deviation from the full model is less than 1.3%. For more than 16 modes the low-dimensional model deviates significantly from the full model. The period is shown in Fig. 5.16. For 6-15 modes the period lies within the interval $26.40 - 26.59$. The deviation from the full model is less than 0.5%.

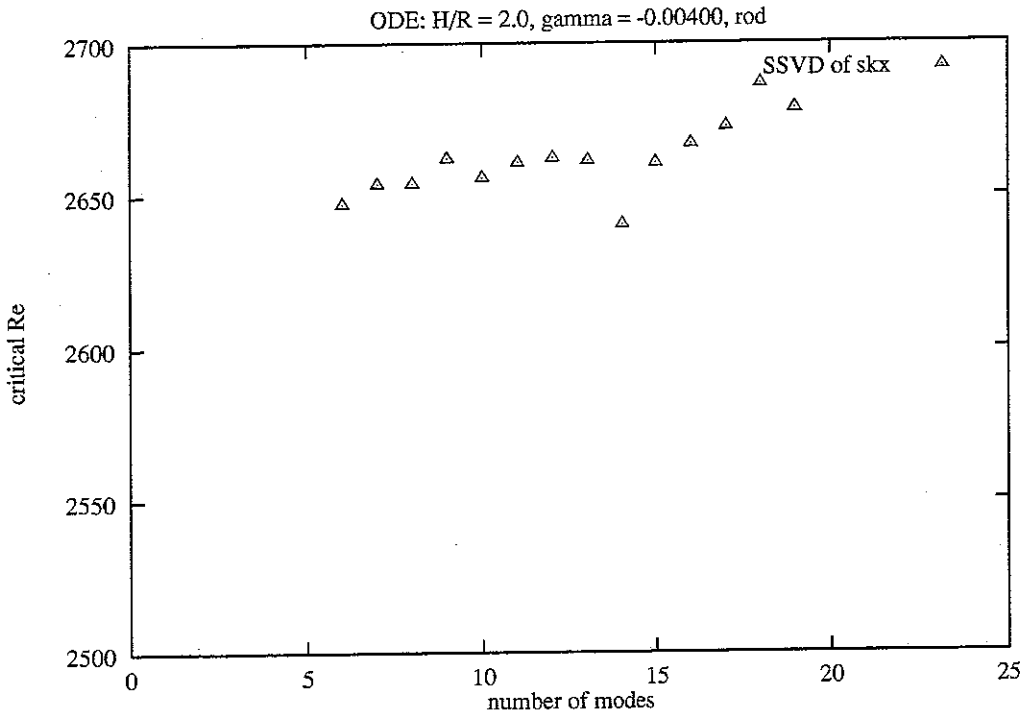

Figure 5.15: The critical Reynolds number of the skx model for $\gamma = -0.004$.

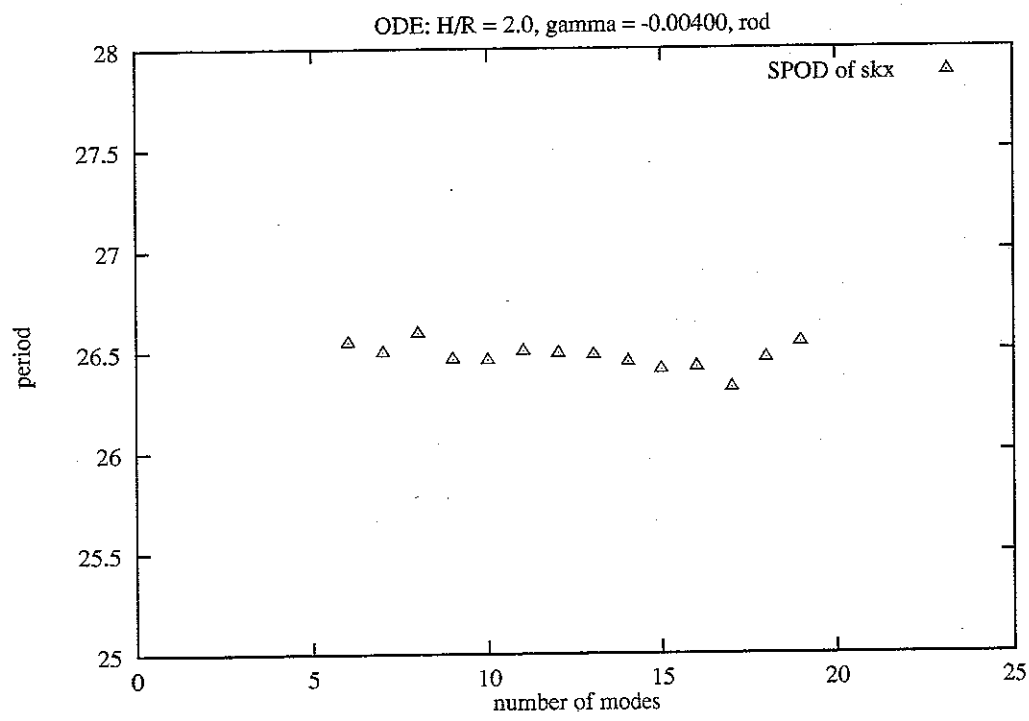

Figure 5.16: The period at the Hopf bifurcation of the skx model for $\gamma = -0.004$.

Conclusion for the model with a counter-rotating rod

A working low-dimensional model of a Hopf bifurcation can be constructed for a fixed non-zero γ. This is interesting because the flow configured with a rotating rod is different from the flow in the cavity without a rod whereas the behavior of the flow with a fixed rod is nearly identical to the flow without a rod. However, it was expected that the low-dimensional model should work, because the boundary condition of the rod is similar to the other boundary conditions, and because for a fixed γ the inhomogeneous boundary conditions for the azimuthal velocity are contained by the mean field like for the low-dimensional models of the flow in the cavity without a rod.

5.5 Modeling a Hopf bifurcation for a constant Reynolds number

5.5.1 Satisfying the boundary conditions of azimuthal velocity

A low-dimensional model, for which γ is allowed to vary, is fundamentally different from the previously presented models. Although the Reynolds number is constant, the fact that the data ensemble, which is used for the decomposition, contains snapshots for different values of γ implies that the azimuthal velocity becomes non-zero on a part of the boundary of the modes. In the previous models, subtracting the ensemble mean field from all the snapshots ensured that all the modes contained only zero azimuthal velocity on the boundary. A low-dimensional model, for which γ is allowed to vary, must be able to maintain a balance among the modes for which the boundary conditions of the azimuthal velocity is satisfied by the reconstructed flow field. This feature is needed to construct a low-dimensional model in which γ and Re_{lid} are both free parameters.

It is reasonable to expect that the performance of low-dimensional models with a varying γ is comparable to the performance of the previous models, because a linear combination of the modes, for which the boundary conditions of the azimuthal velocity diverge from the boundary conditions enforced in the model, would produce escalating terms in the part of the projected equations corresponding to diffusion. However, The author has not been able to locate any references to this issue in the literature.

5.5.2 Hopf bifurcation for $\mathrm{Re}_{lid} = 2550$

In 2.7.8 a Hopf bifurcation was found for $\mathrm{Re}_{lid} = 2550$. The critical γ was estimated to be 0.00366. For the full simulation with a time step of $\Delta t = 0.04$ and a 201x101 computational grid at $\gamma = 0.00400$ the period was found to be 26.47. In the current study, it was attempted to

reproduce the Hopf bifurcation by simple low-dimensional models. The models were analyzed with AUTO 97 in order to find the critical Reynolds number and the period.

The hopfy model

A low-dimensional model of the Hopf bifurcation for constant $\mathrm{Re}_{lid} = 2550$ was constructed for 4-10 modes. This model was called hopfy. The modes were based on the data ensemble consisting of a snapshot for $\gamma = 0.000$, which was placed in the first block of the SPOD, a snapshot for $\gamma = 0.002$, which was placed in the second block, and 65 snapshots for $\gamma = 0.004$ which were placed in the third block.

As for the data used to construct the previous low-dimensional models, care was taken so that the full solutions were close to the limiting state before the snapshots were sampled. Also, close to a whole number of periods were represented by the snapshots of the periodic flow.

The SPOD utilized the LAPACK SVD routine mentioned in Appendix B. The relative eigenvalue spectrum of the SPOD is shown in Fig. 5.17. At mode number 10 the relative

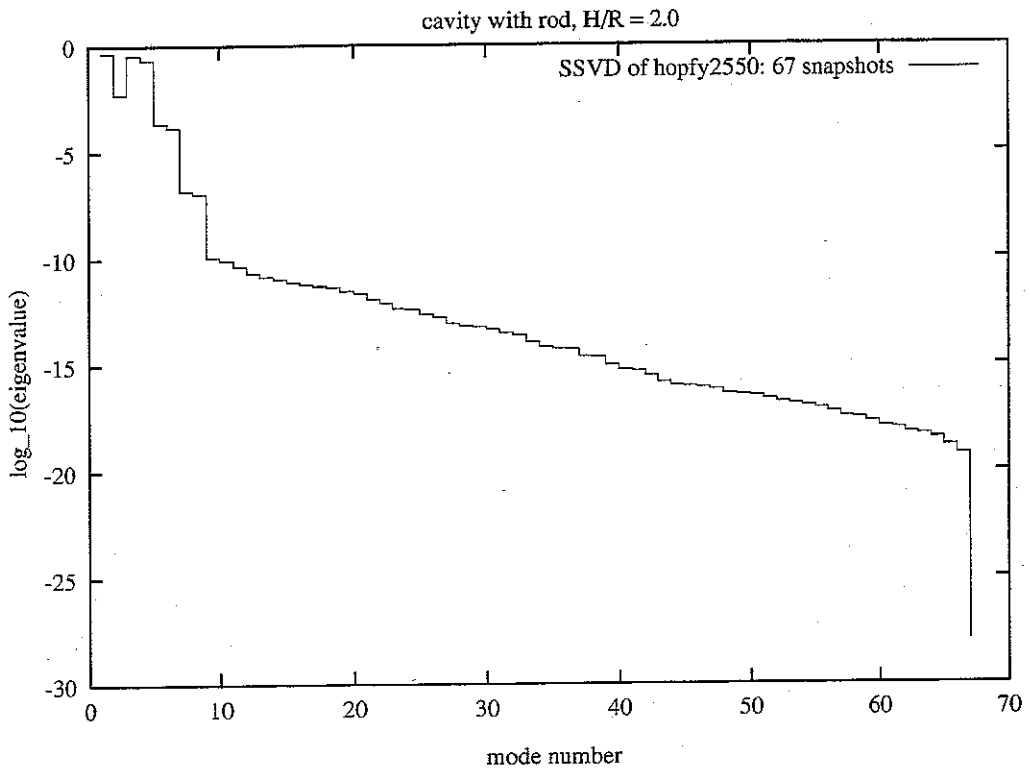

Figure 5.17: Relative eigenvalue spectrum for the SPOD of the hopfy data ensemble for $\mathrm{Re}_{lid} = 2550$.

eigenvalue is less than 10^{-10} and the decay of the eigenvalues with an increasing number of modes becomes slow as compared to the previous modes. Like in 2.7.7, this indicates that the

ratio between the smallest and the largest eigenvalue is near the limit that can be obtained for the given ensemble of data. Thus, it is expected that the low-dimensional model diverges significantly from the full model for a number of modes above 10.

The hopfy model was analyzed with AUTO 97 in order to find the critical γ and the period. An example of the graphical output from AUTO 97 is shown for 5 modes in Fig. 5.20. The horizontal axis represents the Reynolds number and the vertical axis represents an L_2-norm used by AUTO 97. The diagram shows a steady solution. The full line represents a stable solution and the filled square indicates a Hopf bifurcation. The dashed line represents an unsteady solution or a solution for which stability is unknown. The actual Hopf bifurcation is shown by the filled square at the bottom of the curve for $\gamma = 0.00399$. An unstable steady solution exists for γ greater than the critical value. The hopf bifurcation of the of the unstable steady solution indicated at the upper right part of the curve is a numerical artifact. No bifurcation to a stable steady solution of the full model has been detected for such a large γ-value. However, it is detected far away from the range of γ-values represented by snapshots used for the construction of the low-dimensional model.

In Fig. 5.18 the critical γ of the hopfy model is shown. For 4-10 modes the value lies within the interval $0.00395 - 0.00398$. The deviation from the full model is less than 9%. For more than 10 modes the low-dimensional model deviates significantly from the full model. However, this was expected. The period is shown in Fig. 5.19. For 4-10 modes the period lies within the interval $26.37 - 26.41$. The deviation from the full model is less than 0.4%.

Comparing the performance of the low-dimensional model to the previous models it is remarkable that, although the deviation from the full model is an order of magnitude greater for the critical value of the controlling parameter, the deviation of the period is of a similar order of magnitude.

As mentioned in 5.5.1, the hopfy model is fundamentally different from the previously presented models. As the data ensemble, which is used for the decomposition, contains snapshots for different values of γ, it is implied that the azimuthal velocity becomes non-zero on a part of the boundary of the modes. This feature is in contrast to the previous models in which subtraction the ensemble mean field from all the snapshots ensured that all the modes contained only zero azimuthal velocity on the boundary.

Apparently, the hopfy model, which allows γ to vary, is able to maintain a balance among the modes such that the boundary conditions of the azimuthal velocity is satisfied by the reconstructed flow field. If the difference between the enforced boundary conditions of the low-dimensional model and the boundary conditions of the linear combination of modes yielding the reconstructed flow field was diverging, the model would not be able to function.

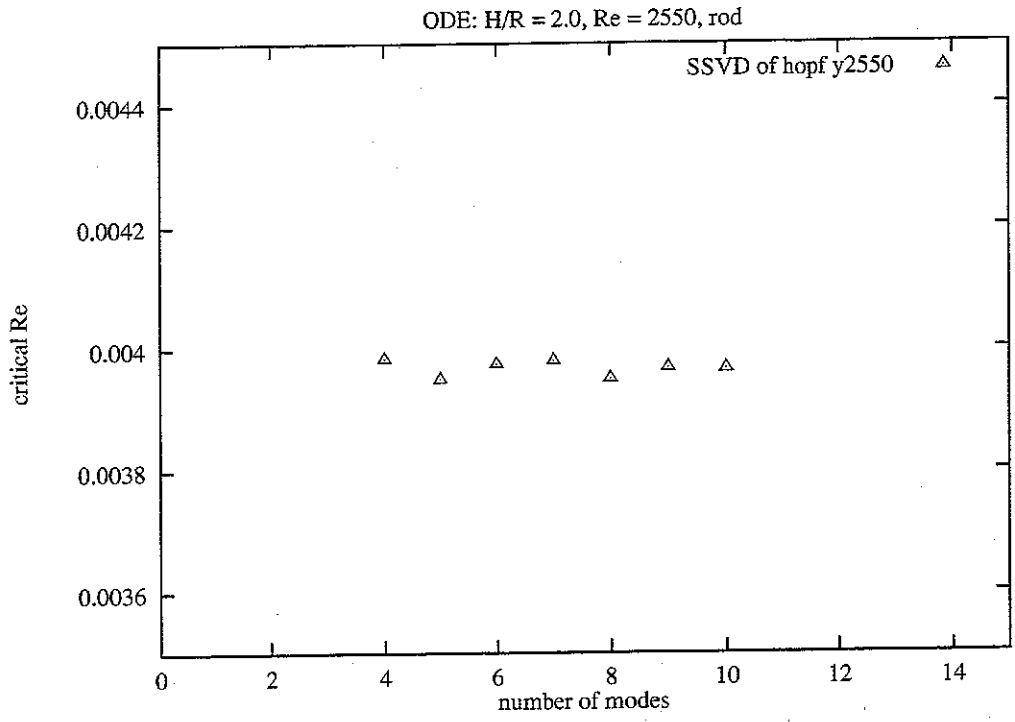

Figure 5.18: The critical γ of the hopfy model for $\mathrm{Re}_{lid} = 2550$.

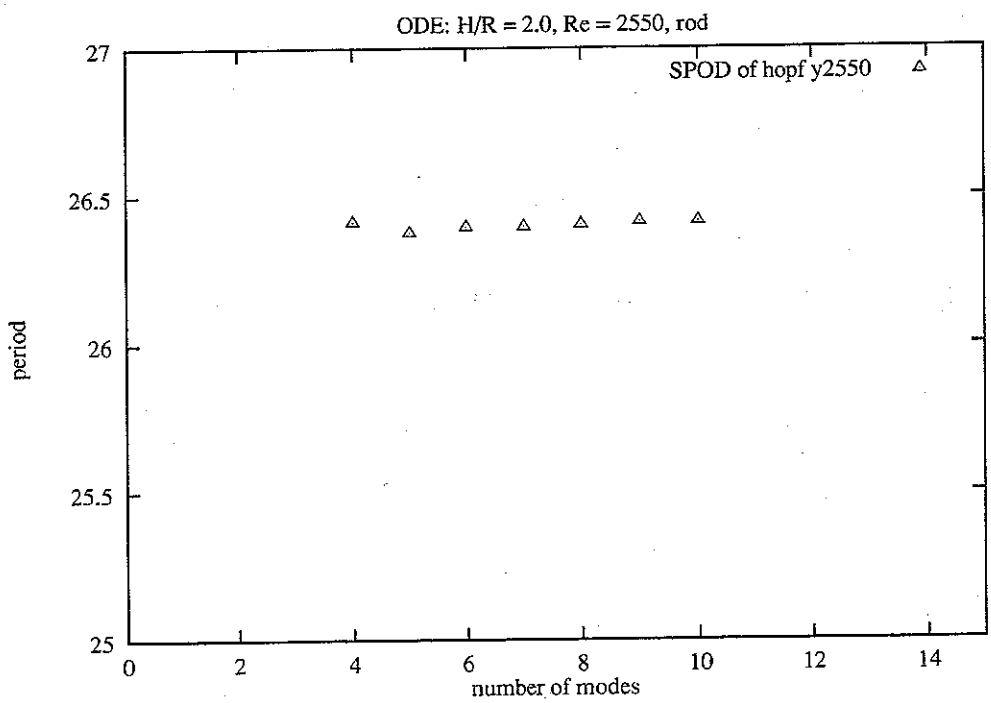

Figure 5.19: The period at the Hopf bifurcation of the hopfy model for $\mathrm{Re}_{lid} = 2550$.

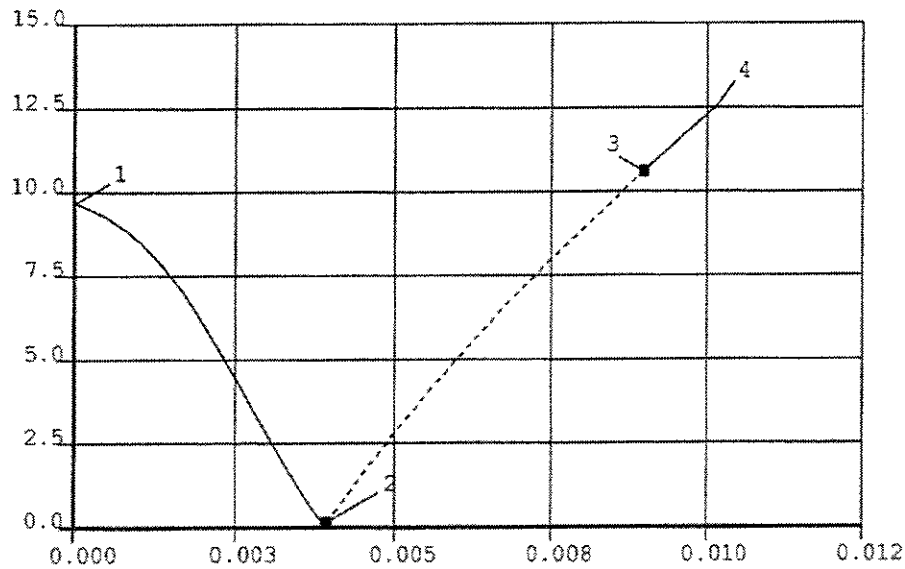

Figure 5.20: Graphical output from AUTO 97 of the steady solution of the hopfy model with 5 modes for $\mathrm{Re}_{lid} = 2550$. The horizontal axis represents γ and the vertical axis represents an L_2-norm used by AUTO 97.

The hopfx model

An alternative low-dimensional model of the Hopf bifurcation for constant $\mathrm{Re}_{lid} = 2550$ was constructed for 4-10 modes. This model was called hopfx. The modes were based on the data ensemble consisting of a snapshot for $\gamma = 0.002$, which was placed in the first block of the SPOD, and 65 snapshots for $\gamma = 0.004$ which were placed in the second block. In contrast to the hopfy model, only one snapshot was provided in the hopfx model for representing the steady region of the parameter space.

An example of the graphical output from AUTO 97 is shown for 5 modes in Fig. 5.21. The horizontal axis represents the Reynolds number and the vertical axis represents an L_2-norm used by AUTO 97. The diagram shows a steady solution. The full line represents a stable solution and the filled square indicates a Hopf bifurcation. The dashed line represents an unsteady solution or a solution for which stability is unknown.

The actual Hopf bifurcation is shown by the filled square at the bottom of the curve for $\gamma = 0.00399$. An unstable steady solution exists for γ greater than the critical value. A fold bifurcation named "3" is shown very close to the Hopf bifurcation. Although it is not known if a fold bifurcation of the unstable steady solution exists, the fold bifurcation contained by the hopfx model is located for a γ-value so close the the critical γ of the Hopf bifurcation, that it was difficult to utilize AUTO 97 for detecting the Hopf bifurcation.

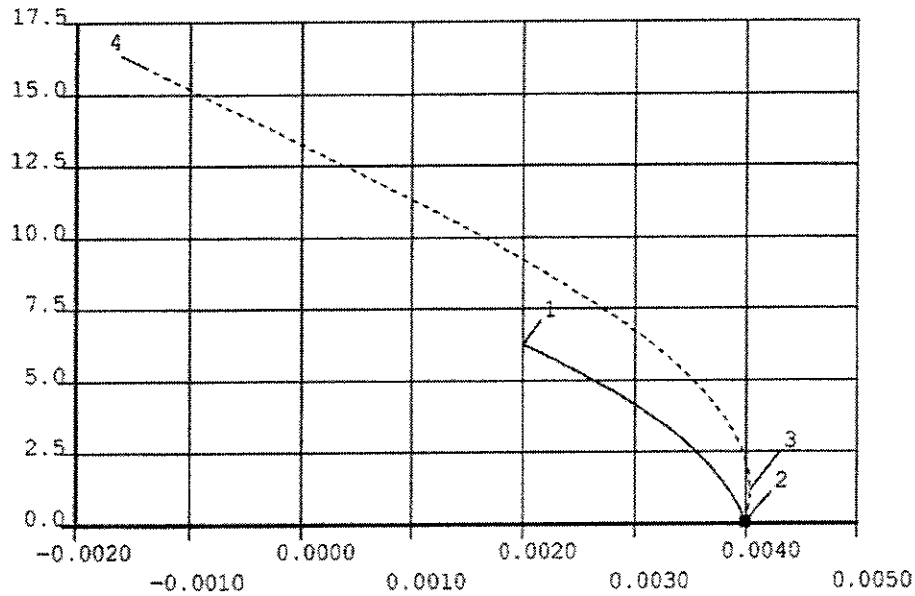

Figure 5.21: Graphical output from AUTO 97 of the steady solution of the hopfx model with 5 modes for $\mathrm{Re}_{lid} = 2550$. The horizontal axis represents γ and the vertical axis represents an L_2-norm used by AUTO 97.

The fold bifurcation located very close to the Hopf bifurcation was a common feature for the hopfx model with a number of modes in the range 4-10. Therefore, despite the prediction of critical values of γ within the range $0.00399 - 0.00400$ and a period with an accuracy comparable to the hopfy model, the hopfx model should be considered unreliable. For more than 10 modes the model deviated significantly from the full model.

Conclusion for the models with a constant Reynolds number

It can be concluded for the models with a constant Reynolds number that it is possible to construct a simple working model for which γ is allowed to vary. However, in contrast to the models of a constant γ, it may be necessary to include at least one additional sub-ensemble for a parameter value within the range of the parameter space corresponding to a steady limiting flow. The alternative possibility of including additional modes derived from sub-ensembles corresponding unsteady limiting flows has not been discussed.

This type of low-dimensional models is fundamentally different from the models with constant γ and the models with only one parameter. As the data ensemble, which is used for the decomposition, contains snapshots for different values of γ, it is implied that the azimuthal velocity becomes non-zero on a part of the boundary of the modes. This feature is in contrast to the models in which subtraction the ensemble mean field from all the snapshots ensures that all the modes have zero azimuthal velocity on the boundary. Thus, an important demon-

block	Re_{lid}	γ	snapshots	weight
1	2500	0.00000	1	1.0
	2550	0.00000	1	1.0
2	2500	0.00200	1	1.0
	2550	0.00200	1	1.0
3	2500	0.00400	1	1.0
4	2550	0.00400	65	1.0
5	2600	0.00000	59	0.1
6	2600	0.00200	59	0.01
7	2600	0.00400	79	0.001

Table 5.1: Blocks of the SPOD used to construct the h1 model.

stration has been performed which indicates that it is possible to construct low-dimensional models with more than one free parameter.

5.6 Continuation of a Hopf bifurcation

Within the parameter space, the region of the unsteady limiting flow is divided from the region of the steady limiting flow by a critical curve. For the region of the parameter space included in Fig. 2.7, the unsteady limiting flow is periodic within a substantial part of the unsteady region located near the steady region. The upper part of the critical curve consists of points, each of which is the critical point of a Hopf bifurcation. This part of the critical curve can be reproduced by low-dimensional models and detected via Hopf continuation. The task of Hopf continuation can be performed by AUTO 97.

A low-dimensional model used for Hopf continuation must be operational with two varying parameters. As far as the author knows, there have been no previous reports in the literature of such models based on projection on orthogonal modes which are calculated by decomposition techniques. Within this context, a new issue is introduced - how should the ensemble data used for the decomposition be located in the two-dimensional parameter space? Also, when utilizing the SPOD for the decomposition, the additional complication of the order of the sub-ensembles needs to be considered.

5.6.1 A two-parameter low-dimensional model

An ensemble of data consisting of the sub-ensembles defined in Table 5.1 was used to construct a two-parameter low-dimensional model called h1. For each parameter combination, the

corresponding sub-ensemble was assigned to a numbered block of the SPOD. Also, the number of snapshots contained by each sub-ensemble is shown in Table 5.1. The sub-ensembles of an unsteady limiting flow each contain more than one snapshot. The sub-ensembles of a steady limiting flow only contain one snapshot each. The blocks containing the unsteady sub-ensembles were kept as small as possible in order to obtain a high numerical accuracy by enabling the use of the LAPACK SVD routine for as many of the blocks as possible. On the other hand, some of the steady sub-ensembles were assigned to the same block. Hence, a smaller number of blocks is obtained. As this requires fewer orthogonalizations in the second stage of the SPOD, the numerical accuracy is increased. In order prevent the SPOD from selecting modes with poor accuracy from the last blocks, the first stage eigenvalues of last three blocks were weighted in the mode selection procedure before the second stage of the SPOD. The resulting relative eigenvalue spectrum for 40 modes is shown in Fig. 5.22. Within

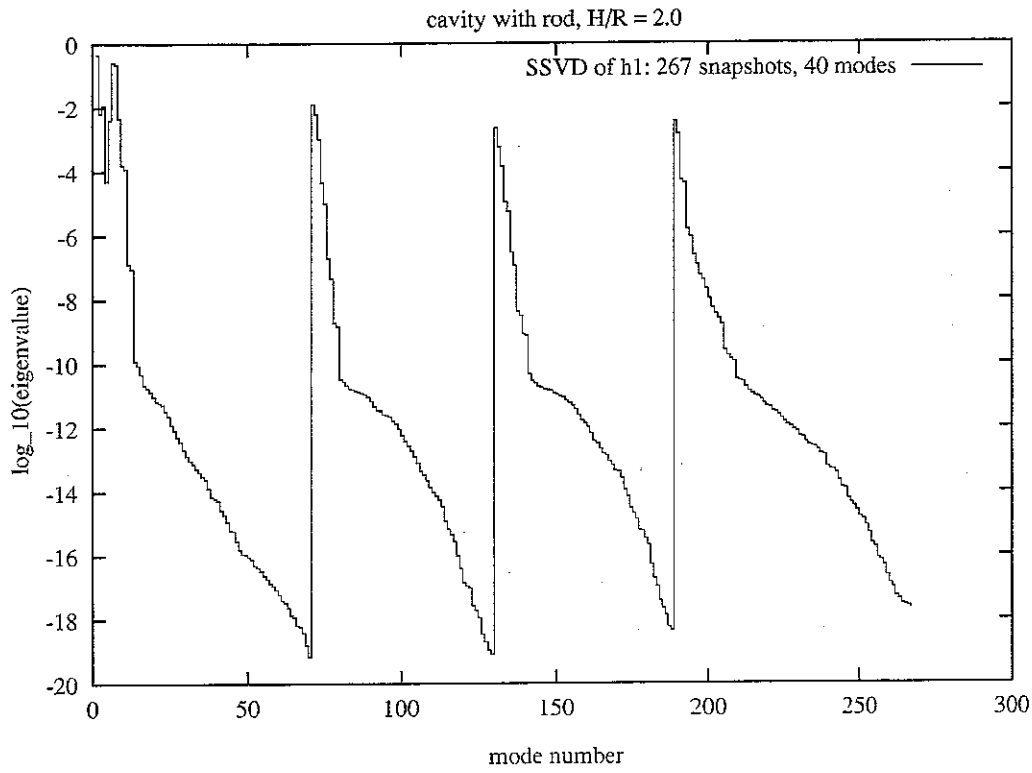

Figure 5.22: Relative eigenvalue spectrum for the SPOD of the data ensemble used for the h1 model.

each of the unsteady blocks, the relative eigenvalues decay slow compared to the previous modes after reaching a level below 10^{-10}. The blocks 4, 5, 6 and 7 of the SPOD yielded 7, 9, 9 and 10 modes respectively. The relative eigenvalues of the calculated modes were all above 10^{-10}. Thus, a high degree of numerical accuracy is expected for all of the modes used in the h1 model.

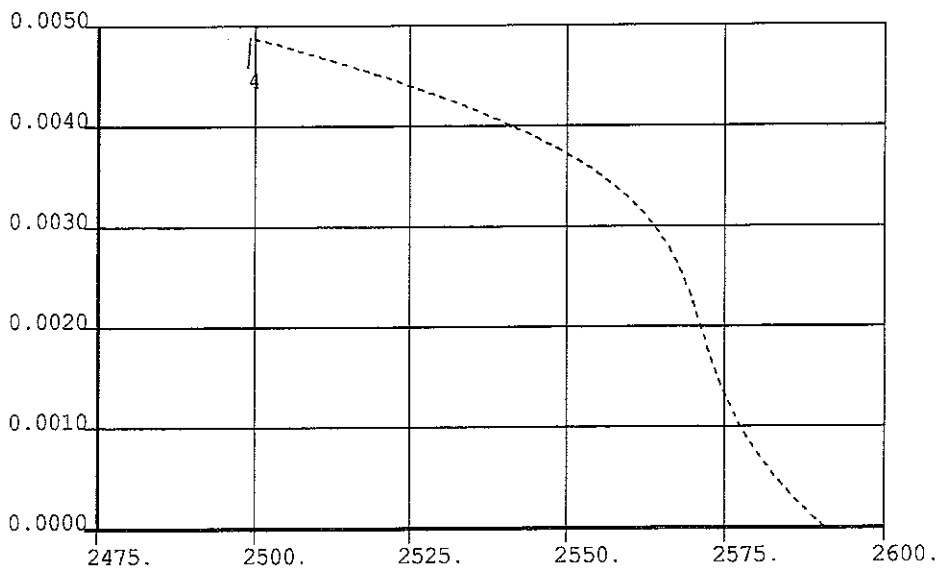

Figure 5.23: Graphical output from AUTO 97 of the critical curve found via Hopf continuation of the h1 model with 40 modes. The horizontal axis represents the Reynolds number and the vertical axis represents γ.

The SPOD of the h1 ensemble was calculated for 23-40 modes. Each set of modes was used to construct a low-dimensional model as explained in Chapter 4.

In order to use AUTO 97 for Hopf continuation, a Hopf bifurcation needs to be located on a steady solution for a varying parameter, which is called the primary parameter, and a constant parameter called the secondary parameter. For the h1 model, Re_{lid} was chosen as the primary parameter and γ was chosen as the secondary parameter. For the calculation of the steady solution, a γ-value of 0.0 was chosen.

The critical point of the Hopf bifurcation is used as a starting point for the Hopf continuation in which both of the parameters are allowed to vary. During the Hopf continuation, the period and the secondary parameter are recorded as a function of the primary parameter. AUTO 97 is capable of detecting fold bifurcations on the critical curve. Furthermore, the parameters can be recorded for specific values of both of the parameters. This was used to record the γ of the critical curve for $\mathrm{Re}_{lid} = 2550$.

As an example, the critical curve for 40 modes is shown in Fig. 5.23. The starting point of the curve is located at the right hand side of the diagram for $\gamma = 0.0$. The corresponding Reynolds number was calculated to be 2591. The curve proceeds in an S-shaped form towards smaller Reynolds numbers and larger values of γ until the end-point at $\mathrm{Re}_{lid} = 2500$ where the calculation was stopped.

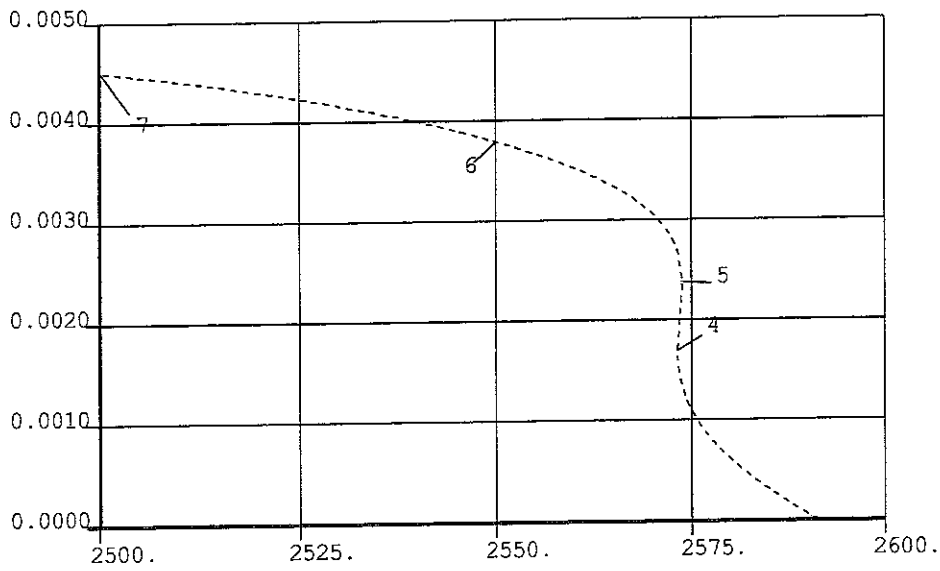

Figure 5.24: Graphical output from AUTO 97 of the critical curve found via Hopf continuation of the h1 model with 30 modes. The horizontal axis represents the Reynolds number and the vertical axis represents γ.

The part of the curve above $\gamma = 0.004$ can be considered as an extrapolation because it does not lie in between any values of γ represented in the data ensemble used for the construction of the h1 model As can be seen from Fig. 2.7, the Hopf bifurcation for $\mathrm{Re}_{lid} = 2500$ occurs for a γ-value in the range $0.00525 - 0.00550$ whereas the value predicted by the h1 model with 40 modes is 0.00488. Thus the h1 model is able to perform predictions outside its valid range of parameters, although these predictions are not very accurate.

For the h1 models with 32, 33, 34 and 36 modes, fold bifurcations appeared on the critical curve. The models with 32-36 modes were discarded because of the fold bifurcations. Also, the models with less than 25 modes had critical curves with fold bifurcations and were discarded. The critical curve of the h1 model with 33 modes is shown in Fig. 5.24. The fold bifurcations have been assigned the labels "4" and "5". The label "6" is not a bifurcation but it denotes a point for which the parameters are recorded.

In order to obtain a quantitative measure of the deviation from the true critical curve of the modeled critical curves, the critical Reynolds number for $\gamma = 0.0$ and the critical γ for $\mathrm{Re}_{lid} = 2550$ were plotted versus the number of modes. Also, the period was plotted.

Fig. 5.25 depicts the critical Re_{lid} for $\gamma = 0.0$. For 25-31 modes, critical Re_{lid} within the range $2591 - 2592$ are obtained. The deviation from the actual value of 2590 is less than 0.08%. For 37-40 modes, a critical Re_{lid} of 2591 is obtained. The deviation from the actual value is less than 0.04%.

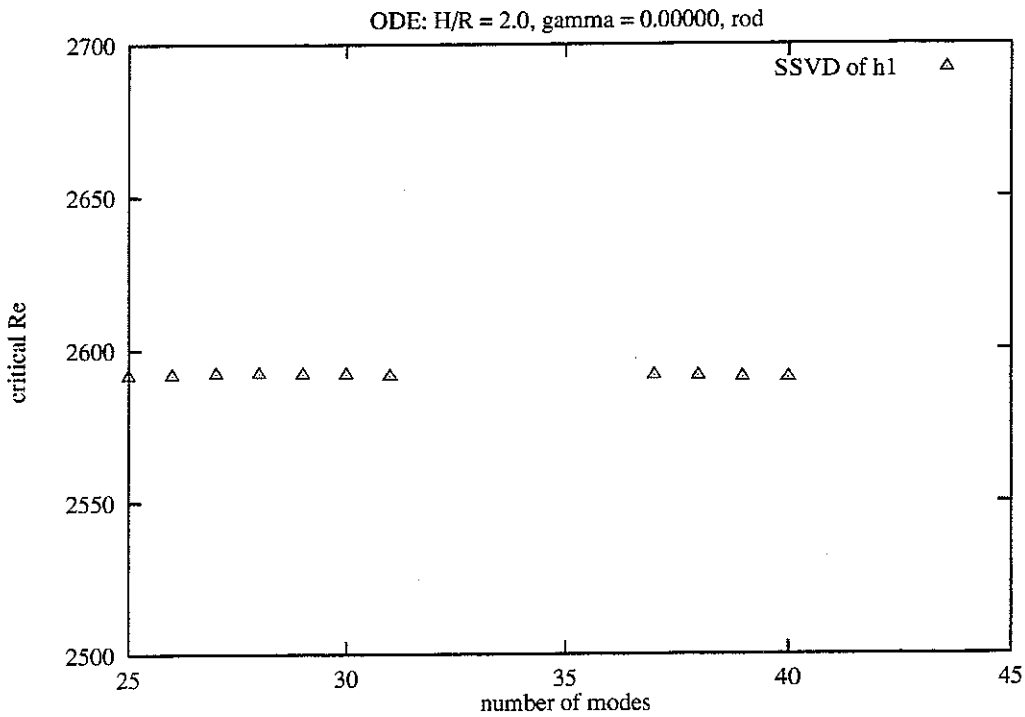

Figure 5.25: The critical Reynolds number of the h1 model for $\gamma = 0.000$.

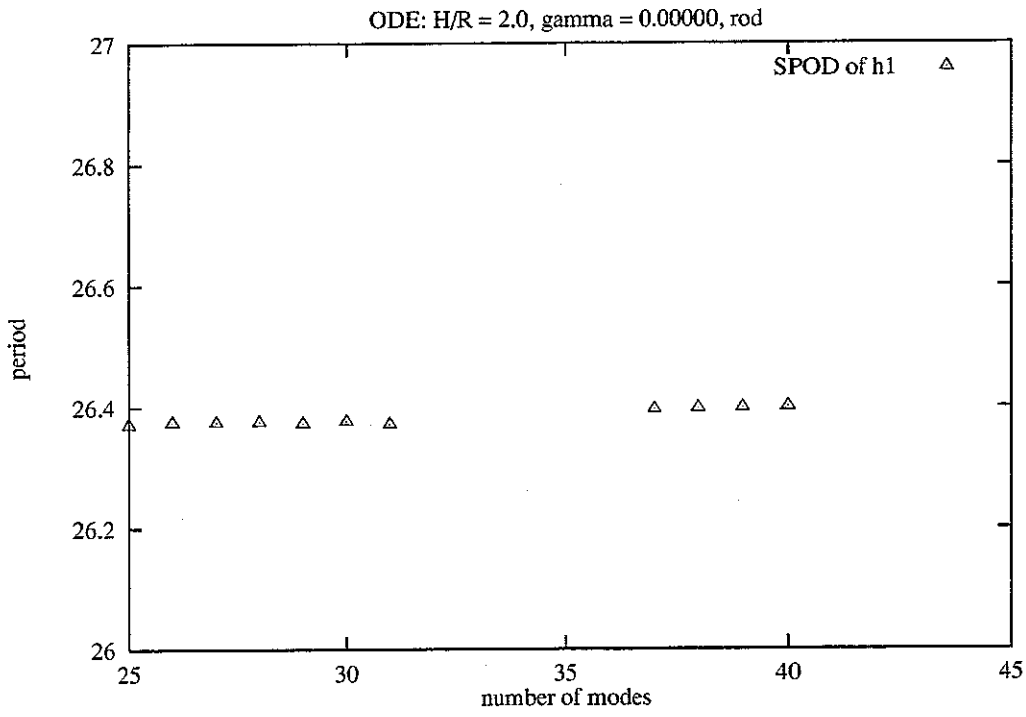

Figure 5.26: The period on the critical curve of the h1 model for $\gamma = 0.000$.

The period shown in Fig. 5.26 lies within the range $26.37 - 26.38$ for 25-31 modes. The deviation from the actual value of 26.44 is less than 0.3%. For 37-40 modes the period is 26.40 which deviates less than 0.2% from the actual value.

For the h1 model, both the critical Reynolds number and the period of the Hopf bifurcation for $\gamma = 0.0$ compare excellently to the results obtained for the simpler models presented in 5.3.1.

Fig. 5.27 depicts the critical γ for $\mathrm{Re}_{lid} = 2550$. For 25-31 modes, the critical γ lies within the range $0.00365 - 0.00378$. The deviation from the actual value of 0.00366 is less than 4%. For 37-40 modes, the critical γ lies within the range $0.00373 - 0.00382$, for which the deviation from the actual value is less than 4%. The period shown in Fig. 5.28 lies within the range $26.36 - 26.39$ for 25-31 modes. The deviation from the actual value of 26.47 is less than 0.5%. For 37-40 modes the period lies within the range $26.40 - 26.42$ which deviates less than 0.2% from the actual value.

Both the critical γ and the period of the Hopf bifurcation for $\mathrm{Re}_{lid} = 2550$ compare favorably to the results obtained for the simpler models presented in 5.5.2.

Since the h1 models with 32-36 modes were discarded, the following question is raised - is it the models with 25-31 modes or the models with 37-40 modes which are reliable, and which is the set of models which might be working by a mere chance? It is not considered acceptable to have occurrences of spurious malfunctioning models for certain numbers of modes within the range between the minimum number of modes required to model the Hopf bifurcation and the maximum limit estimated for the current ensemble of data used for the construction of the low-dimensional model.

The eigenvalue spectrum shown in Fig. 5.22 indicates that the h1 model should be capable of supporting a number of modes greater than 40. Also, Fig. 5.25 and in particular Fig. 5.27 indicate that the modeled critical curve approaches the true critical curve for an increased number of modes within the interval 37-40. Unfortunately, due to the large memory requirements of AUTO 97, it was not possible to analyze the low-dimensional models for more than 40 modes. However, it is very likely that the h1 model performs well for more than 40 modes. Therefore, it is believed that the minimum number of modes required for the h1 model is at least 37 and not 25. Furthermore, the maximum number of modes must be greater than 40 and not 31.

Probably, a better model than the h1 model can be constructed to yield the section of the critical curve in question. For instance, the sub-ensembles of data used for the model could have been arranged differently. Also, different weighting factors could have been applied for the SPOD blocks, and various maximum limits of the number of modes from each block could have been defined. These options were not investigated further.

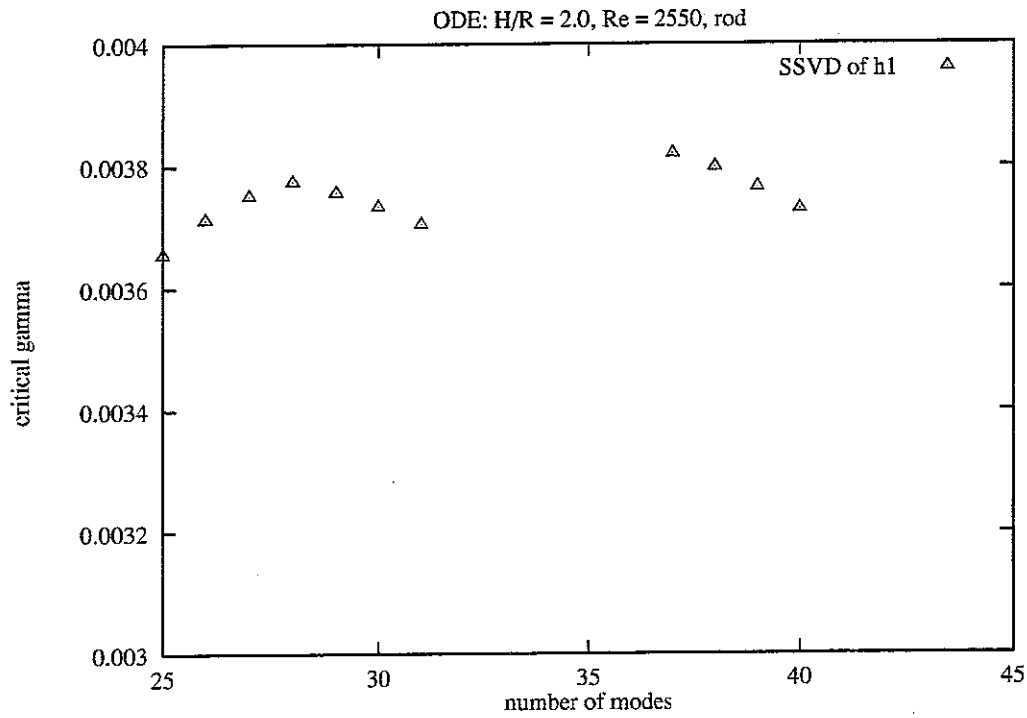

Figure 5.27: The critical γ of the h1 model for $\mathrm{Re}_{lid} = 2550$.

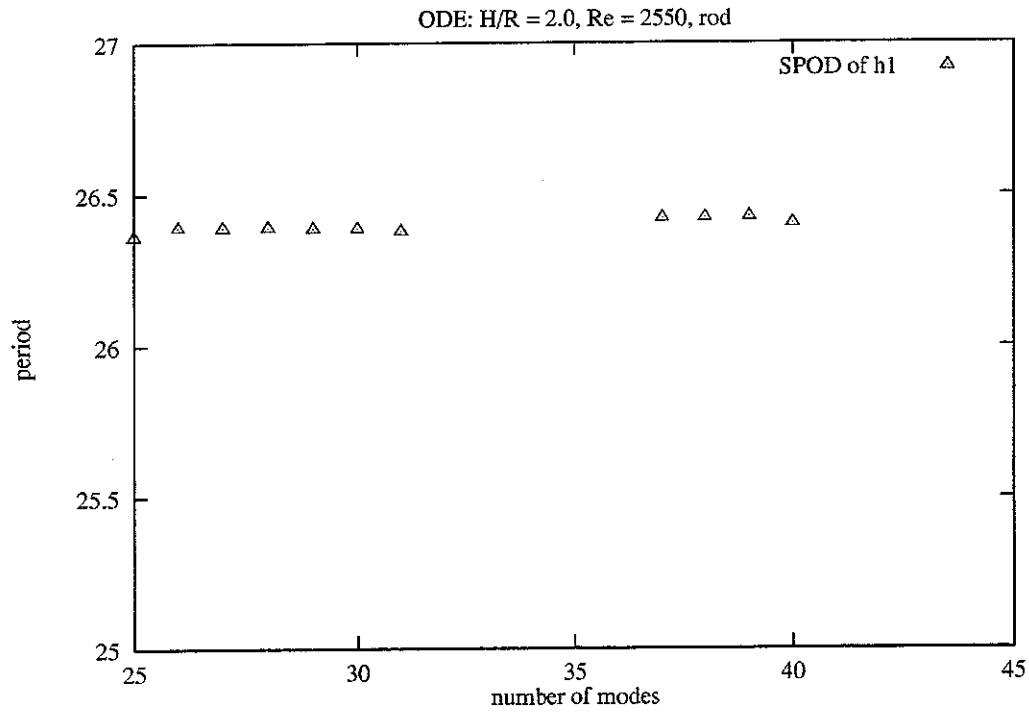

Figure 5.28: The period on the critical curve of the h1 model for $\mathrm{Re}_{lid} = 2550$.

The accuracy of the critical values predicted by the h1 model for one constant parameter is remarkable compared to the earlier results obtained for the simpler models in 5.3.1 and 5.5.2. This could provide a clue of how to provide the data used to build low-dimensional models. When considering the data ensemble used for the construction of a low-dimensional model for which a high degree of accuracy is desired, it may be beneficial to include sub-ensembles of data for other values of the constant parameter instead of including sub-ensembles of data for an extended range of values of the varying parameter.

For a system with one control parameter, it seems that other sets of data than the snapshots sampled close to the limiting flow for one parameter value on each side of a bifurcation are needed in order to produce a low-dimensional model with an accurate critical parameter value. For a lid driven cavity with a fixed rod, improved accuracy can be obtained by including snapshots for a co-rotating rod in the low-dimensional model. Another possibility could be to sample transient data. However, this would require a characterization of the transient and a consistent method of sampling the transient snapshots. This issue has not been pursued further.

It has been demonstrated that for a lid driven cavity with a fixed rod, improved accuracy of a low-dimensional model can be obtained by including snapshots for a co-rotating rod in the data ensemble used for the construction of the model. It would be interesting to investigate if this observation can be exploited within the context of the lid driven cavity without a rod. One might be able to obtain a low-dimensional model with improved accuracy by sampling of snapshots for simultaneously rotating end-covers. Perhaps investigations along this line would prove useful for other systems than the lid driven cavity.

Conclusion for the two-parameter low-dimensional model

A low-dimensional model, which is operational with two varying parameters, has been used for Hopf continuation. The resulting critical curve was compared in two points to the data obtained for the full model in 2.7.7 and 2.7.8. For one constant parameter, the critical values obtained for the other parameter compare favorably to the results obtained for the simpler models presented in 5.3.1 and 5.5.2. Thus, when considering the data ensemble used for the construction of a low-dimensional model for which a high degree of accuracy is desired, it may be beneficial to include sub-ensembles of data for other values of the constant parameter instead of including sub-ensembles of data for an extended range of values of the varying parameter. This observation might have implications for a wide range of applications.

block	Re_{lid}	γ	snapshots	weight
1	2550	0.00000	1	1.0
2	2550	0.00200	1	1.0
3	2550	0.00400	65	1.0
4	2550	0.00500	67	1.0
5	2550	0.00550	40	1.0
6	2550	0.00600	38	1.0

Table 5.2: Blocks of the SPOD used to construct the freqy model.

5.7 Modeling a bifurcating periodic solution

In 2.7.6 a bifurcating periodic solution was found for $Re_{lid} = 2550$. For the full simulation with a time step of $\Delta t = 0.04$ and a 201x101 computational grid, at $\gamma = 0.00500$ the basic frequency was found to be 0.03776 corresponding to a period of 26.48. At $\gamma = 0.00525$ the basic frequency was found to be 0.02571 corresponding to a period of 38.90. In the current study, it was attempted to reproduce the bifurcation by a low-dimensional model. The model was analyzed with AUTO 97.

The freqy model

An ensemble of data consisting of the sub-ensembles defined in Table 5.2 was used to construct a two-parameter low-dimensional model called freqy. For each parameter combination, the corresponding sub-ensemble was assigned to a numbered block of the SPOD. Also, the number of snapshots contained by each sub-ensemble is shown in Table 5.2. The sub-ensembles of an unsteady limiting flow each contain more than one snapshot. The sub-ensembles of a steady limiting flow only contain one snapshot each. The blocks containing the unsteady sub-ensembles were kept as small as possible in order to obtain a high numerical accuracy by enabling the use of the LAPACK SVD routine for as many of the blocks as possible. The resulting relative eigenvalue spectrum for 40 modes is shown in Fig. 5.29. Within each of the unsteady blocks, the relative eigenvalues decay slow compared to the previous modes after reaching a level below 10^{-10}. The blocks 3, 4, 5 and 6 of the SPOD yielded 7, 9, 10 and 12 modes respectively. The relative eigenvalues of the calculated modes were all above 10^{-10}. Thus, a high degree of numerical accuracy is expected for all of the modes used in the freqy model. The SPOD of the freqy ensemble was calculated for 35 and 40 modes. Each set of modes was used to construct a low-dimensional model.

In order to use AUTO 97 to detect bifurcations of a periodic solution, a Hopf bifurcation

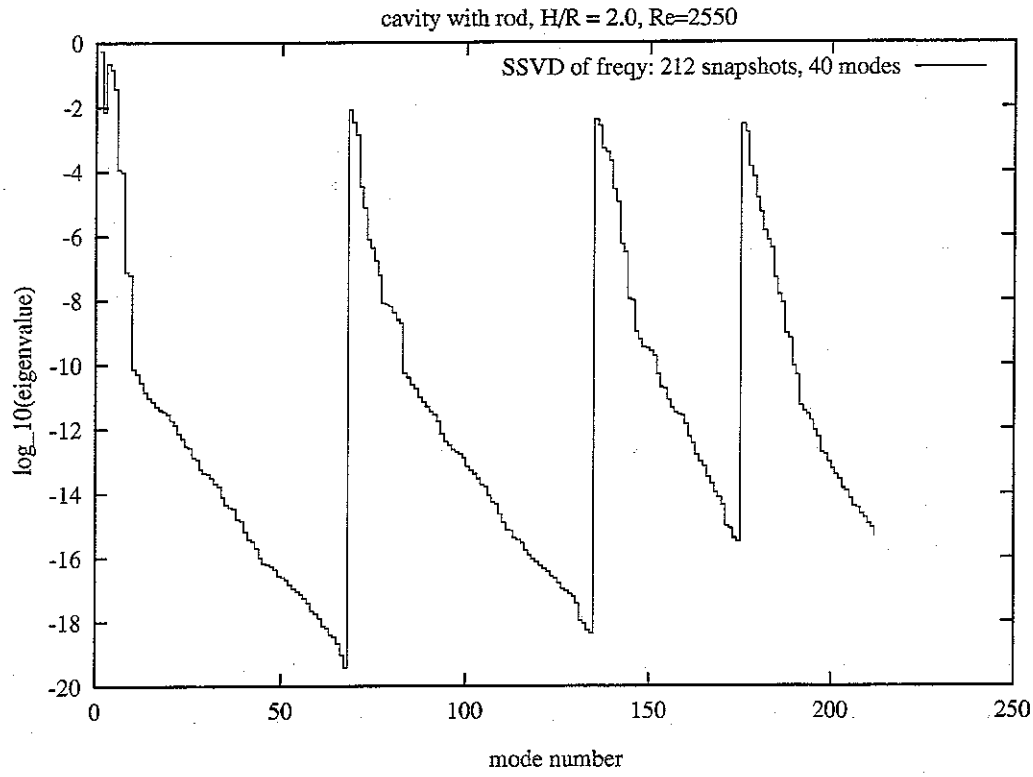

Figure 5.29: Relative eigenvalue spectrum for the SPOD of the data ensemble used for the freqy model with 40 modes.

needs to be located on a steady solution. The critical point of the Hopf bifurcation is used as a starting point for the calculation of the periodic solution in which only one parameter, in this case γ, is allowed to vary. During the Hopf continuation, the period is recorded as a function of the primary parameter. AUTO 97 is capable of detecting fold bifurcations on the periodic solution.

The periodic solution for 40 modes is shown in Fig. 5.30. The starting point of the curve is located at the left hand side of the diagram for $\gamma = 0.00354$. The corresponding period was calculated to be 26.40. The curve proceeds along the stable periodic solution towards larger values of γ until a torus bifurcation with the label "5" is encountered at $\gamma = 0.00499$. The dashed curve on the right hand side of the torus bifurcation indicates an unstable periodic solution. The other torus bifurcation labeled "6" does not comply with the full numerical simulations, but it does not lie in between any values of γ represented in the data ensemble used for the model construction. AUTO 97 is unable to perform continuation of torus bifurcations and to calculate the stable solution resulting from a torus bifurcation.

For the freqy model with 35 modes, the Hopf bifurcation occurs at $\gamma = 0.00360$ with a period of 26.36. A torus bifurcation of the periodic solution was found for $\gamma = 0.00479$ and no other bifurcation were detected before the chosen end-point at $\gamma = 0.00656$.

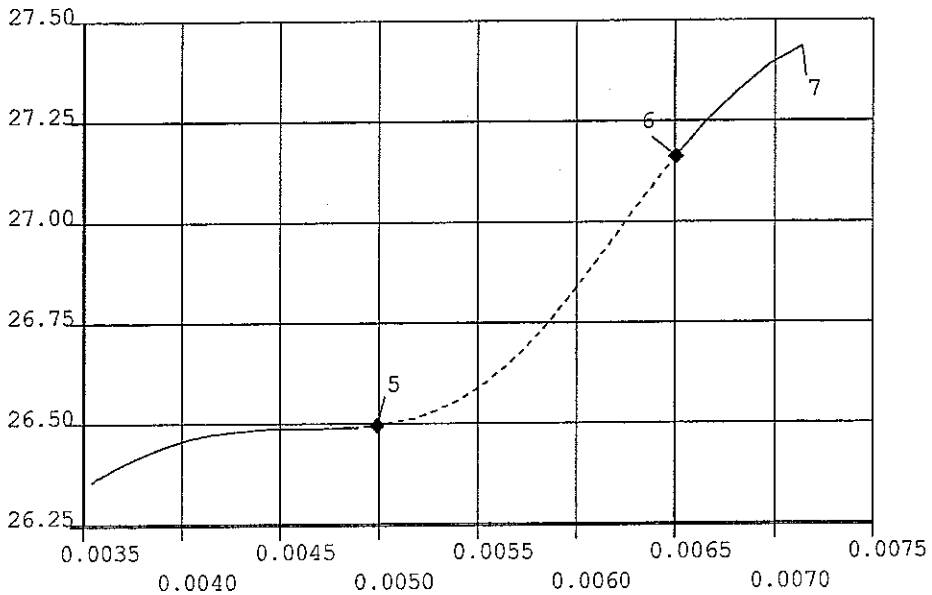

Figure 5.30: Graphical output from AUTO 97 of the periodic solution of the freqy model with 40 modes. The horizontal axis represents γ and the vertical axis represents the period.

For both the model with 35 modes and the model with 40 modes, the critical γ of the Hopf bifurcation was obtained with a deviation less than 4% from the actual critical value of 0.00366 and the obtained period deviates less than 0.5% from the actual value of 26.48. These results compare quite favorably to the results obtained for the models in 5.5.2.

For both of the models with 35 and 40 modes, the torus bifurcation of the periodic solution is detected for a γ-value close to the interval of γ-values in which a change of the frequencies occurs in the full solution. However, it has not been proved that a torus bifurcation occurs. A simpler solution would be the occurrence of fold bifurcations of the periodic solution generating hysteresis. This can be detected by full numerical simulations. In the event that the explanation of the behavior of the full solution is the fold bifurcations, it is expected that a low-dimensional model similar to the hopfy model, based on data including the hysteresis, would detect the fold bifurcations. A less satisfying aspect of this issue is that the constants used for controlling AUTO 97 might be set in such a way that very long transients are somehow confused with solutions containing multiple basic frequencies. Unfortunately, AUTO 97 cannot calculate the stable solution after a torus bifurcation. Otherwise, the Runge-Kutta solver described in 4.4 could be used to solve the ODE's of the low-dimensional model for different parameter values in order to verify the results of AUTO 97.

5.8 Conclusion

Low-dimensional models of the flow in the lid driven cavity with a rotating rod have been constructed by projection of the governing equations on modes resulting from the application of decomposition techniques to data obtained from full numerical simulations.

In order to compare the solutions of the current type of low-dimensional model with results obtained in the earlier work of E. A. Christensen *et al.* [10] a special version of the low-dimensional model was implemented for the lid driven cavity without a rod. The performance of this version of the model compared favorably with the earlier model. It was also verified that the low-dimensional model without the rod is able to reproduce the steady states appearing in an ensemble consisting of steady states only.

Encouraging results have been obtained by applying a decomposition technique called the Sequential Proper Orthogonal Decomposition (SPOD) which was developed to perform decompositions suitable for low-dimensional models. The SPOD is capable of transforming data organized in different sets separately while still producing orthogonal modes.

Also, a method developed for constructing low-dimensional models with more than one free parameter was applied to the flow in the lid driven cavity with a rotating rod. The resulting model allows one of the free parameters to appear in the inhomogeneous boundary conditions without the addition of any constraints. This is necessary because both the driving lid and the rotating rod can be controlled simultaneously. Apparently, the results are among the first to be obtained for low-dimensional models based on projection on POD modes for more than one free parameter.

The transition occurring for varying parameter values was studied and the results were compared to the original results obtained for the full numerical simulations. The effect of different methods of data sampling and variations of the decomposition procedure was investigated.

The results indicate that it is possible to predict an upper limit for the number of modes. For a few number of modes above this limit, the low-dimensional models deviate significantly from the full model. For a few number of modes below this limit, the models attain their best performance. The upper limit is decided by the number of modes at which the eigenvalues of the SPOD decay with the number of modes at a much smaller rate than for the previous modes. However, it is not obvious how many modes should be included to satisfy the minimum number of modes required to model a Hopf bifurcation.

A bifurcating periodic solution has been investigated, but no conclusive results can obtained without additional full numerical simulations.

A low-dimensional model with two varying parameters was utilized for Hopf continuation.

The resulting critical curve was compared to the data obtained for the full model. For one constant parameter, the accuracy of the critical values obtained for the varying parameter were superior to the results obtained for simpler models. Thus, when considering the data ensemble used for the construction of a low-dimensional model for which a high degree of accuracy is desired, it may be beneficial to include sub-ensembles of data for other values of the constant parameter instead of including sub-ensembles of data for an extended range of values of the varying parameter. This observation might have implications for a wide range of applications of low-dimensional models.

Appendix A

Derivation of the governing equations for the lid driven cavity

A.1 Outline

The foundation for computing solutions to any hydrodynamic problem is the Navier-Stokes equations and the continuity equation for incompressible flow. For constant viscosity these equations reduce to the commonly known form

$$\frac{\partial}{\partial t}\mathbf{v} + (\mathbf{v}\cdot\nabla)\mathbf{v} = -\frac{1}{\rho}\nabla P + \nu\nabla\cdot\nabla\mathbf{v}, \tag{A.1}$$

$$\nabla\cdot\mathbf{v} = 0, \tag{A.2}$$

where ∇P is the sum of the pressure gradient and conservative body forces such as gravity.

By rewriting the Navier-Stokes equations as a vorticity transport equation on rotational form, the term containing the pressure gradient can be eliminated. A constraint ensuring the existence of a pressure function is thereby introduced. For the lid driven cavity, however, the constraint is automatically satisfied when solving the azimuthal velocity equation. Also, by introducing a stream function, the continuity equation is automatically satisfied and the velocities can be replaced by derivatives of the stream function.

For rotational symmetry, and utilizing cylindrical coordinates, it is sufficient to consider the transport equations for the azimuthal components of the vorticity and velocity and a Poisson equation for the azimuthal component of the stream function.

A.2 Rotational form of the vorticity transport equation

The Navier-Stokes equations and the continuity equation can be stated in the dimensionless form

$$\frac{\partial}{\partial t}\mathbf{v} + (\mathbf{v}\cdot\nabla)\mathbf{v} = -\nabla P + \frac{1}{\mathrm{Re}}\nabla\cdot\nabla\mathbf{v}, \tag{A.3}$$

$$\nabla\cdot\mathbf{v} = 0. \tag{A.4}$$

The Reynolds number is given by

$$\mathrm{Re} = \frac{\Omega^2 D}{\nu} \tag{A.5}$$

where D is the characteristic diameter and Ω is the characteristic angular frequency.

Using the vector identities

$$(\mathbf{v}\cdot\nabla)\mathbf{v} = \frac{1}{2}\nabla(\mathbf{v}\cdot\mathbf{v}) - \mathbf{v}\times(\nabla\times\mathbf{v}), \tag{A.6}$$

$$\nabla\cdot\nabla\mathbf{v} = \nabla(\nabla\cdot\mathbf{v}) - \nabla\times(\nabla\times\mathbf{v}), \tag{A.7}$$

and utilizing the continuity equation (A.4) the Navier-Stokes equations (A.3) can be rewritten as

$$\frac{\partial}{\partial t}\mathbf{v} - \mathbf{v}\times(\nabla\times\mathbf{v}) = -\nabla(P + \frac{1}{2}\mathbf{v}\cdot\mathbf{v}) - \frac{1}{\mathrm{Re}}\nabla\times(\nabla\times\mathbf{v}). \tag{A.8}$$

Introducing the vorticity,

$$\boldsymbol{\omega} = \nabla\times\mathbf{v}, \tag{A.9}$$

and applying the curl operator yields the rotational form of the vorticity transport equation

$$\frac{\partial}{\partial t}\boldsymbol{\omega} - \nabla\times(\mathbf{v}\times\boldsymbol{\omega}) = -\frac{1}{\mathrm{Re}}\nabla\times(\nabla\times\boldsymbol{\omega}). \tag{A.10}$$

Because the curl operator involves differentiation it is necessary to introduce a constraint in order to establish the equivalence between the first formulation, which is given by (A.3) and (A.4), and the second formulation given by (A.4), (A.9) and (A.10). Define

$$\boldsymbol{\xi} = \frac{\partial}{\partial t}\mathbf{v} - \mathbf{v}\times(\nabla\times\mathbf{v}) + \frac{1}{\mathrm{Re}}\nabla\times(\nabla\times\mathbf{v}) \tag{A.11}$$

in a multiply connected domain. Furthermore, choose p loops $\Gamma_1, \ldots, \Gamma_p$ and assume that the domain can be made simply connected by p cuts which will cut the loops too. According to Daube *et al.* [12] the following theorem holds,

$$\left(\nabla\times\boldsymbol{\xi} = 0,\ \int_{\Gamma_i}\boldsymbol{\xi}\cdot d\mathbf{l} = 0,\ i = 1,\ldots,p\right) \Leftrightarrow (\exists\phi:\ \boldsymbol{\xi} = \nabla\phi), \tag{A.12}$$

where $\mathbf{l}$ is the tangential vector. Thus, the constraint,

$$\int_{\Gamma_i}\left(\frac{\partial}{\partial t}\mathbf{v} - \mathbf{v}\times(\nabla\times\mathbf{v}) + \frac{1}{\mathrm{Re}}\nabla\times(\nabla\times\mathbf{v})\right)\cdot d\mathbf{l} = 0,\ i = 1,\ldots,p, \tag{A.13}$$

ensures the existence of a pressure function P so that (A.8) is satisfied. It has now been established that the first formulation, which is given by (A.3) and (A.4), is equivalent to the second formulation given by (A.4), (A.9), (A.10) and (A.13).

Note that the theorem (A.12) also implies that

$$\int_{\Gamma_i} \left(\nabla (P + \frac{1}{2} \mathbf{v} \cdot \mathbf{v}) \right) \cdot d\mathbf{l} = 0, \ i = 1, \ldots, p. \tag{A.14}$$

Therefore, if (A.8) is satisfied along the loops, then the constraint (A.13) is satisfied. In the case of the lid driven cavity with a rod, only one loop is necessary because the domain can be made simply connected by a cut from the rod to the cylinder wall. Placing the loop in a plane, which is orthogonal to the center axis, and solving the azimuthal component of the velocity transport equation (A.8) ensures that the constraint (A.13) is satisfied.

A.3 Cylindrical coordinates

Introduce the cylindrical coordinates,

$$(x^1, x^2, x^3) = (r, \theta, z), \tag{A.15}$$

and the orthogonal coordinate system,

$$(\xi^1, \xi^2, \xi^3) = (r \cos\theta, r \sin\theta, z). \tag{A.16}$$

For a contravariant tensor

$$\mathbf{T} = T^j \mathbf{e}_j \tag{A.17}$$

the rotation is given by

$$\nabla \times \mathbf{T} = \frac{1}{\sqrt{g}} \begin{vmatrix} \mathbf{e}_1 & \mathbf{e}_2 & \mathbf{e}_3 \\ \frac{\partial}{\partial x^1} & \frac{\partial}{\partial x^2} & \frac{\partial}{\partial x^3} \\ g_{1j} T^j & g_{2j} T^j & g_{3j} T^j \end{vmatrix} \tag{A.18}$$

where the fundamental tensor is defined by

$$\mathbf{g} = \{g_{ij}\} = \{\mathbf{e}_i \cdot \mathbf{e}_j\} \tag{A.19}$$

and g represents the determinant

$$g = \det \mathbf{g}. \tag{A.20}$$

Because (ξ^1, ξ^2, ξ^3) is orthogonal the Jacobian

$$\mathbf{J} = \left\{ \frac{\partial \xi^i}{\partial x^j} \right\} \tag{A.21}$$

can be used for calculating the fundamental tensor via

$$\{g_{ij}\} = \mathbf{J}^{\mathrm{T}}\mathbf{J} = \begin{bmatrix} 1 & 0 & 0 \\ 0 & r^2 & 0 \\ 0 & 0 & 1 \end{bmatrix} \tag{A.22}$$

which yields

$$g = \det\{g_{ij}\} = r^2. \tag{A.23}$$

Inserting, the contravariant rotation for cylindrical coordinates becomes

$$\nabla \times \mathbf{T} = \frac{1}{r}\begin{vmatrix} \mathbf{e}_1 & \mathbf{e}_2 & \mathbf{e}_3 \\ \frac{\partial}{\partial r} & \frac{\partial}{\partial \theta} & \frac{\partial}{\partial z} \\ T^1 & r^2T^2 & T^3 \end{vmatrix} \tag{A.24}$$

The covariant tensor

$$\mathbf{T} = T_j\mathbf{e}^j \tag{A.25}$$

is related to the contravariant tensor via the relations

$$\mathbf{e}_k = g_{kj}\mathbf{e}^j \tag{A.26}$$

$$T_k = g_{kj}T^j \tag{A.27}$$

By substitution, the covariant rotation for cylindrical coordinates is found to be

$$\nabla \times \mathbf{T} = \frac{1}{r}\begin{vmatrix} \mathbf{e}^1 & r^2\mathbf{e}^2 & \mathbf{e}^3 \\ \frac{\partial}{\partial r} & \frac{\partial}{\partial \theta} & \frac{\partial}{\partial z} \\ T_1 & T_2 & T_3 \end{vmatrix} \tag{A.28}$$

It is useful to consider *unit tangential vectors* which are popular in the literature of fluid mechanics. By choosing

$$\mathbf{e}_r = \mathbf{e}_1, \quad r\mathbf{e}_\theta = \mathbf{e}_2, \quad \mathbf{e}_z = \mathbf{e}_3, \tag{A.29}$$

it is obtained that $\mathbf{e}_r$ is parallel to $\mathbf{e}_1$, $\mathbf{e}_\theta$ parallel to $\mathbf{e}_2$ and $\mathbf{e}_z$ parallel to $\mathbf{e}_3$ in such a way that

$$\mathbf{e}_r \cdot \mathbf{e}_r = 1, \quad \mathbf{e}_\theta \cdot \mathbf{e}_\theta = 1, \quad \mathbf{e}_z \cdot \mathbf{e}_z = 1. \tag{A.30}$$

Defining

$$\mathbf{T} = T_r\mathbf{e}_r + T_\theta\mathbf{e}_\theta + T_z\mathbf{e}_z \tag{A.31}$$

it is follows that

$$T_r = T_1, \quad T_\theta = rT_2, \quad T_z = T_3. \tag{A.32}$$

By substitution, the rotation formulated by unit tangential vectors for cylindrical coordinates becomes

$$\nabla \times \mathbf{T} = \frac{1}{r} \begin{vmatrix} \mathbf{e}_r & r\mathbf{e}_\theta & \mathbf{e}_z \\ \frac{\partial}{\partial r} & \frac{\partial}{\partial \theta} & \frac{\partial}{\partial z} \\ T_r & rT_\theta & T_z \end{vmatrix} \tag{A.33}$$

In a right-oriented coordinate system, the cross product is given by

$$\mathbf{T} \times \mathbf{S} = \frac{1}{\sqrt{g}} \begin{vmatrix} \mathbf{e}_1 & \mathbf{e}_2 & \mathbf{e}_3 \\ T_1 & T_2 & T_3 \\ S_1 & S_2 & S_3 \end{vmatrix} \tag{A.34}$$

Using unit tangential vectors the cross product for cylindrical coordinates becomes

$$\mathbf{T} \times \mathbf{S} = \frac{1}{r} \begin{vmatrix} \mathbf{e}_r & r\mathbf{e}_\theta & \mathbf{e}_z \\ T_r & rT_\theta & T_z \\ S_r & rS_\theta & S_z \end{vmatrix} = \begin{vmatrix} \mathbf{e}_r & \mathbf{e}_\theta & \mathbf{e}_z \\ T_r & T_\theta & T_z \\ S_r & S_\theta & S_z \end{vmatrix} \tag{A.35}$$

The general contravariant formulation of the divergence is

$$\nabla \cdot \mathbf{T} = \frac{1}{\sqrt{g}} \frac{\partial}{\partial x^i} (\sqrt{g} T^i) \tag{A.36}$$

which for the cylindrical coordinates (A.15) is given by

$$\nabla \cdot \mathbf{T} = \frac{1}{r} \frac{\partial}{\partial r} (rT^1) + \frac{\partial}{\partial \theta} T^2 + \frac{\partial}{\partial z} T^3. \tag{A.37}$$

Using unit tangential vectors the divergence for cylindrical coordinates becomes

$$\nabla \cdot \mathbf{T} = \frac{1}{r} \frac{\partial}{\partial r} (rT_r) + \frac{1}{r} \frac{\partial}{\partial \theta} T_\theta + \frac{\partial}{\partial z} T_z. \tag{A.38}$$

A.4 The Poisson equation

The stream function $\boldsymbol{\psi}$ is defined so that the velocity field is given by

$$\mathbf{v} = -\nabla \times \boldsymbol{\psi}. \tag{A.39}$$

In cylindrical coordinates this yields

$$\mathbf{v} = -\frac{1}{r} \begin{vmatrix} \mathbf{e}_r & r\mathbf{e}_\theta & \mathbf{e}_z \\ \frac{\partial}{\partial r} & \frac{\partial}{\partial \theta} & \frac{\partial}{\partial z} \\ \psi_r & r\psi_\theta & \psi_z \end{vmatrix} \tag{A.40}$$

However, by choosing a covariant stream function

$$\boldsymbol{\psi} = \psi_j \mathbf{e}^j \tag{A.41}$$

and using

$$\psi_r = \psi_1, \quad \psi_\theta = r\psi_2, \quad \psi_z = \psi_3 \tag{A.42}$$

the following expression is obtained

$$\mathbf{v} = -\frac{1}{r}\begin{vmatrix} \mathbf{e}_r & r\mathbf{e}_\theta & \mathbf{e}_z \\ \frac{\partial}{\partial r} & \frac{\partial}{\partial \theta} & \frac{\partial}{\partial z} \\ \psi_1 & \psi_2 & \psi_3 \end{vmatrix} \tag{A.43}$$

For rotational symmetry let $\psi = \psi_2$ and observe that

$$v_r = \frac{1}{r}\frac{\partial \psi}{\partial z}, \quad v_z = -\frac{1}{r}\frac{\partial \psi}{\partial r}. \tag{A.44}$$

Hence, the vorticity becomes

$$\boldsymbol{\omega} = \nabla \times \mathbf{v} = \frac{1}{r}\begin{vmatrix} \mathbf{e}_r & r\mathbf{e}_\theta & \mathbf{e}_z \\ \frac{\partial}{\partial r} & \frac{\partial}{\partial \theta} & \frac{\partial}{\partial z} \\ \frac{1}{r}\frac{\partial \psi}{\partial z} & rv_\theta & -\frac{1}{r}\frac{\partial \psi}{\partial r} \end{vmatrix} \tag{A.45}$$

Defining

$$\omega = \omega_\theta \tag{A.46}$$

it is obtained that

$$r\omega = \frac{\partial^2 \psi}{\partial r^2} - \frac{1}{r}\frac{\partial \psi}{\partial r} + \frac{\partial^2 \psi}{\partial z^2}. \tag{A.47}$$

Also,

$$\omega_r = -\frac{\partial}{\partial z}v_\theta, \quad \omega_z = \frac{1}{r}\frac{\partial}{\partial r}(rv_\theta). \tag{A.48}$$

Now, define

$$[\mathbf{T}]_\theta = T_\theta. \tag{A.49}$$

For rotational symmetry

$$[\nabla(\nabla \cdot \boldsymbol{\psi})]_\theta = 0 \tag{A.50}$$

Thus, the azimuthal component of the equation

$$\boldsymbol{\omega} = -\nabla \times (\nabla \times \boldsymbol{\psi}) = \nabla^2 \boldsymbol{\psi} - \nabla(\nabla \cdot \boldsymbol{\psi}) \tag{A.51}$$

reduces to

$$\omega = \nabla^2 \psi. \tag{A.52}$$

Therefore, (A.47) will be referred to as the *Poisson equation.*

A.5 The conservative vorticity transport equation

Restating the vorticity transport equation (A.10) on rotational form

$$\frac{\partial}{\partial t}\boldsymbol{\omega} - \nabla \times (\mathbf{v} \times \boldsymbol{\omega}) = -\frac{1}{\mathrm{Re}}\nabla \times (\nabla \times \boldsymbol{\omega}). \tag{A.53}$$

and recalling the rotation formulated by unit tangential vectors for cylindrical coordinates (A.33) it is found that the azimuthal component of the vorticity transport equation becomes

$$\frac{\partial}{\partial t}\omega = -\left(\frac{\partial}{\partial r}[\mathbf{v} \times \boldsymbol{\omega}]_z - \frac{\partial}{\partial z}[\mathbf{v} \times \boldsymbol{\omega}]_r\right) + \frac{1}{\mathrm{Re}}\left(\frac{\partial}{\partial r}[\nabla \times \boldsymbol{\omega}]_z - \frac{\partial}{\partial z}[\nabla \times \boldsymbol{\omega}]_r\right) \tag{A.54}$$

Using (A.35) for rotational symmetry gives

$$\mathbf{v} \times \boldsymbol{\omega} = \begin{vmatrix} \mathbf{e}_r & \mathbf{e}_\theta & \mathbf{e}_z \\ v_r & v_\theta & v_z \\ -\frac{\partial}{\partial z}v_\theta & \omega & \frac{1}{r}\frac{\partial}{\partial r}(rv_\theta) \end{vmatrix} \tag{A.55}$$

which yields

$$\frac{\partial}{\partial r}[\mathbf{v} \times \boldsymbol{\omega}]_z = \frac{\partial}{\partial r}\left(v_r\omega + v_\theta\frac{\partial}{\partial z}v_\theta\right) \tag{A.56}$$

$$\frac{\partial}{\partial z}[\mathbf{v} \times \boldsymbol{\omega}]_r = \frac{\partial}{\partial z}\left(-v_z\omega + \frac{1}{r}v_\theta\frac{\partial}{\partial r}(rv_\theta)\right). \tag{A.57}$$

Thus, the convection terms can be put on conservative form

$$-\left(\frac{\partial}{\partial r}[\mathbf{v} \times \boldsymbol{\omega}]_z - \frac{\partial}{\partial z}[\mathbf{v} \times \boldsymbol{\omega}]_r\right) = -\frac{\partial}{\partial r}(v_r\omega) - \frac{\partial}{\partial z}(v_z\omega) + \frac{1}{r}\frac{\partial}{\partial z}(v_\theta^2). \tag{A.58}$$

Using (A.33) for rotational symmetry gives

$$\nabla \times \boldsymbol{\omega} = \frac{1}{r}\begin{vmatrix} \mathbf{e}_r & r\mathbf{e}_\theta & \mathbf{e}_z \\ \frac{\partial}{\partial r} & \frac{\partial}{\partial \theta} & \frac{\partial}{\partial z} \\ -\frac{\partial}{\partial z}v_\theta & r\omega & \frac{1}{r}\frac{\partial}{\partial r}(rv_\theta) \end{vmatrix} \tag{A.59}$$

which yields the diffusion terms

$$\begin{aligned} \frac{\partial}{\partial r}[\nabla \times \boldsymbol{\omega}]_z - \frac{\partial}{\partial z}[\nabla \times \boldsymbol{\omega}]_r &= \frac{\partial}{\partial r}\left(\frac{1}{r}\frac{\partial}{\partial r}(r\omega)\right) + \frac{\partial}{\partial z}\left(\frac{1}{r}\frac{\partial}{\partial z}(r\omega)\right) \\ &= -\frac{1}{r^2}\omega + \frac{1}{r}\frac{\partial}{\partial r}\left(r\frac{\partial\omega}{\partial r}\right) + \frac{\partial^2\omega}{\partial z^2}. \end{aligned} \tag{A.60}$$

Inserting the convection terms (A.58) and the diffusion terms (A.60) into the azimuthal component of the vorticity transport equation (A.54) yields the *vorticity transport equation on conservative form*

$$\frac{\partial\omega}{\partial t} = -\frac{\partial}{\partial r}(v_r\omega) - \frac{\partial}{\partial z}(v_z\omega) + \frac{1}{r}\frac{\partial}{\partial z}(v_\theta^2) + \frac{1}{\mathrm{Re}}\left(-\frac{1}{r^2}\omega + \frac{1}{r}\frac{\partial}{\partial r}\left(r\frac{\partial\omega}{\partial r}\right) + \frac{\partial^2\omega}{\partial z^2}\right). \tag{A.61}$$

A.6 The conservative azimuthal velocity transport equation

Restating (A.8)

$$\frac{\partial}{\partial t}\mathbf{v} - \mathbf{v} \times (\nabla \times \mathbf{v}) = -\nabla(P + \frac{1}{2}\mathbf{v} \cdot \mathbf{v}) - \frac{1}{\mathrm{Re}}\nabla \times (\nabla \times \mathbf{v}) \tag{A.62}$$

it is seen that the azimuthal component in cylindrical coordinates for rotational symmetry reduces to

$$\frac{\partial}{\partial t}v_\theta - [\mathbf{v} \times (\nabla \times \mathbf{v})]_\theta = -\frac{1}{\mathrm{Re}}[\nabla \times (\nabla \times \mathbf{v})]_\theta. \tag{A.63}$$

Using (A.35) and (A.33) and utilizing rotational symmetry the following is obtained

$$\begin{aligned} -[\mathbf{v} \times (\nabla \times \mathbf{v})]_\theta &= +v_r[\nabla \times \mathbf{v}]_z - v_z[\nabla \times \mathbf{v}]_r & \text{(A.64)} \\ &= v_r\frac{1}{r}\frac{\partial}{\partial r}(rv_\theta) + v_z\frac{1}{r}\frac{\partial}{\partial z}(rv_\theta) \\ &= \frac{v_r v_\theta}{r} + v_r\frac{\partial v_\theta}{\partial r} + v_z\frac{\partial v_\theta}{\partial z}. & \text{(A.65)} \end{aligned}$$

Rendering the continuity equation (A.4) dimensionless and applying (A.38) for rotational symmetry yields

$$\frac{1}{r}\frac{\partial}{\partial r}(rv_r) + \frac{\partial v_z}{\partial z} = 0. \tag{A.66}$$

Expanding, multiplying by v_θ, adding to (A.65) and collecting terms yields the azimuthal component of the convection terms on conservative form

$$\begin{aligned} -[\mathbf{v} \times (\nabla \times \mathbf{v})]_\theta &= \frac{v_r v_\theta}{r} + v_r\frac{\partial v_\theta}{\partial r} + v_z\frac{\partial v_\theta}{\partial z} + v_\theta\left(\frac{v_r}{r} + \frac{\partial v_r}{\partial r} + \frac{\partial v_z}{\partial z}\right) \\ &= \frac{\partial}{\partial r}(v_r v_\theta) + \frac{\partial}{\partial z}(v_z v_\theta) + \frac{2}{r}v_r v_\theta. & \text{(A.67)} \end{aligned}$$

The azimuthal component of the diffusion terms can be evaluated by applying (A.33) twice, utilizing rotational symmetry and expanding the terms yielding

$$\begin{aligned} -[\nabla \times (\nabla \times \mathbf{v})]_\theta &= \frac{1}{r}r\left(\frac{\partial}{\partial r}[\nabla \times \mathbf{v}]_z - \frac{\partial}{\partial z}[\nabla \times \mathbf{v}]_r\right) \\ &= \frac{\partial}{\partial r}\left(\frac{1}{r}\frac{\partial}{\partial r}(rv_\theta)\right) + \frac{\partial}{\partial z}\left(\frac{1}{r}\frac{\partial}{\partial z}(rv_\theta)\right) \\ &= -\frac{1}{r^2}\left(v_\theta + r\frac{\partial v_\theta}{\partial r}\right) + \frac{1}{r}\frac{\partial}{\partial r}\left(v_\theta + r\frac{\partial v_\theta}{\partial r}\right) + \frac{\partial^2 v_\theta}{\partial z^2} \\ &= -\frac{1}{r^2}v_\theta + \frac{1}{r}\frac{\partial}{\partial r}\left(r\frac{\partial v_\theta}{\partial r}\right) + \frac{\partial^2 v_\theta}{\partial z^2}. & \text{(A.68)} \end{aligned}$$

Inserting the convection terms (A.67) and the diffusion terms (A.68) into (A.63) yields the *azimuthal velocity transport equation on conservative form*

$$\frac{\partial}{\partial t}v_\theta = -\frac{\partial}{\partial r}(v_r v_\theta) - \frac{\partial}{\partial z}(v_z v_\theta) - \frac{2}{r}v_r v_\theta + \frac{1}{\mathrm{Re}}\left(-\frac{1}{r^2}v_\theta + \frac{1}{r}\frac{\partial}{\partial r}\left(r\frac{\partial v_\theta}{\partial r}\right) + \frac{\partial^2 v_\theta}{\partial z^2}\right). \tag{A.69}$$

This concludes the derivation.

Appendix B

Numerical accuracy of the eigenvalues of POD and SPOD

Let $\mathbf{R}$ be a symmetrical matrix, for instance the auto-covariance matrix of a POD. Consider the eigenvalue κ_i of the matrix $(\mathbf{R}+\mathbf{D})$. Assume that the elements of $\mathbf{D}$ are small compared to the elements of $\mathbf{R}$. Then there exists an eigenvalue, λ_i, for $\mathbf{R}$ so that

$$|\lambda_i - \kappa_i| \leq \|\mathbf{D}\|_2 \tag{B.1}$$

(see Madsen and Nielsen [20] or another introduction to numerical analysis of eigenvalues for matrices). Here, $\|\cdot\|_2$ denotes the matrix 2-norm defined by

$$\|\mathbf{Y}\|_2 = \max_{\|\mathbf{x}\|_2 = 1} \|\mathbf{Y}\mathbf{x}\|_2 \tag{B.2}$$

for the matrix $\mathbf{Y}$. Letting λ_1 be the largest eigenvalue of $\mathbf{R}$,

$$\|\mathbf{R}\|_2 = \max_i |\lambda_i| = \lambda_1. \tag{B.3}$$

Thus,

$$\frac{|\lambda_i - \kappa_i|}{\lambda_1} \leq \frac{\|\mathbf{D}\|_2}{\|\mathbf{R}\|_2} \tag{B.4}$$

For sufficiently large eigenvalues, this relationship guarantees the existence of an eigenvalue for the matrix $\mathbf{R}$ near a computed eigenvalue. However, if the ratio λ_i/λ_1 between an eigenvalue and the largest eigenvalue becomes smaller than the right hand side of (B.4), several of the eigenvalues less than λ_i may lie near the computed eigenvalue. Thus, the eigenvalues cannot be distinguished from each other. This offers a theoretical limit for the smallest eigenvalues that can be obtained with a given machine accuracy.

When calculating an auto-covariance matrix, $\mathbf{R} = \mathbf{U}^T\mathbf{U}$, the worst conceivable case of degraded numerical accuracy is the addition of many small products to one very large product,

i.e. for a machine accuracy of ϵ and for $r_{ij} = \sum u_{ki}u_{kj}$,

$$r_{ij} + d_{ij} = (\mathbf{u}_i + \boldsymbol{\delta}_i) \cdot (\mathbf{u}_j + \boldsymbol{\delta}_j) \approx \sum_{k=1}^{P} \left(u_{ki}u_{kj} + 2\epsilon \sum_{m=1}^{P} u_{mi}u_{mj} \right) = r_{ij} + 2P\epsilon r_{ij}. \quad \text{(B.5)}$$

In this relation it has been exploited that, for any k, the addition of the product $u_{ki}\delta_{kj}$ introduces a numerical error of the same magnitude as the addition of the first product, $u_{1i}\delta_{1j}$, which was assumed to be very large, and that $u_{1i}u_{1j} \approx \sum_m u_{mi}u_{mj}$. Thus, for the worst case,

$$\|\mathbf{D}\|_2 \approx 2P\epsilon\|\mathbf{R}\|_2. \quad \text{(B.6)}$$

The most favorable case is when products of comparable size are added, i.e.

$$r_{ij} + d_{ij} = (\mathbf{u}_i + \boldsymbol{\delta}_i) \cdot (\mathbf{u}_j + \boldsymbol{\delta}_j) \approx \sum_{k=1}^{P} (u_{ki}u_{kj} + 2\epsilon u_{ki}u_{kj}) = r_{ij} + 2\epsilon r_{ij}. \quad \text{(B.7)}$$

In this case,

$$\|\mathbf{D}\|_2 \approx 2\epsilon\|\mathbf{R}\|_2. \quad \text{(B.8)}$$

The available machine accuracy is $\epsilon = 2.2 \cdot 10^{-16}$. For the worst case, a POD based on direct calculation of the auto-covariance matrix has a theoretical limit of accuracy of order $2P\epsilon = 1.76 \cdot 10^{-11}$ for the ratio between the smallest and the largest eigenvalue. Here, $P = 40000$ denotes the number of vector components in a snapshot. For a practical calculation of the auto-covariance matrix the accuracy is assumed to be increased by one decade or more. However, a few decades of accuracy might be lost due to the practical method used for solving the eigenvalue problem. Hence, an accuracy of at least 10 decades is expected.

For the POD based on direct calculation of the auto-covariance matrix, the least conservative estimate of the theoretical limit of accuracy for the ratio between the smallest and the largest eigenvalue is $2\epsilon = 4.4 \cdot 10^{-16}$. Taking into account the loss of a few decades due to the method used for solving the eigenvalue problem, at most 13 decades of accuracy can be expected.

By using the method called Singular Value Decomposition (SVD) to calculate the POD the accuracy can be improved. When using the LAPACK SVD routine, the auto-covariance matrix defined in 3.1 is not calculated directly and it is the singular values which are returned. The eigenvalues are calculated as the squares of the singular values. Therefore, this method should yield at least twice the accuracy of a POD based on direct calculation of the auto-covariance matrix, i.e. more than 20 decades.

In this study, utilization of the LAPACK SVD routine for calculating the POD was limited to 104 snapshots. For calculating the POD's involved in the SPOD the total number of snapshots was limited to 156 snapshots or less depending on the data ensemble and the calculated modes. When more snapshots were required, the LAPACK SVD routine was

applied for as many of the first blocks of the SPOD as possible in order to minimize the numerical errors introduced by the sequential orthogonalization. The POD utilizing direct calculation of the auto-covariance matrix was applied for the remaining blocks when needed.

Bibliography

[1] N. Aubry, P. Holmes, J. L. Lumley, E. Stone, "The dynamics of coherent structures in the wall region of a turbulent boundary layer," J. Fluid Mech., **192** (1988), pp. 115-173.

[2] S. Banerjee, J. V. Cole, K. F. Jensen, "Designing Reduced-Order Models for Rapid Thermal Processing Systems," J. Electrochem. Soc., Vol. 145, No. 11, 1988, pp. 3974-3981.

[3] A. K. Bangia, P. F. Batcho, I. G. Kevredikis, G. E. Karniadakis, "Unsteady Two-dimensional flows in complex geometries: Comparative bifurcation studies with global eigenfunction expansions," SIAM J. Sci. Comput., Vol. 18, No. 3, 1997, pp. 775-805.

[4] G. Berkooz, P. Holmes, and J. L. Lumley, "The Proper Orthogonal Decomposition in the Analysis of Turbulent Flows," Annu. Rev. Fluid Mech. 1993, 25:539-575.

[5] M. Brøns, "Topological fluid mechanics of Axisymmetric Flows," in *Simulation and Identification of Organized Structures in Flows*, edited by J. N. Sørensen, E. J. Hopfinger, and N. Aubry (Kluwer Academic Publishers, Dordrecht, 1998) 213-222.

[6] M. Brøns, and J. N. Hartnack, "Streamline topologies near simple degenerate critical points in two-dimensional flow away from boundaries," Phys. Fluids **11** (2), 314-324, 1999.

[7] M. Brøns, L. K. Voigt, and J. N. Sørensen, "Streamline topology of steady axisymmetric vortex breakdown in a cylinder with co- and counter-rotating end-covers," J. Fluid Mech., **401** (1999), pp. 275-292.

[8] P. Buchhave, M. L. Jakobsen, C. H. Westergaard, and J. N. Sørensen, "PIV: Measurement of the early transition of a rotating flow in a closed cylinder," Fourth International Conference on Laser Anemometry, Advances and Applications, Cleveland, Ohio, 1991.

[9] W. Cazemier, R. W. C. P. Verstappen, A. E. P. Veldman, "Proper orthogonal decomposition and low- dimensional models for driven cavity flows," Phys. Fluids **10** (7), 1685-1699, 1998.

[10] E. A. Christensen, J. N. Sørensen, M. Brøns, P. L. Christiansen, "Low-Dimensional Representations of Early Transition in Rotating Fluid Flow," Theoret. Comput. Fluid Dynamics (1993) 5: 259-267.

[11] E. A. Christensen, M. Brøns, and J. N. Sørensen, "Evaluation of Proper Orthogonal Decomposition- based decomposition techniques applied to parameter-dependent non-turbulent flows," SIAM J. Sci. Comput., Vol. 21, No. 4, 2000, pp. 1419-1434.

[12] O. Daube, J.-L. Guermond, A. Sellier, "Sur la formulation vitesse-tourbillon des équations de Navier-Stokes en écoulement incompressible," C. R. Acad. Sci. Paris, t. 313, Série II, pp. 377-382, 1991. Including abridged english version titled "On the velocity-vorticity formulation of Navier-Stokes equations in incompressible flow."

[13] J. Delville, "Characterization of the Organization in Shear Layers via Proper Orthogonal Decomposition," from J. P. Bonnet, and N. Glauser (eds.), *Eddy Structure Identification in Free Turbulent Shear Flows*, 225-237, 1993, Kluwer Academic Publishers.

[14] E. J. Doedel, A. R. Champneys, T. F. Fairgrieve, Y. A. Kuznetsov, B. Sandstede and X. Wang, "AUTO 97: Continuation and bifurcation software for ordinary differential equations (with HomCont)," Concordia University, Montreal, Canada, 1997. Available via FTP from pub/doedel/auto at *ftp.cs.concordia.ca.*

[15] M. P. Escudier, "Observations of the flow produced in a cylindrical container by a rotating endwall," Exp. Fluids **2**, (1984), pp. 189-196.

[16] K. Fukanaga, *Statistical Pattern Recognition*, Second Edition, 1990, Academic Press.

[17] J. N. Hartnack, "Streamline topologies near a fixed wall using normal forms," Acta Mechanica, 136, 1-2, pp. 55-75 (1999).

[18] H. Hussain, V. Shtern, F. Hussain, "Control of Vortex Breakdown Using Vortex Generators," 28th AIAA Fluid Dynamics Conference, 4th AIAA Shear Flow Control Conference, Snowmass Village, 1997.

[19] J. L. Lumley, "The structure of inhomogeneous turbulent flows," *Atmospheric turbulence and radio wave propagation* (eds. A. M. Yaglom and V. I. Tatarski), 1967, pp. 167-178.

[20] K. Madsen, H. B. Nielsen, *Egenværdier for matricer*, Hæfte 36, Numerisk Institut, Danmarks Tekniske Højskole, Polyteknisk Forlag, 1975.

[21] M. Manhart, "Vortex Shedding from a Hemisphere in a Turbulent Boundary Layer," Theoret. Comput. Fluid Dynamics, 1998, 12 (1): pp. 1-28.

[22] T. Mullin, S. J. Tavener, K. A. Cliffe, "On The Creation of Stagnation Points in a Rotating Flow," ASME Annual Congress, Dallas, Nov. 1997, (also submitted to the ASME Journal of Fluids Engineering).

[23] T. Mullin, J. J. Kobine, S. J. Taverner, K. A. Cliffe, "On the creation of stagnation points near straight and sloped walls," Phys. Fluids **12** (2), 425-431, 1999.

[24] M. Münkel, F. Kaiser, O. Hess, "Stabilization of spatiotemporally chaotic semiconductor laser arrays by means of delayed optical feedback," Physical Review E, Vol. 56, No. 4, 1997, pp. 3868-3875.

[25] B. Ronnenberg, "Ein selbstjustierendes 3-komponenten-LDA nach dem vergleigh-strahlverfaren, angewendt für untersuchungen in einer stationaren zylindersymmetrischen drehströmung mit einem rühckströmgebiet," Bericht 20, Max-Planck-Institut für Strömungsforschung, Göttingen, 1977.

[26] R. A. Sahan, A. Liakopoulos, H. Gunes, "Reduced dynamical models of nonisothermal transitional grooved-channel flow," Phys. Fluids **9** (3), 1997, pp. 551-565.

[27] J. N. Sørensen, Ta Phuoc Loc, "High-order axisymmetric Navier-Stokes code: Description and evaluation of boundary conditions," Int. J. Num. Methods Fluids **9**, 1517 (1989).

[28] J. N. Sørensen, E. A. Christensen, "Direct numerical simulation of rotating fluid flow in a closed cylinder," Phys. Fluids **7** (4), 1995.

[29] J. N. Sørensen, M. O. L. Hansen, and E. A. Christensen, "Numerical Investigation of Symmetry Breakdown in a Cylindrical Lid Driven Cavity," Proceedings of the Third ECCOMAS Computational Fluid Dynamics Conference, pp. 439-444, Paris, 1996.

[30] I. Triandaf, I. B. Schwartz, "Karhunen-Loeve mode control of chaos in a reaction-diffusion process," Physical Review E, Vol. 56, No. 1, 1997, pp. 204-212.

[31] H. U. Vogel, "Experimentelle ergebnisse über die laminare strömung in einem zylindrischen gehaüse mit darin rotierender scheibe," Bericht 6, Max-Planck-Institut für Strömungsforschung, Göttingen, 1968.

Recent Ph.D.-dissertations in Fluid Mechanics

Sørensen, J. N. Three-Level, Viscous-Inviscid Interaction Technique for the Prediction of Separated Flow Past Rotating Wing, AFM 86-03, 1986

Michelsen, J. A. Modeling of Laminar Incompressible rotating Fluid Flow, AFM 86-05, and Modeling of Turbulent Incompressible Rotating Fluid Flow, AFM 86-07, 1986

Sørensen, L. S. Three-Dimensional Electro-Fluid-Dynamics in Tuft Corona Wire-Plate Precipitators, AFM 89-03, 1989

Gervang, B. Numerical Simulation of 3-Dimensional Flow in Straight and Curved Ducts of Rectangular Cross Section, AFM 89-09, 1989

Andresen, E. Statistical Approach to Continuum Models for Turbulent Gas Particle Flows, AFM 90-04, 1990

Nielsen, N. F. Low Reynolds Number Fluid Dynamics with Applications to suspension feeding Animals, AFM 91-10, 1991

Zamany, J. Modeling of Particle Transport in Commercial Electrostatic Precipitators, Ph.D under ATV, EF316, 1992

Christensen, E. A. Laminar-Turbulent Transition in the Rotating Driven Cavity Problem, AFM 93-12, 1993

Trinh, C. M. Turbulence Modelling of Confined Swirling Flows, Risø-R-647, 1993

Meyer, K. M. Experimental and Numerical Investigation of Turbulent Flow and Heat Transfer in Staggered Tube Bundles, AFM 94-03, 1994

Mayer, S. Particle Motion in Unsteady Tree-Dimensional Flow at Low Reynolds Numbers, AFM 94-04, 1994

Hansen, M. O. L. Vorticity-Velocity Formulation of the Navier-Stokes Equation for Aerodynamic Flows, AFM 94-07, 1994

Hvid, S. L. Curvature Based Smoothing of Plane Cubic B-spline Curves, AFM 93-08, Surface Description Using Bicubic B-splines, AFM 93-10, QM3D, 3D Netgenerering, Brugermanual, AFM 94-02 and Three Dimensional Algabraic Grid Generation, AFM 94-08, 1993-94

Walther, J. H. Discrete Vortex Method for Two-dimensional Flow past Bodies of Arbitrary Shape Undergoing Prescribed Rotary and Translational Motion, AFM 94-11, 1994

Nim, E. Energidissipation og masseoverførsel af gas i og omkring statiske miksere med boblestrømning, Ph.d. under ATV, EF410, 1994

Filippone, A. Interaction of Potential Flow Model with the Navier-Stokes Equations for Rotor Aerodynamics, AFM 95-07, 1995

Jensen, E. Optimization of the Electromagnetic Flowmeter, AFM 95-09, 1995

Schmidt, J. J. Experimental and numerical investigation of separated flows, ET-PHD 97-01, 1997

Nygreen, P. A vorticity-streamfunction formulation of the Navier-Stokes equations for predicting unsteady flow past bodies in arbitrary movement, ET-PHD 97-02, 1997

Sørensen, D. N. Aerodynamic Modeling and Optimization of Axial Fans, ET-PHD 98-01, 1998

Lennart, A. S. Experimental and theoretical/numerical study of evaporation from shallow pools of organic liquids, at simulated work place conditions, ET-PHD 98-02, 1998

Johansen, J. Unsteady Airfoil Flows with Application to Aeroelastic Stability, Risø-R-1116(EN), 1999

Ullum, U. Imaging Techniques for Planar Velocity and Concentration Measurements, ET-PHD 99-03, 1999

ISBN 87-7475-232-4